



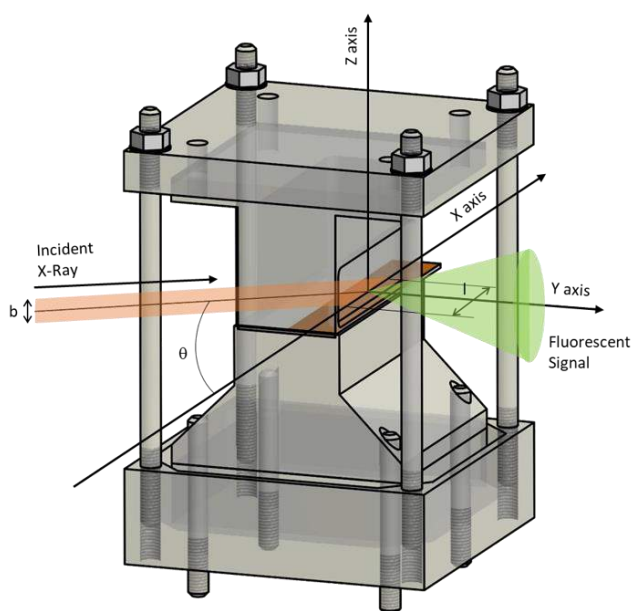
UNIVERSITÀ
DEGLI STUDI
FIRENZE

DOTTORATO DI RICERCA IN SCIENZE CHIMICHE

CICLO XXX

COORDINATORE Prof. Piero Baglioni

ELECTRODEPOSITION AND CHARACTERIZATION OF METALS FOR IMPROVED CORROSION RESISTANCE AND ENERGY CONVERSION



Dottorando

Dott. Enrico Berretti

Co-Tutore

PhD Alessandro Lavacchi

Tutore

Prof. Massimo Innocenti



UNIVERSITÀ
DEGLI STUDI
FIRENZE

DOTTORATO DI RICERCA IN SCIENZE CHIMICHE

CICLO XXX

COORDINATORE Prof. Piero Baglioni

ELECTRODEPOSITION AND CHARACTERIZATION OF METALS FOR
IMPROVED CORROSION RESISTANCE AND ENERGY CONVERSION

Settore Scientifico Disciplinare CHIM/01

Dottorando

Dott. Enrico Berretti

(firma)

Tutore

Prof. Massimo Innocenti

(firma)

Co-Tutore

PhD Alessandro Lavacchi

(firma)

Coordinatore

Prof. Piero Baglioni

(firma)

Anni 2014/2017

Index

| | | |
|----------|--|-----------|
| 1 | INTRODUCTION | 1 |
| 2 | METHODS | 4 |
| 2.1 | ELECTRODEPOSITION | 4 |
| 2.2 | SURFACE DEPENDENT DEPOSITION METHODS | 8 |
| 2.2.1 | <i>Under Potential Deposition (UPD) & Electrochemical Atomic Layer Deposition (E-ALD)</i> | <i>8</i> |
| 2.2.2 | <i>Redox Replacement (RR) & Surface Limited Redox Replacement (SLRR)</i> | <i>10</i> |
| 2.3 | SYNCHROTRON LIGHT METHODS | 13 |
| 2.3.1 | XAS | 14 |
| 2.3.1.1 | Transmission Mode | 14 |
| 2.3.1.2 | Fluorescence Mode | 15 |
| 2.3.1.3 | Energy and transition probability | 16 |
| 2.3.1.4 | XANES & EXAFS | 17 |
| 2.3.1.5 | The XAS Beamline | 18 |
| 2.3.2 | FEXRAV | 19 |
| 2.3.3 | GIXAS | 22 |
| 3 | ELECTRODEPOSITION AND CHARACTERISATION OF PALLADIUM FILMS AS CATALYST LAYERS IN DIRECT ETHANOL FUEL CELLS (DEFCS) | 24 |
| 3.1 | INTRODUCTION | 24 |
| 3.1.1 | <i>Fuel Cell Working Principle: The Hydrogen/Oxygen Cell</i> | <i>27</i> |
| 3.1.2 | <i>Fuel Cells Criticalities</i> | <i>28</i> |
| 3.1.2.1 | The Polymeric Electrolyte Membrane | 28 |
| 3.1.2.2 | Catalysts for Cathodic reactions | 29 |
| 3.1.2.3 | Catalyst for Anodic reactions | 30 |
| 3.1.3 | <i>Direct Alcohol Fuel Cells (DAFCs)</i> | <i>30</i> |
| 3.1.4 | <i>Alkaline Direct Ethanol Fuel Cells (ADEFCs) & Ethanol Electrooxidation reaction</i> | <i>31</i> |
| 3.1.5 | <i>Palladium electrochemical behaviour in alkaline media</i> | <i>33</i> |
| 3.2 | THE FEXRAV EXPERIMENT | 36 |
| 3.2.1 | <i>The FEXRAV Cell</i> | <i>37</i> |
| 3.2.2 | <i>Samples preparation & Chemicals</i> | <i>37</i> |
| 3.2.3 | <i>Experimental Set-Up</i> | <i>41</i> |
| 3.2.4 | <i>Beam Energy Selection & Detection Limit</i> | <i>41</i> |
| 3.2.5 | <i>Results</i> | <i>43</i> |

| | | |
|---------|---|----|
| 3.2.5.1 | Half-Cell Measures | 43 |
| 3.2.5.2 | Fuel Cell Measures | 48 |
| 3.2.6 | <i>Study on Pd deactivation using FEXRAV and Computational Speciation Models</i> | 49 |
| 3.3 | THE GI-FEXRAV EXPERIMENT | 49 |
| 3.3.1 | <i>Why combining GIXAS and FEXRAV?</i> | 49 |
| 3.3.2 | <i>GI-FEXRAV cell</i> | 51 |
| 3.3.2.1 | GI-FEXRAV Cell Preparation | 55 |
| 3.3.3 | <i>Catalytical Model Surfaces preparation</i> | 58 |
| 3.3.3.1 | Chemicals | 59 |
| 3.3.3.2 | Substrate Preparation | 60 |
| 3.3.3.3 | Substrate Analysis | 61 |
| 3.3.3.4 | UPD of Cu on Polycrystalline Au (111) | 65 |
| 3.3.3.5 | SLRR of Pd from Cu & Alcohol Oxidation Tests | 67 |
| 3.3.3.6 | Ethanol oxidation tests | 68 |
| 3.3.3.7 | Comparison between the electrochemical behaviour of UPD Pd and Pd NPs towards ethanol oxidation | 69 |
| 3.3.3.8 | XPS surface characterization | 71 |
| 3.3.3.9 | Final Considerations on prepared sample surfaces | 72 |
| 3.3.4 | <i>Data Acquired</i> | 74 |
| 3.3.4.1 | Ex Situ Experiment | 74 |
| 3.3.4.2 | In Situ Experiments | 75 |
| 3.3.5 | <i>Topography of the sample after the GI-FEXRAV experiment</i> | 78 |
| 4 | ELECTRODEPOSITION AND CHARACTERIZATION OF ALUMINIUM METAL FILMS FROM IONIC LIQUIDS (ILS) | 81 |
| 4.1 | INTRODUCTION | 81 |
| 4.2 | IONIC LIQUIDS | 81 |
| 4.3 | ALUMINIUM | 84 |
| 4.4 | ELECTRODEPOSITION OF ALUMINIUM FROM IONIC LIQUIDS | 85 |
| 4.5 | STUDY ON THE DEPOSITION CONDITIONS | 87 |
| 4.6 | ROTATING HULL CYLINDER (RHC) | 89 |
| 4.6.1 | <i>Design of the Cell</i> | 90 |
| 4.6.2 | <i>Testing of the cell & FEA model</i> | 93 |
| 4.7 | ELECTRODEPOSITED ALUMINIUM AS THERMAL BARRIER IN TURBINE VANES | 97 |

| | | |
|----------|---|------------|
| 5 | CONCLUSIONS | 99 |
| 5.1 | FEXRAV EXPERIMENTS AND Pd DEACTIVATION..... | 99 |
| 5.2 | ALUMINIZATION FROM IONIC LIQUIDS..... | 101 |
| 6 | APPENDIX | 102 |
| 6.1 | APPENDIX A: ARTICLE “COMPUTATIONAL SPECIATION MODELS: A TOOL FOR THE INTERPRETATION OF SPECTROELECTROCHEMISTRY FOR CATALYTIC LAYERS UNDER OPERATIVE CONDITIONS | 102 |
| 6.2 | APPENDIX B: FEXRAV/GIXAS CELL SCHEMATICS | 109 |
| 6.3 | APPENDIX C: ARTICLE “ALUMINIUM ELECTRODEPOSITION FROM IONIC LIQUID: EFFECT OF DEPOSITION TEMPERATURE AND SONICATION” | 118 |
| 6.4 | APPENDIX D: RHC SCHEMATICS..... | 133 |
| 6.5 | APPENDIX E: ARTICLE “ALUMINIZING VIA IONIC LIQUID ELECTRODEPOSITION AND PACK CEMENTATION: A COMPARATIVE STUDY WITH INCONEL 738 AND A CoNiCrAlY” | 144 |
| 7 | BIBLIOGRAPHY..... | 156 |

Acronyms

| | |
|-------------------------|---|
| <i>CE</i> | Counter Electrode |
| <i>DES</i> | Deep Eutectic Solvent |
| <i>E-ALD</i> | Electrochemical Atomic Layer Deposition |
| <i>EOR</i> | Ethanol Oxidation Reaction |
| <i>FEXRAV</i> | Fixed Energy X-Ray Absorption Voltammetry |
| <i>GI-FEXRAV</i> | Grazing Incidence FEXRAV |
| <i>GIXAS</i> | Grazing Incidence X-ray Absorption Spectroscopy |
| <i>HC</i> | Hull Cell |
| <i>HOR</i> | Hydrogen Oxidation Reaction |
| <i>IL</i> | Ionic Liquid |
| <i>NP</i> | NanoParticle |
| <i>ORR</i> | Oxygen Reduction Reaction |
| <i>RE</i> | Reference Electrode |
| <i>RHC</i> | Rotating Hull Cell |
| <i>UPD</i> | Under Potential Deposition |
| <i>WE</i> | Working Electrode |
| <i>XAS</i> | X-ray Absorption Spectroscopy |

1 Introduction

Electrodeposition, or electroplating, was one of the first technologies developed, in the late 18th century, from the studies about the electricity issues. His history began with Luigi Brugnatelli, a colleague of Alessandro Volta who, in 1805, firstly performed the coating by thin layers of gold on conductive manufacts, exploiting Volta's device as a source of electrical power. After this discovery, throughout the years of the nineteen century, technology developed many new ways to utilise this technique, obtaining metallic coatings of various elements on conductive and nonconductive substrates, first for aesthetic purposes and finally for a technological application. The first electroplating techniques were used to mass reproduce metallic artistic manufacts with complex shapes, and to cover them with thin layers of noble metals, to give the illusion of bulk precious artifacts¹. The versatility of the method led shortly to its usage in a strictly industrial context, to the deposition of thick layers of less noble metals, to hinder corrosion phenomenon or to enhance particular surface properties of the processed items. Finally, not only to improve the aesthetic features of the treated object but to boost its chemical and physical characteristics. Until today, research on this topic has developed a broad range of electrolytic solutions (also called galvanic baths) to obtain coatings of different elements, compounds, and alloys, but some issues related to the deposition of certain metals, and the electrochemical stability and safety of the relative plating baths are still unresolved.

The work done during my PhD has focused on two main topics, related to electrodeposition processes and the characterisation of the obtained coatings:

- a) Electrodeposition and characterisation of palladium films as catalyst (Anodic) layers in Direct Ethanol Fuel Cells (DEFCs).
- b) Electrodeposition and characterisation of aluminium metal films from Ionic Liquids (ILs);

Both the addressed topics have a high industrial relevance in the field of energy production, but they have needed two slightly different approaches to the study of the involved phenomenon.

My work on the electrodeposition from ionic liquids was, in fact, part of a European project (SCAIL-UP, [HTTP://scailup.eu](http://scailup.eu)) for the scaling up of the aluminising operation from ionic liquids, from a lab scale set-up to an industrial process. The final objective of this project was, in fact, the production of a pilot plant for the aluminization process via ionic liquids of turbine vanes for energy and aerospace applications. My work on this topic mainly focused on technological and industrial aspects of electrodeposition, in the research of the optimal deposition conditions to obtain metallic layers with specific properties (thicknesses, corrosion resistance and morphology).

On the other hand, the study and characterisation of Pd surfaces for alcohol reactions in alkaline Direct Ethanol Fuel Cells (DEFCs) had a more fundamental science footprint. This research focused mainly on the improvement of an analytical technique used in high fluence X-Ray sources (Synchrotrons), and on the development of electrodeposition methodologies for the preparation of ordered metallic layers usable as model catalytical coatings for the study of alcohol electrooxidation. Particular focus was paid on palladium, a promising metal for the anodic reactions in Alkaline Direct Alcohol Fuel Cells (DAFCs). Two main electrodeposition techniques were used to control the amount of deposited palladium: the Electro-Chemical Atomic Layer Deposition (E-ALD) and the Surface Limited Redox Replacement (SLRR). Part of this work was carried out during two experiments at the European Synchrotron Radiation Facility

(ESRF) in Grenoble during the last year, performed by X-Ray Absorption Spectroscopy (XAS).

In the end, both the addressed research topics exploited state of the art deposition and characterization techniques to study the obtained metal coatings. The ability to precisely control deposit coverage and thicknesses via E-ALD and SLRR, the possibility to electrodeposit metals from “exotic” electrolytes like ionic liquids and the use of in situ synchrotron techniques to characterize the obtained metallic films could permit, in future, to design and prepare new materials and devices of great industrial interest, to overcome today’s manufacturing limitations..

A scheme of the work presented in this thesis can be found in **Figure 1**.

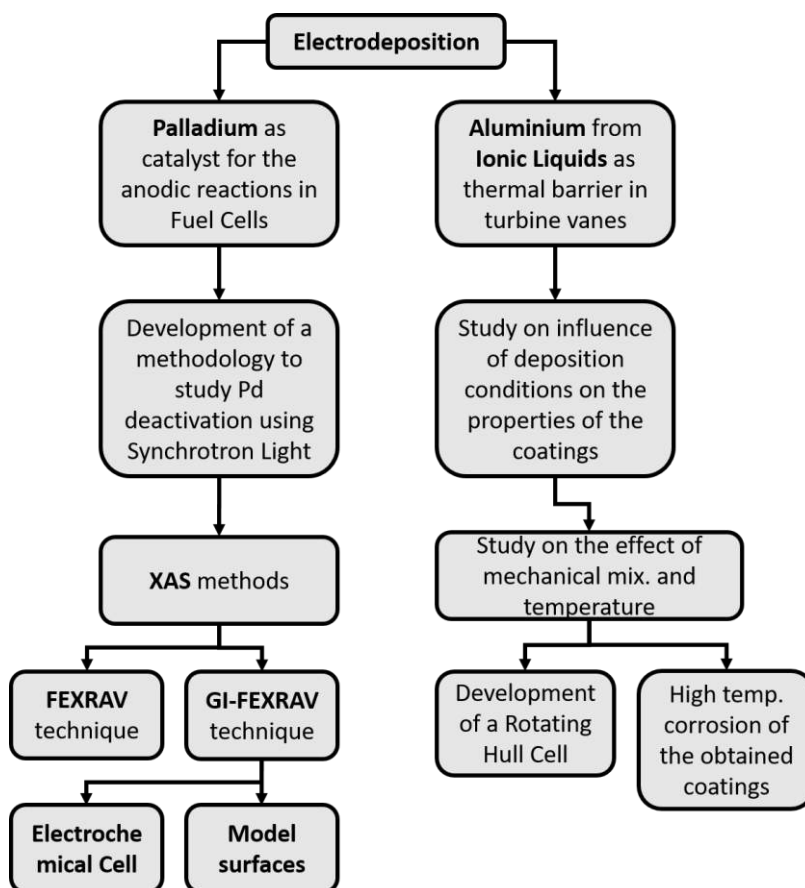


Figure 1 – The scheme of the work presented in this thesis

2 Methods

2.1 Electrodeposition

The electrodeposition, or electroplating, is a technique that permits, through the application of a particular potential between two electrodes, the discharge of ionic species from a solution (called electrolyte) to a conductive object, called electrode (particularly a cathode for the discharge of cationic species like metals). This process is led by a charge transfer at the electrolyte/electrode liquid/solid interface and leads to the formation of a solid film above the surface of the cathode, whose thickness is dependent on the used deposition parameters (deposition time, current and potential applied, nature and kinetics of the phenomenon involved).

The apparatus adopted to perform the electroplating process is called electrochemical cell, and is mainly composed of two solid conductive elements, called electrodes:

- An anode, on which the oxidation reaction takes place;
- A cathode, on which the reduction reaction occurs.

The two electrodes are immersed in salty conducting solutions, called electrolyte; the union between an electrode and its electrolyte is called “half-cell”. Electrochemical cells used for the electrodeposition process slightly differ from the ones usually schematized for the galvanic process (i.e. batteries)² (**Figure 2**).

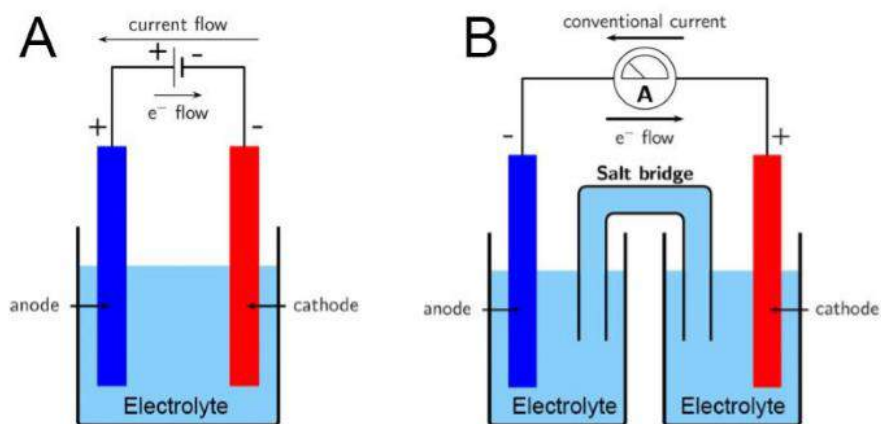


Figure 2 – two different kinds of Electrochemical cells: (A) An Electrolytic Cell and (B) A Galvanic Cell

In galvanic cells, the salt bridge is essential to separate the anodic solution from the cathodic one, to permit the establishment of the equilibria needed to let the cell work correctly, following spontaneous pathways³. On the other hand, ordinary electrolytic cells for metal deposition are constituted by a single vessel, or tank, in which the solution hosts both the electrodes. This fact leads to a first consideration; during spontaneous processes involved in galvanic cells, particular attention has to be paid both to the cathodic and the anodic reactions respectively. Instead, during metal electrodeposition, the focus is shifted primarily on the cathode, and on reactions occurring on its surface. In these cells, the anode is often constituted by the metal we want to deposit; its dissolution during the oxidation process permits to replenish the electrolyte with cations, and consequently to maintain a certain concentration of the electrodeposited ionic species into the galvanic bath.

For these reasons, the cathode, on which the deposition phenomenon occurs, is named working electrode (WE), while the anode is named counter electrode (CE). A third electrode on which no current flow, the reference electrode (RE), could be present (**Figure 3**).

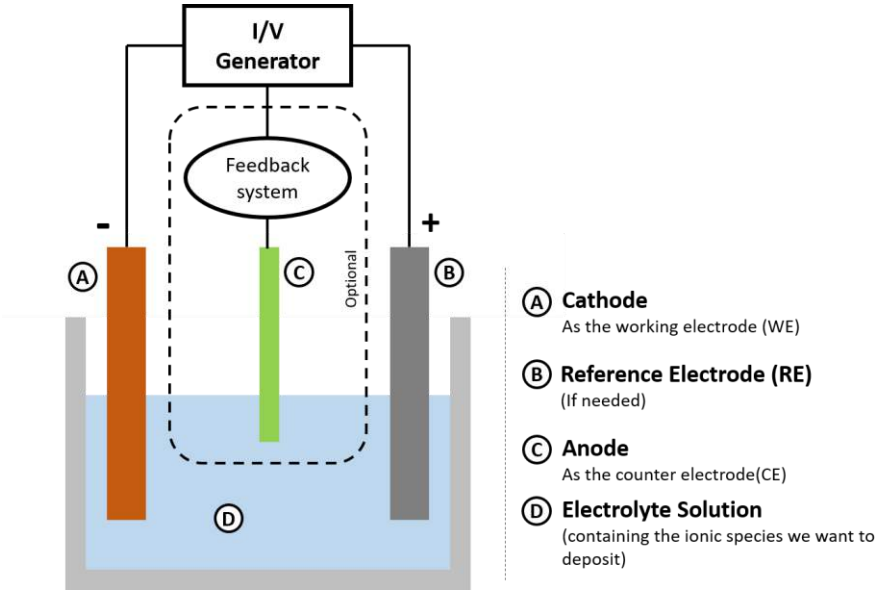


Figure 3 – A scheme of an electrolytic cell for the electrodeposition of metals: a two or three electrodes set up can be used.

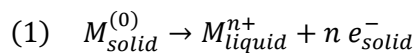
In fact, a two or three electrode set-up can be used depending on the electrochemical process we want to perform:

- During **Potentiostatic deposition** a three-electrode set-up must be used.
- During **Galvanostatic deposition** a two electrodes set-up could be used.

A brief description of these two techniques is presented below:

Potentiostatic deposition implies the application of a constant potential to the working electrode, to perform electrodeposition.

In general, when a metal is immersed in a solution, it tends to dissolve to reach chemical equilibrium, releasing, into the electrolyte, their relative ions, following the generic formula **(1)**:



Where solid and liquid indicate the phase in which the object is present. This dissolution process leads to the formation of electrode related ions on the solution side, and to the electron stacking on the solid side surface. At the

same time, ions from the solution become deposited out on the electrodes. The potential differences at the metal-solution interface are controlled by the rate of these two opposing processes. The specific potentials at which these two reaction rates are equal (called standard potentials) are usually given in the literature for solutions at 25°C and activity at value unity. The equilibrium potential at a metallic electrode, which is at equilibrium with its ions, is given by the Nernst expression **(2)**:

$$(2) \quad E^r = E^0 + \frac{RT}{zF} \ln a_{ion}$$

Where:

- E^r is the reversible electrode potential (in Volt);
- E^0 is the standard oxidation potential for the metal (in Volt), related to solutions at 25°C, and activity at value unity;
- R is the universal gas constant ($R = 8.314472 \text{ J K}^{-1} \text{ mol}^{-1}$);
- z is the number of electrons transferred in the oxidation reaction;
- F is the faraday constant ($F = 9.64853399 \times 10^{-4} \text{ C mol}^{-1}$);
- A_{ion} Indicates the ionic actual activity of the metal cations dissolved in the solution.

Formula **(2)** is related to the reversible/equilibrium potential, but deposition occurs as an irreversible process. To perform the deposition of metal, the electrode potential has to be shifted to more negative values (E^d), in respect to the previous reversible potential, by the overvoltage η . the Nernst expression can then be modified to obtain the deposition potential as in equation **(3)**:

$$(3) \quad E^d = E^0 + \frac{RT}{zF} \ln a_{ion} + \eta$$

And finally $\eta = E^d - E^r$, with $\eta < 0$. η can then be considered the potential shift from the equilibrium potential needed to maintain the deposition going at a given desired rate⁴. Potentiostatic deposition is then a deposition process in which the working electrode is maintained to a constant potential E^d thanks to the feedback with the reference electrode, while the deposition current is let flow between WE and CE.

During **Galvanostatic deposition**, a current flow is imposed inside the cell between the cathode and the anode. In this case, the flow direction defines on which electrode the reduction reaction will occur. The electrode connected to the minus terminal of the current generator will be covered with electrons, favouring the discharge of cationic species on its surface and thus the reduction process; vice versa on the other electrode anodic reactions will occur.

Common industrial electroplating processes (like Ni, Cr, Cu, Ag, Au plating) are commonly performed using current controlled methods (like the galvanostatic method). On the other hand, potential controlled methods are more suitable for some niche processes in which a better compositional control is needed (deposition of alloys), and in the characterisation of electrolytic bath behaviour⁵.

2.2 Surface Dependent Deposition Methods

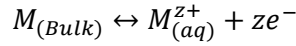
Apart from the conventional electrodeposition methods, two particular techniques were used during this research, the Electrochemical Atomic Layer Deposition (E-ALD) and the Surface Limited Redox Replacement (SLRR). Both these techniques exploit surface limited phenomenon, thus permitting an ordered mono or submonolayer atomic deposition and, in the end, the minimization of the amount of deposited metal. The particular interest in these techniques resides also in the possibility to stack different monolayers to grow a compound^{6,7}, a semiconductor as an example, or even to stack two different semiconductors to grow a P-N junction⁸. During both the XAS experiments, E-ALD method was used in conjunction with SLRR (obtaining first a sacrificial metal deposit, and then substituting the sacrificial metal with the palladium) and alone (to get a direct surface limited deposition of palladium above the gold substrate).

2.2.1 Under Potential Deposition (UPD) & Electrochemical Atomic Layer Deposition (E-ALD)

Usually, to potentiostatically obtain the electrodeposition of bulk metal, we have to apply at the working electrode a potential that is more negative respect to the Nernst equilibrium potential. As already mentioned, in the electrocrystallization field, this potential is commonly defined as overpotential η :

$$\eta = E - E_{M_{(Bulk)}/M_{(aq)}^{z+}}$$

Where E is the actual electrode potential, and $E_{M_{(Bulk)}/M_{(aq)}^{z+}}$ is the Nernst equilibrium potential of the reaction:



Where $M_{(Bulk)}$ represent the bulk metallic material, and $M_{(aq)}^{z+}$ stands for a ion in solution, bearing the charge number z . For bulk materials, due to kinetic hindrances, metal deposits take place when $E < E_{M_{(Bulk)}/M_{(aq)}^{z+}}$, so that the overvoltage results with the condition $\eta < 0$. During Under Potential Deposition (UPD), reverse conditions occur, because metal deposition occurs when $E > E_{M_{(Bulk)}/M_{(aq)}^{z+}}$, so that $\eta > 0$. This means that to achieve UPD of a metal we have to apply a potential that is more positive respect the Nernst potential⁹. Thanks to this, we can define UPD phenomenon as “the deposition of a metal at more positive potentials in respect to the deposition potential of the metal onto itself”; this leads to different considerations:

1. To achieve the UPD phenomenon the chemical nature of the species we want to deposit and the ones constituting the substrate must differ;
2. UPD is a surface limited phenomenon. Interactions between a foreign substrate and ions could occur only until the base surface is not completely covered; this means that using Under Potential Deposition, can be attained only a maximum of an atomic monolayer of deposit above the substrate.

Even if the precise mechanics that lead to the Under Potential Deposition cannot be univocally addressed, we can locate the driving force of the process into constructive interactions between ions and the surface. Chemical interactions, as adsorption of the ionic species above the substrate, could favour the discharge of ionic species, leading to the need for less energy (and thus less negative potentials) to achieve deposition (**Figure 4**^{6,7,10}).

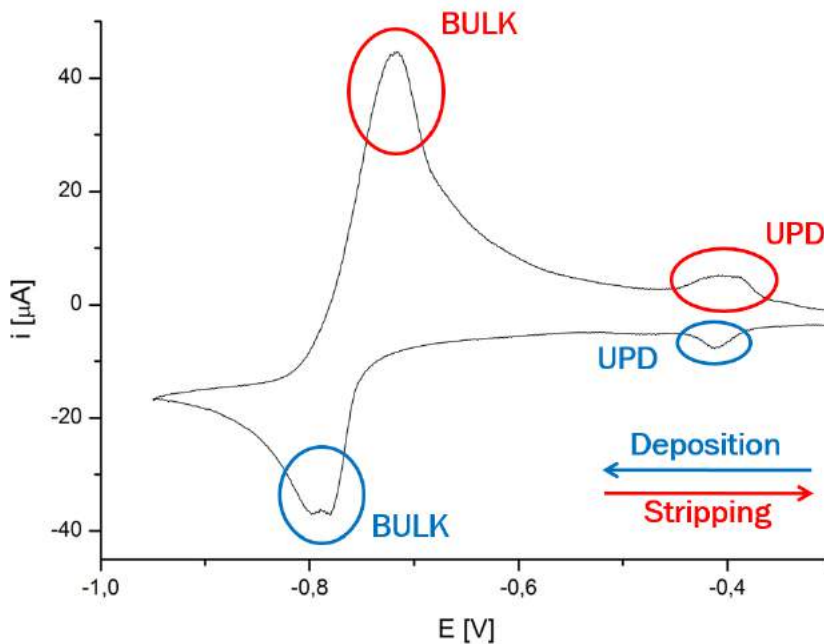


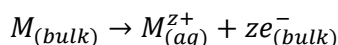
Figure 4 – A cyclic voltammetry of a Cd^{2+} solution in ammonia buffer (pH 9.2) performed on an Ag(111)/S electrode, scan speed 20mV/sec, potentials referred to the Ag/AgCl KCl sat. electrode. During the forward (cathodic) scan, a peak related to the monolayer UPD of Cd is visible at potentials of about -0.4V, far before the bulk deposition, that occurs at potentials lower than -0.8V. During the anodic scan, the process is reversed

The exploitation of the UPD phenomenon is the foundation of the Electrochemical Atomic Layer Deposition (E-ALD) technique, which permits the growth of Nanofilms stacking layers of UPD films one above the other^{8,11}.

2.2.2 Redox Replacement (RR) & Surface Limited Redox Replacement (SLRR)

Redox Replacement (RR) is an electrochemical phenomenon in which we have the dissolution of a species from a solid electrode and the contemporaneous deposition of another species on the same electrode from an ionic bath. The working mechanics of the process is similar to the ones seen during galvanic cell operations, but for RR a single piece of conductive material acts both as cathode and anode. In fact, Redox replacement can be seen as a particular kind of wet corrosion, that occurs when a conductive object (made by a metal called A) is placed in an

electrolytic bath with ions of a more noble metal (called B, with a higher reduction potential). When this happens, an equilibrium between the solid and the liquid phase tends to form, leading (especially for less noble metals, like Zn, Cu) to the dissolution of the electrodic metal A and the formation of the relative cations on the electrolyte side, following the general oxidation reaction:



The electrons released during this reaction remain on the solid conductive phase and are free to move inside metal A, until they find a surface spot with an adsorbed ion of metal B. At this point a reduction of the adsorbed metal ion can occur, with the formation of a metallic atom B on the surface of metal A. In **Figure 5** a brief scheme of the process is shown.

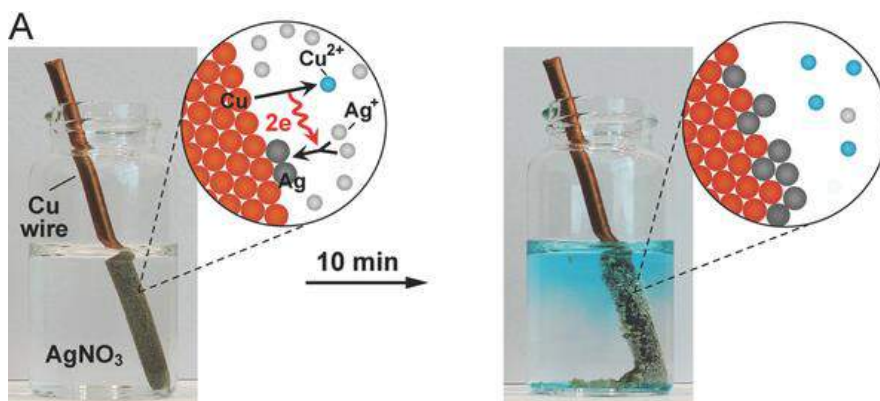


Figure 5 – An example of redox replacement (RR); the electron exchange between the dissolving copper and the adsorbed silver leads to the production of an Ag film on the object surface

The overall process can be then divided into two reactions occurring simultaneously:

- The coating of a thin film of the noblest metal on certain surface spots of the object;
- The dissolution of the less noble metal in another zona.

The process can usually be prolonged till the obtainment of micrometric thicknesses of the noblest metal, as well known even by the Mesoamerican cultures before the contact with Europeans^{12–14} (**Figure 6**).



Figure 6 – A pre-Columbian gilded mask from Loma Negra archaeological site; the gold layer was obtained using RR

A further enhancement of this method exploits, as a base substrate, an electrode made of a thin layer of a less noble metal deposited on a noble surface. When this solid is poured into a solution containing ions of a metal whose redox potential is in between the two of the solid phase, galvanic exchange can occur. This phenomenon is called Surface Limited Redox Replacement (SLRR), just because after the galvanic exchange between the surface metal and the one present in solution, the process stops, hindered by the bottommost noble surface. This technique is commonly used^{15–17} on mono or submonolayers of metals deposited via Under-Potential Deposition (UPD) to obtain the substitution of the topmost deposits solely.

2.3 Synchrotron Light Methods

A synchrotron is a cyclic particle accelerator in which electrons are moved in order to produce high-intensity X-rays, thanks to the bremsstrahlung phenomenon. To better understand their working principle, a schematic description of the European Synchrotron Radiation Facility (ESRF) is shown in **Figure 7** as an example:

1. Electrons are first accelerated, packed in “bunch”, to 200 million electron-volts thanks to an electron gun, called LINAC, in order to finish into the booster ring.
2. The booster ring, with a length of about 300 m, is needed to provide an additional acceleration of the electrons, till they reach an energy of 6 GeV; the charged particles are forced to follow the particular shape of the ring thanks to magnets scattered in the ring curves.
3. Once reached the working energy, the electrons are injected into the storage ring, an 844 meters high vacuum tubing with a series of beamlines disposed tangentially to its circumference. Again, the maintaining of the circular electron trajectory is due to different types of magnets, placed at the frontend of a beamline. These devices are in fact responsible for the X-ray emission; the trajectory change induced in the electron by the magnet permits the emission of the bremsstrahlung X-Ray radiation used on the beamlines.

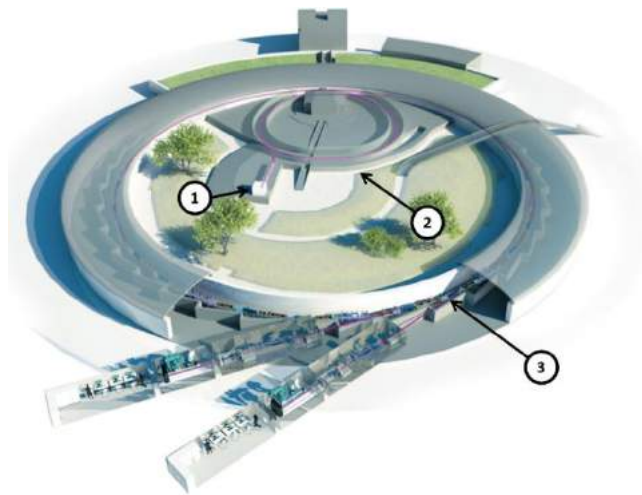


Figure 7 – The main parts of a synchrotron: 1) The LINAC, 2) The Booster Ring, 3) The Storage Ring & the Beamlines

Synchrotron facilities are essential due to their high X-Ray brilliance. This feature permits a vast array of both in-situ and ex-situ characterization techniques, exploiting their high-intensity x-ray source. Such techniques vary from diffraction to absorption, imaging and so on, and can be used in a wide range of different research fields. The experiments cited in this thesis were performed in an X-Ray Absorption Spectroscopy (XAS) dedicated line at the European Synchrotron Radiation Facility (ESRF) in Grenoble.

2.3.1 XAS

X-ray Absorption Spectroscopy (XAS) is a broadly used method to investigate local atomic structure as well as electronic states. At its core, it is based on the study of the variation of the absorption coefficient μ of samples subjected to irradiation by a coherent x-ray flux. During an XAS experiment, the sample is hit by an incident X-Ray beam with intensity I_0 ; a portion of the radiation will be absorbed by the sample and re-emitted on the whole solid angle with intensity I_f , while part will pass through the specimen with a dampened intensity I_t . Conceptually, an XAS experiment can then be associated to a UV-VIS spectroscopy, despite the differences between the involved absorption mechanisms; data acquisition can then be performed both in transmission mode and in fluorescence mode (**Figure 8**).

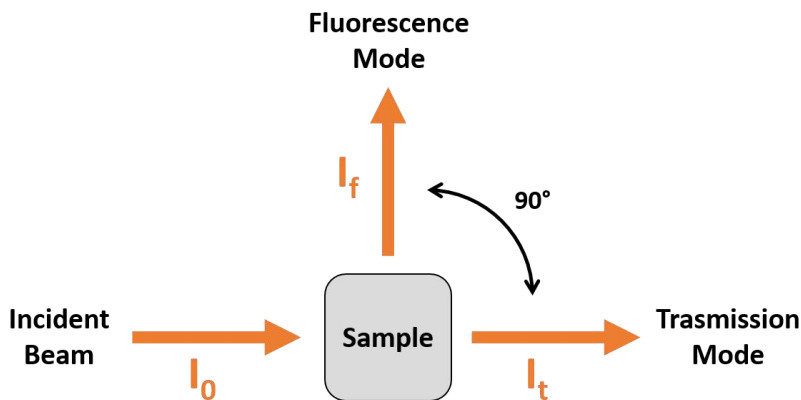


Figure 8 – The two experimental set-ups that can be used during XAS

2.3.1.1 Transmission Mode

The transmitted signal I_t has an intensity which is related to the absorption coefficient, and to the thickness of the sample through a law conceptually similar to Lambert-Beer one (4).

$$(4) \quad I_t(l) = I_0 \cdot e^{-\mu(E)l}$$

Where l is the sample thickness, and $\mu(E)$ is the radiation energy-related absorption coefficient. Rearranging the previous formula, we can write the absorption coefficient for a transmission mode XAS experiment as (5):

$$(5) \quad \mu(E) \propto \frac{I_0}{I_t}$$

2.3.1.2 Fluorescence Mode

The radiation absorption, and thus the fluorescence emission, are linked to the photoelectric effect. An X-ray beam strikes a sample and excites core electrons that can either be promoted to an unoccupied level or ejected from the atom. If the negative charge dissociates, this produces an excited ion with an electron vacancy in an inner shell. During the relaxation process (**Figure 9**) the vacancy can be filled by an outer shell electron, and the emitted energy can be dissipated by in the emission a photon (fluorescence) or of another electron (Auger effect) on all the solid angle around the sample.

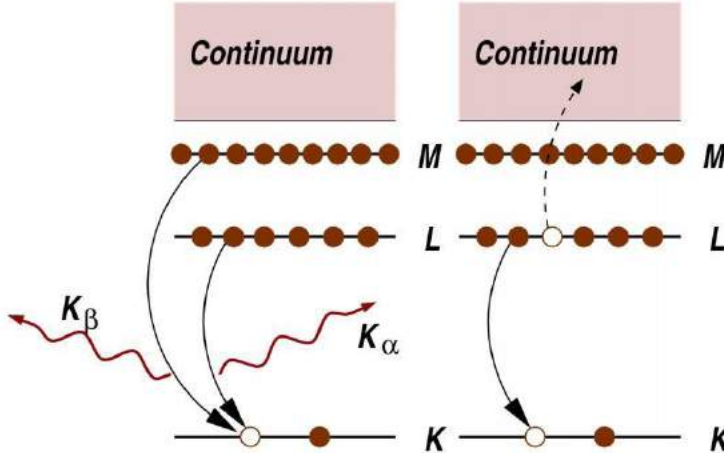


Figure 9 – The relaxation process could lead to the emission of a photon (left) or by the emission of another electron (Auger effect, right)

Both the emitted particles could be used to determine the absorption coefficient, but in the fluorescence emission is more intense for high energy X-rays (Hard X-Ray region). Exiting photon intensity I_f can be collected and related to the absorption coefficient by formula (6):

$$(6) \quad \mu(E) \propto \frac{I_f}{I_0}$$

2.3.1.3 *Energy and transition probability*

The atom absorption process occurs if the incident x-ray has a precise energy (related to the transition we want to provoke) and it is in fact associated with a specific interaction probability through the Fermi Golden Rule (7).

$$(7) \quad \mu(E) \propto |M|^2 \rho \propto |\langle f | H_p | i \rangle|^2 \rho$$

The bracketed term expresses the probability of a transition between initial state i and final state f , and it is proportional to the product of the square abs of the matrix M with the density of states ρ . H_p represents the Hamiltonian perturbation of the states due to the electromagnetic field of the X-Rays.

The electrons that are excited are typically from the 1s or 2p shell, so the energies are on the order of thousands of electron volts. XAS, therefore, requires high-energy X-ray excitation, which occurs at synchrotron facilities. X-ray energy is about 10^4 eV (where "soft x-rays" are between 100 eV- 3 keV and "hard x-rays" are above three keV) corresponding to wavelengths around 1 Angstrom. This wavelength is on the same order of magnitude as atom-atom separation in molecular structures, for this reason, XAS is a useful tool to deduce the local structure of atoms. XAS is also utilised in analysing materials based on their characteristic X-ray absorption "fingerprints." It is possible to deduce local atomic environments of each separate type of atom in a compound. This feature is caused by the diffusion/retro diffusion of the emitted photoelectrons that will behave like waves, interacting with the other vicinal atoms giving interference. We can see a similar phenomenon when a rock is thrown into a pond; waves created by the object hitting the surface will propagate radially, till their encounter with an object above the surface. The tide is then retro diffused, and during its trip back could interfere with the fringes of the arriving wave. This phenomenon leads to a modulation of the μ value, and thus to changes in the XAS spectra, dependent on the chemical environment in which the analyzed species are present. XAS is also particularly convenient because it is a non-destructive method that permits the determination of structures from heterogeneous and/or amorphous samples.

2.3.1.4 XANES & EXAFS

X-ray Absorption near Edge Spectroscopy (XANES) and Extended X-ray Absorption Fine Structure (EXAFS) refer to two different branches of the absorption spectra acquired during an XAS scan (**Figure 10**). It is, in fact, possible, during XAS measurements, to acquire the absorption coefficient μ varying the incident beam energy between the absorption edge of the element we want to characterise. The obtained spectra can then be divided into the two abovementioned regions:

- XANES region energy range extends from before the absorption edge, to 60-100 eV after;
- EXAFS region spans from 100 eV after the edge, to the end of the spectra (higher energies).

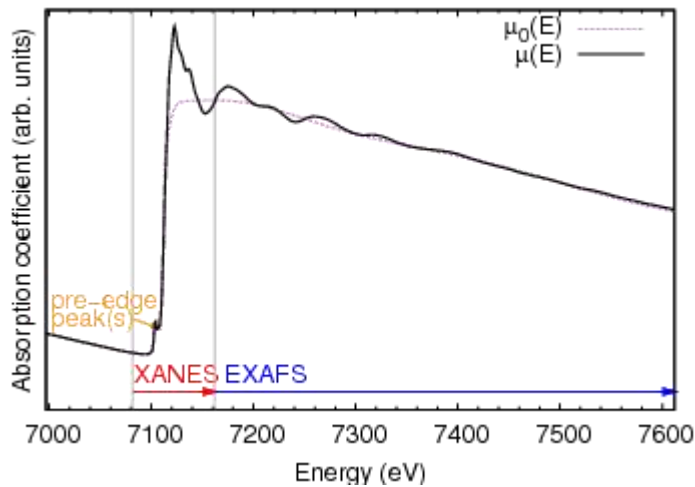


Figure 10 – The different zones of a XAS spectra

Different information could be acquired analysing XANEX and EXAFS intervals. Also, the degree of required data analysis is different (**Figure 11**).

| | XANES | EXAFS |
|----------------------|--|--|
| Data obtained | Geometry, Oxidation number | Coordination number, distances, Disorder |
| Modelization | Complex, feasible for simple systems | Easier to perform |
| Analysis | Easy if qualitative, Complex if quantitative | Moderately complex |

Figure 11 – Main differences between XANES and EXAFS spectra

XANES near edge fingerprint could be particularly helpful to identify individual states of the studied atomic species by comparison with spectra acquired from standards.

Acquiring a XAS spectra while varying energies could be a long process; depending on the experimental set-ups (Sample thickness, beam energy sample absorption, the distance between sample and detector...), measures could last several hours, depending on the signal to noise ratio for each energy scanned. During the performed experiments the XAS technique was employed to acquire data on Pd standards; mainly the XANES spectra were useful to permit a comparison between the various Pd species present in the reactive environment.

2.3.1.5 *The XAS Beamline*

The XAS experiments treated in this thesis were performed at the BM-08 line of ESRF in Grenoble. The design of this beamline permits surface and thin layer x-ray absorption experiments, but its flexibility allows also a wide range of different experimental set-ups. BM-08 exploits a bending magnet source and has an optical hutch capable of delivering x-rays in an energy range between 4 to 72 keV, with a maximum flux on the sample of $2 \cdot 10^{11}$ Ph/s at 20 KeV. The sample chamber permits to work in a vacuum, or in presence of different gaseous pressures, even at higher temperatures. Samples could be mounted on a grazing incident motorised support, which allows a sample/beam incident angle of the order of mrad, or on a holder head which permits ample 3d movement of the samples.

The experimental hutch is also equipped with two ionisation chambers, before and after the sample chamber; they are used to normalise the fluctuations of the x-ray beam that can occur during prolonged experiments.

The beam spot size could be regulated horizontally, from 0.2 mm to 10 mm, and vertically, from 0.2 mm to 2 mm, depending on the beam energy.

2.3.2 FEXRAV

Fixed Energy X-Ray Absorption Voltammetry (FEXRAV) is an in-situ synchrotron light methodology in which the conjunct use of XAS and voltammetric techniques permit a fast mapping of an element redox behaviour inside a defined potential window. This method is suitable to study red/ox kinetics of an element in well-defined and known systems, or to define a correlation between potential and red/ox behaviour of elements in complex and unknown matrices; the fixed energy value is opportunely chosen in a way that a signal variation can be interpreted as a variation of the chemical state of the element under study. Here the critical point is the selection of the right energy. This is done via the acquisition of XAS spectra on standards of the elements that are in different chemical states, representative of the species that form under operation. From the comparison of the spectra in the XANES region, the energy of the spectral feature that shows the most significant variation among the reference spectra is selected. Then, the variation of the fixed energy signal as a result of the change of the potential is recorded. Minguzzi & al. have applied this approach to the study of the oxidation states of Iridium during cyclic voltammetry¹⁸. They were able to determine the exact dependence of the Iridium oxidation state on the potential. The technique was termed Fixed Energy X-Ray Absorption Voltammetry (FEXRAV), and the same approach has been successfully applied to the investigation of the electrocatalytic activity of silver toward hydrodehalogenation reactions¹⁹. To use the FEXRAV technique, a particular design of the electrochemical cell has to be adopted (see chapters **3.2.1** and **3.3.2**). Usually, the sample acts both as working electrode, and as x-ray target for the XAS. It could be composed of certain thicknesses of nanostructured material, to maximise surface to volume ratio (and consequently to increase the signal related to surface reactivity). For this reason, FEXRAV could be particularly suitable to study dispersed systems, like nanoparticles.

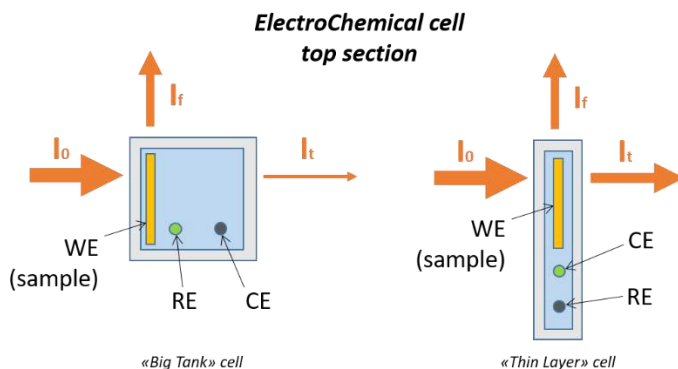


Figure 12 – Comparison between an EC cell usable in fluorescence mode (left) and an EC cell usable in transmission mode (right)

Like traditional XAS experiments, FEXRAV technique could be performed in transmission mode or fluorescence mode, depending on the electrochemical cell geometry and the displacement of the target electrode. During the electrochemical tests, the electrode surface has to be immersed in a liquid. This could lead to a dampening of the transmitted signal due to the scattering of the liquid, and consequently to a decrease in intensity of the I_t of the exiting beam, leading to longer acquisition times (to an increase of the signal to noise ratio). In principle, only thin layer cells should be used to acquire the absorption coefficient using the transmission mode, in order to minimize the liquid that the beam has to overpass, thus minimizing the scattering (its effect due to plastic cell walls depends on the used materials, but is often omissible in respect of the one generated by the liquid). Fluorescence mode is more accessible; even if a significant liquid volume is present beyond the sample electrode, the fluorescence intensity I_f could be acquired with a smart thin cell wall design (**Figure 12**).

The data obtained from a single FEXRAV experiment usually consist in:

- A Time vs Absorption coefficient μ data set;
- A Time vs Current (or potential) data set.

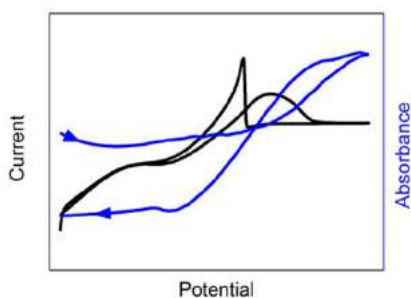


Figure 13 – An example of data acquired during a FEXRAV experiment: coupled with the voltammetric scan (black), the XAS signal (blue) can be seen. The experiment was led using undissaturated KOH 2M + EtOH 2M electrolyte, O₂ presence is responsible for the negative current at lower potentials. The use of undissaturated solutions was a particular choice, performed to reproduce normal working conditions of a fuel cell

The coupling between current and absorption spectra with the dependence of the potential variations in cyclic voltammetries is usually plotted, as in **Figure 13**. FEXRAV also shows the possibility to follow a system evolution during voltammetries by the prolonged acquisition of the emitted signal during subsequent voltammetric cycles. This could help to define and quantify variations in the inquired atom valence during prolonged voltammetric cycling, by plotting fluorescence signal and potential (or current) vs the experiment time, like in **Figure 14**.

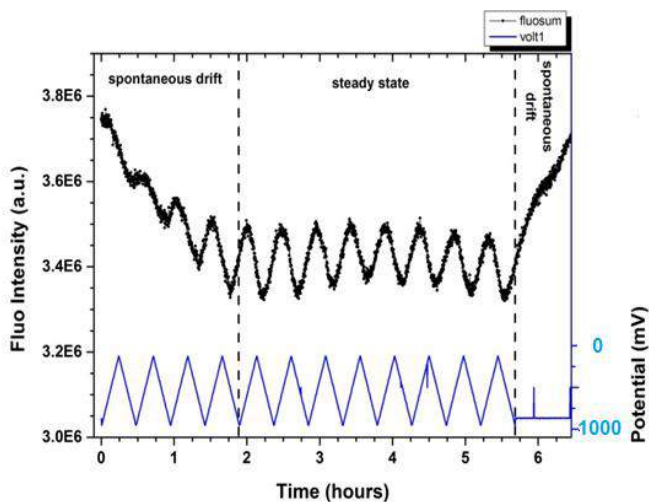


Figure 14 – The evolution of an atomic species can be followed by the study of the variations of the emission signal; kinetic information on the reactivity could also be acquired by coupling the XAS data with the change of potential/current during CVs

2.3.3 GIXAS

Grazing Incidence X-Ray Absorption Spectroscopy (GIXAS) is a technique in which the X-Ray beam hits the sample surface at a very low incident angle (below 0.5°)²⁰. This technique is well suited to investigate surfaces, like 2D films or especially large but thin layers because the grazing incidence set-up enables the sampling of only the topmost layers. The geometrical set-up permits also to project the x-ray beam over a large area of the specimen, inducing absorption of a larger amount of material by increasing the sample/beam interaction volume (**Figure 15**), and thus permitting an increase in the output signal, increasing the signal to noise ratio, and in the end decreasing the acquisition time of the absorption spectroscopy measurements.

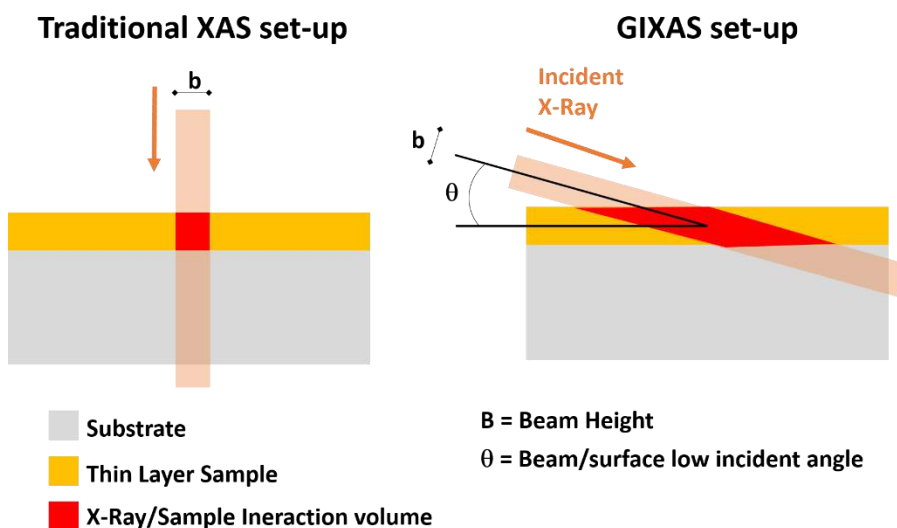


Figure 15 – Side view of the used experimental geometry on a thin layer sample for a traditional XAS measurement (left) and for the GIXAS method (right)

The dimension of the irradiated area is dependent on geometrical characteristics of the incident beam in respect to the sample surface. As an example, the sample irradiated length could be varied changing the x-ray beam height, and its incidence angle on the surface (which should be below 0.5°) following a simple trigonometrical formula ($b/l = \sin \theta$, where b is the height of the beam, l is its in-plane projection and θ is the angle between the incident x-rays and the sample surface, **Figure 16**).

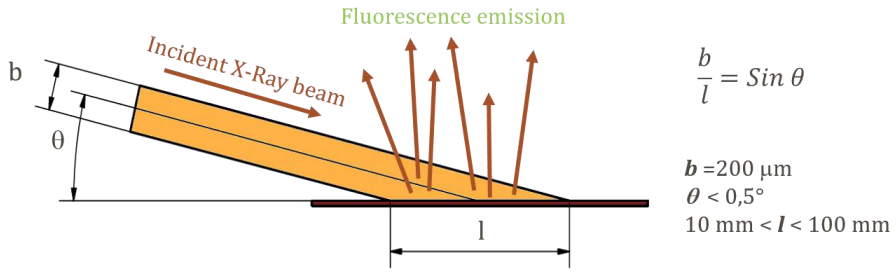


Figure 16 – Side view of a GIXAS experimental set-up, where b is the height of the beam, θ is the incident angle between sample and beam, and l is the length of the sample interacting with the radiation; w , the width of the beam is perpendicular to the view and is omitted

It must be stressed that, in order to perform the sample alignment and a correct spectral acquisition, a high level of flatness of the sample surface is required.

3 Electrodeposition and characterisation of palladium films as catalyst layers in Direct Ethanol Fuel Cells (DEFCs)

3.1 Introduction

Research in the field of energy production is today a hot topic, mainly due to the issues related to the increase in the extraction cost of fossil fuels, and thus to their low availability in the years to come. Renewable resources showed a promising alternative to the commonly employed coal and oil fuels, used to produce electricity, but still many technical issues have to be resolved in order to favour their widespread diffusion. Recently, particular interest was shown in respect to fuel cells²¹, devices capable of transforming directly the chemical energy embedded in renewable fuels into electrical power, without the various energy conversion steps needed in conventional combustion engines/turbines. In the most used power production processes, in fact, energy undergoes multiple stages of transformation to become electrical energy. A combustion of some sort has first to transform the chemical energy of the fuel in thermal energy, which is converted into mechanical energy and finally into electrical power. A clear example of this process is shown in turbine working principle for the transformation of the chemical energy embedded in a liquid fuel, into electrical energy:

1. *From Chemical energy to Thermal Energy*

Fuel, mixed with air (oxygen 21%) is burned in a boiler. The combustion leads to the release of energy in the form of heat, which is transferred to a liquid (usually water);

2. *From thermal Energy to Mechanical Energy*

The liquid incurs in phase transition thanks to the transferred heat, becoming a gas and increasing the pressure in the liquid circuit. The obtained hot gases are then conveyed inside the turbine chamber where, by expansion, they produce the rotation of the main turbine shaft.

3. *From Mechanical Energy to Electrical Energy*

The shaft is connected to a generator, which transforms the spindle motion into the flow of electrons inside a conductor.

Energy has to pass through three different transformations, each one with its particular yield, which conveys the energy loss incurred during the process. A total thermodynamic yield can also be calculated as a product of the yields related to the single transformations. This value can be theoretically assessed to about 60% for combustion engines, meaning that 40% of the initial chemical energy supplied to the system is mainly lost in form of heat.

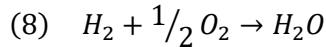
On the other hand, fuel cells are capable of transforming directly chemical energy into electrical energy, with a theoretical thermodynamic yield of more than 90%²², thanks to their working principle, identical to the one shown by galvanic cells. Fundamentally, fuel cells are composed (as galvanic cells) by a cathodic and an anodic compartment, linked by an electrolyte (usually in form of a polymeric membrane) which permits the passage of only certain ionic species in between the two half-cell entities. Different reactants flow onto cathodic and anodic surfaces, usually coated with a thin catalytical deposit. This layer is chosen to promote specific red-ox reactions with the fuel, in order to produce its transformation, and consequently the release/acquisition of electrons on the electrodes surface. This phenomenon leads to the establishment of a potential difference between the two compartments and permits the use of the fuel cell as a power generator. The electrical potential shown between anode and cathode will be given by the sum of the potentials related to the two half-cell reactions

(the thermodynamic reversible potential of the whole cell, related to the Nernst equation for each half-cell reaction) minus an overpotential term, related to the cell polarization, and in the end to kinetic factors²³. Power outputs of a single cell are usually too low to be used, for this reason, usually many cells are stacked to produce a battery, increasing voltage or current output, just like common portable Li-ion or alkaline batteries. Following this brief explanation of the working principle, it appears clear that the main difference between a fuel cell and a galvanic cell resides in the resupplying of the reactants. In fuel cells, we have a continuous flow of fuels, both on the cathodic and in the anodic compartment, rendering these cells in fact “open systems”. On the contrary, galvanic cells have instead only a certain amount of reactant available before their discharge. Another great advantage of these devices is related to the nature of the fuel used. A wide array of different fuel cells has been developed throughout the years; among them, the most promising ones exploit oxygen taken directly from the air mixture for the cathodic reaction, and hydrogen or alcohol for the anodic one. The use of these renewable chemicals to produce electrical power favoured the idea of fuel cells as “green” devices. But today some significant issues regarding both the technological and scientific aspects still limit their exploitation as large-scale devices.

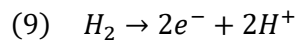
Part of the research undergone during my PhD has focused on one of these open issues, and mainly has regarded the study of the reactivity of palladium used as an anodic catalyst for ethanol electrooxidation, in direct alcohol fuel cells (DAFCs). In respect to platinum, palladium shows a good activity toward ethanol oxidation in an alkaline environment, a lower cost and a higher availability²⁴. Its use, in basic solutions, could lead also to other advantages, in fact, it permits to bypass the CO absorption phenomenon shown by Pt catalysts in acidic FCs (which hinders its reactivity)²⁵, and a more extended durability of the cell polymeric components. The main issue hampering the diffusion of Pd as electrocatalyst is related to its deactivation during working cycles, due to its oxidation²⁶. In this part of the thesis, to shed some light on this phenomenon, the results of two different synchrotron light experiments (MA-3173 and MA-3431), focused on the study of Pd deactivation phenomenon are shown, together with the experimental set-up preparation.

3.1.1 Fuel Cell Working Principle: The Hydrogen/Oxygen Cell

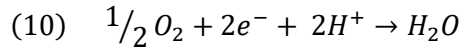
Hydrogen/Oxygen cells were among the first fuel cell systems to be developed and studied, and represent an archetypical example to better show the working principle of these devices. Here, a flux of hydrogen gas is led into the anodic compartment, while supplied oxygen reacts in the cathodic branch. The overall reaction led to water formation as a by-product, following the global reaction (8):



That can be split roughly into an anodic reaction (9) called *Hydrogen Oxidation Reaction* (HOR):



And into a cathodic one (10), called *Oxygen Reduction Reaction* (ORR):



It is worth to notice that the previous example is related to the working principle of Proton Exchange Membrane Fuel Cells (PEMFCs), the most common hydrogen/oxygen fuel cells. The particular feature of this class of cells resides in their membrane, which ideally permits only the passage of the H^+ species between the compartments. In these devices, in fact, the hydronium ion produced on the anodic catalytical surface migrates through the polymeric electrolyte membrane, to participate in the water formation reaction in the cathodic branch, with the external flow of 2 electrons for each water molecule formed. A scheme of the overall process can be also found in **Figure 17** and is suitable to explain the working principle of this kind of fuel cells.

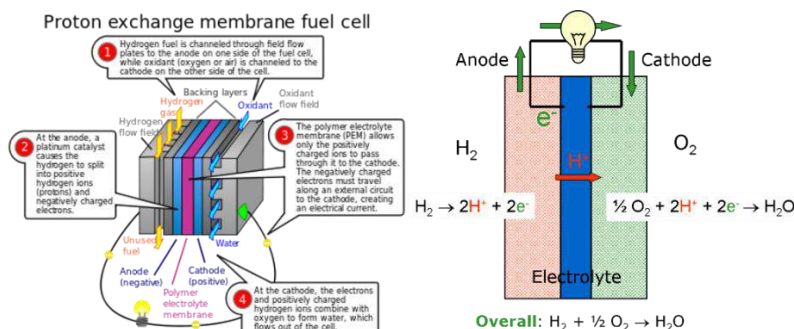


Figure 17 – The Hydrogen/Oxygen Fuel Cell working principle

Despite the simplicity of the processes involved, many important issues are related both to the handling of hydrogen as anodic fuel and to technical issues regarding the design of the cell.

As an example, hydrogen has to be obtained from water by electrolysis, following an energy expensive process (50 kWh kg^{-1}). Being a gas, it has also to be stored and supplied in pressurised containers. Hydrogen is flammable, and its usage as pressurised gas could lead to significant safety risks if not properly handled.

3.1.2 Fuel Cells Criticalities

Apart from fuel nature, various issues, both regarding technological and scientific aspects hinder a widespread diffusion of fuel cells. The first partition of these issues can be related to fuel cell components:

- Issues related to the Polymeric Electrolyte Membrane;
- Issues related to the catalyst in cathodic half-cell;
- Issues related to the catalyst in anodic half-cell.

3.1.2.1 The Polymeric Electrolyte Membrane

The *Polymeric Electrolyte Membrane*, which divides the two cell compartments, is an essential part of the fuel cell. Its role is to let the flow of only certain ionic species (usually H^+ or OH^-) in between the two compartments, hindering the exchange of fuel molecules or combustion by-products. These membranes could be considered in fact as selective filters, used to avoid crossover of species between the two cell compartments, a phenomenon that can be quite harmful to the durability of the catalysts. Different reactants could in fact irreversibly adsorb on catalyst's surface, or

even degrade it, lowering surface activity towards fuel molecules and thus decreasing cell performances. The nature of the chosen PEM usually is correlated to the environment in which FCs have to work, and on the reaction pathway, we want to follow. In alkaline fuel cells, the migration of hydroxyl ions will be usually requested, while in acidic fuel cells the hydronium ion will be transported from the anodic half-cell compartment to the cathodic one. Apart from their selective permeability, also membrane durability is an important topic. Liquid fuel cells have to endure in highly acid or alkaline electrolytes, sometimes at temperatures above 100°C. Corrosion issues are common on these polymeric layers, especially in an acidic environment; for these reasons, research is focusing on the development of selective and resistant membranes as exchange layers in fuel cells.

3.1.2.2 *Catalysts for Cathodic reactions*

The vast majority of the developed fuel cells uses oxygen as fuel for the cathodic reaction; this gas is, in fact, available abundantly in the air mix. On the other hand, Oxygen Reduction Reaction (ORR) is still a significant issue in electrocatalysis, because it limits greatly the energy efficiency of fuel cells, both acidic and alkaline. This because:

1. Oxygen is a potent oxidising agent, and only noble metals and alloys could withstand the highly positive potential associated with the reduction of this fuel without deactivating, by the formation of a surface oxide shell, or by dissolution.
2. ORR has a quite complex mechanics, with many reaction intermediates; ideally, O_2 could react to H_2O by a four-electron process, or produce H_2O_2 by a two-electron pathway. Usually, these two processes co-occur to a different extent. H_2O_2 production should be kept to a minimum because it provides less charge, and also because this product could be harmful to the cell.
3. ORR is a sluggish reaction, with a slow kinetics and a low exchange current density in respect of a wide array of catalytically active materials.

Many surfaces made of metals, alloys or organic molecules have been tested with respect to the ORR. Still, the best catalysts for the oxygen reduction reaction are constituted by platinum. On the other hand, Pt or Pt-based NPs are too expensive for their use in commercial fuel cells.

3.1.2.3 Catalyst for Anodic reactions

In the most common fuel cells, in the anodic compartment, some sort of dehydrogenation reaction occurs between the fuel and the catalyst; hydrogen in fuel molecules is being oxidized by the catalytic material, with the release of electrons onto the solid phase, together with spent fuel by-products. For anodic reaction, there are many different catalysts available, depending on the nature of the fuel used and on the pH, in which reactions took place. Platinum and platinum-based catalysts are addressed as the best choice also for the anodic reactions in hydrogen/oxygen fuel cells and in Direct Alcohol Fuel Cells (DAFCs). This metal shows a great activity towards dehydrogenation of alcohols in acidic media²⁷, with the only drawback of its deactivation caused by the irreversible absorption of CO on its surface^{28–30}. Again, Pt cost and availability pose a serious limit to its exploitation in anodic compartments of these devices.

3.1.3 Direct Alcohol Fuel Cells (DAFCs)

Direct Alcohol Fuel Cells (DAFC) show a lower level of criticality in fuel handling in respect to hydrogen/oxygen cells:

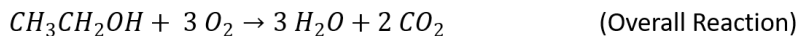
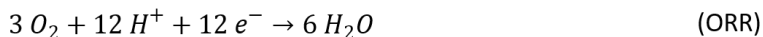
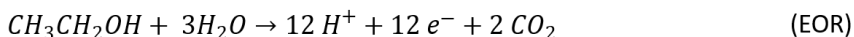
1. First of all the used fuels, like methanol, ethanol, propanol, glycerol, etc. are liquid at room temperature. Also, as the name suggests, alcohol is supplied directly to the anodic compartment in the form of concentrated acid or alkaline solutions, depending on the nature of the catalyst involved, and on the reaction pathway, we want to follow.
2. Also, the process used for alcohol production and refining is less energy expensive with respect to water electrolysis.

In these cells, oxygen reduction reaction is commonly exploited as a cathodic reaction, while in the anodic compartment the dehydrogenation of the alcohol occurs, with the aim to produce its complete degradation to CO₂ and H₂O. This process is difficult to achieve, and depends strongly on pH, on the nature of the catalyst and on the fuel used, and on the whole cell potentials.

3.1.4 Alkaline Direct Ethanol Fuel Cells (ADEFCs) & Ethanol Electrooxidation reaction

Increasing interest in ethanol is shown due to its higher availability, its renewable nature and its well-established distribution infrastructure. For these reasons, *Direct Ethanol Fuel Cells (DEFCs)* are the most promising cells along all the DAFCs. The main aim of these cells is the complete degradation of ethanol in the anodic branch, with the breaking of the C-C bonding and the formation of solely H_2O and CO_2 , following the *Ethanol Oxidation Reaction (EOR)* in the anodic branch, and the *Oxygen Reduction Reaction (ORR)* previously seen in the cathodic branch. Depending on the fuel cell working pH, a distinction between two different sets of EOR/ORR reactions can be made (**Figure 18**).

Acidic DEFCs



Alkaline DEFCs

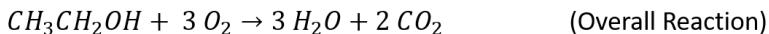
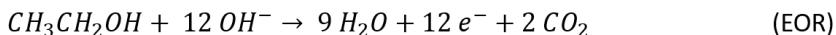


Figure 18 – Difference in reactivity between acidic and alkaline DEFCs

Sadly, a complete ethanol degradation which led to the formation of CO_2 and H_2O through a $12e^-$ pathway is difficult to achieve, due to the particular conditions needed to cleave the C-C bond. Usually, two by-products are produced during reaction³¹ (**Figure 19**):

- CH_3CHO (acetaldehyde) through a $2e^-$ pathway;
- CH_3COOH (acetic acid) through a $4e^-$ pathway.

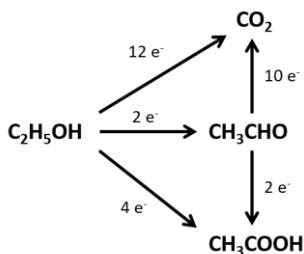


Figure 19 – Ethanol electrooxidation pathways

The breaking of the C-C bond, leading to the formation of CO_2 can be hindered by the absorption of CO, one of the oxidation by-products, as visible in **Figure 20**. The nature of this irreversible CO absorption blocks, in fact, the catalyst surface, making it impossible to adsorb further ethanol molecules, and then halting the *EOR*. This phenomenon, commonly occurring on Pt catalysts in acidic environment³², could be prevented by reaction between CO and a surface hydroxyl group, leading to the formation of a gaseous CO_2 molecule. For this reason, this reaction could be only favoured in the acidic environment, by tailoring also the surface nature (as an example by preparing bimetallic Pt- CeO_2 catalysts^{33,34}, while, it is impossible to achieve in alkaline media at pH above 13³⁵.

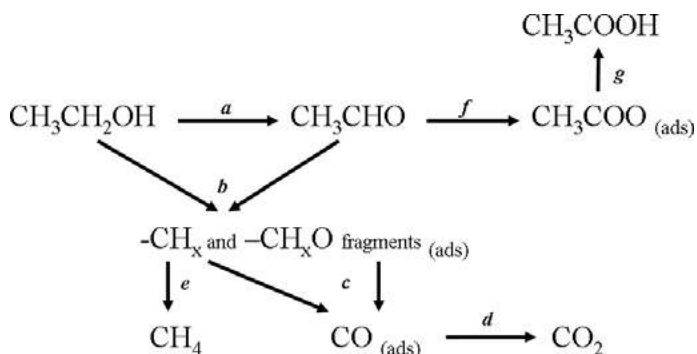


Figure 20 – Reaction pathways for the ethanol oxidation on a Pt surface in acidic media

Into the anodic compartment of alkaline DAFCs, only acetaldehyde, or acetate could be selectively formed, rendering these cells also usable for the production of specific chemicals of industrial interest³¹. The mechanics for these reactions in alkaline media is shown in **Figure 21**.

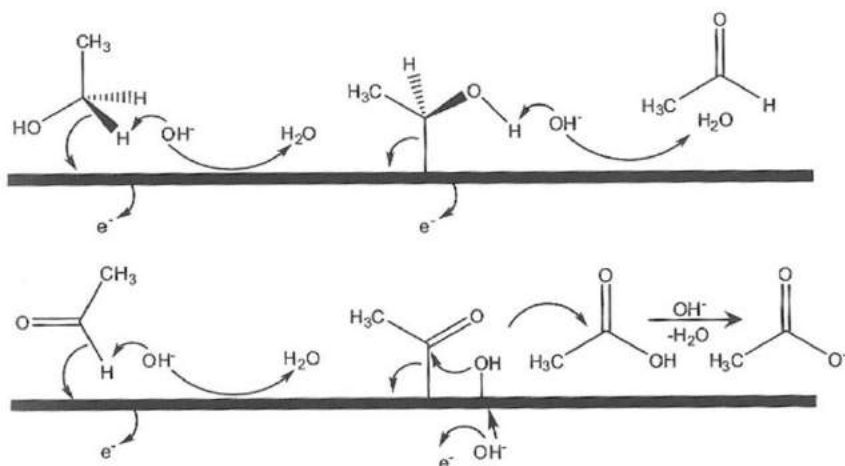


Figure 21 – The proposed reaction mechanics of ethanol oxidation in alkaline media (pH > 13), leading to the formation of acetaldehyde (upper row) and acetate (lower row)

A big advantage in working in alkaline media is related to the feasibility to use different catalysts in respect of Pt. Particularly palladium showed a higher activity towards the *EOR* reaction in alkaline media^{24,35,36}, even greater than platinum in this environment. This, together with Pd lower cost and higher availability made this metal a viable catalyst alternative for alkaline DEFCs. At this point, the only limit to its employment resides in the deactivation phenomenon which occurs under working conditions, a phenomenon still not completely understood^{26,37}. It is in fact still not clear if the deactivation mechanism leads to the formation of a reversible oxide scale on the catalyst surface, if some kind of catalyst dissolution occurs, or if both the phenomenon are present at the same time. Also, a comprehensive study of the oxidation conditions (pH, alkali and fuel concentration, working cycles and potentials) is still lacking.

3.1.5 Palladium electrochemical behaviour in alkaline media

To study the deactivation phenomenon which occurs on palladium surfaces during fuel cells working cycle, some results regarding the Pd electrochemical behaviour have to be shown. Some studies were performed^{38,39}, mainly using electrochemical methods (like cyclic voltammetry), defining palladium reactivity in various alkaline and alkaline + fuel electrolytes. These studies evidenced the formation of Pd (II) species at potentials higher than 0.6V vs RHE, for both the fuelled and unfuelled

solutions. **Figure 22**³⁹ shows a CV performed using a Pd polycrystalline surface as working electrode, a Pt foil as counter electrode and a Hg/HgO/KOH electrode (0.098V vs SHE) as a reference electrode. The electrolyte used was a NaOH 1M solution (pH~14), and the test was performed with a scan speed of 20 mV/sec.

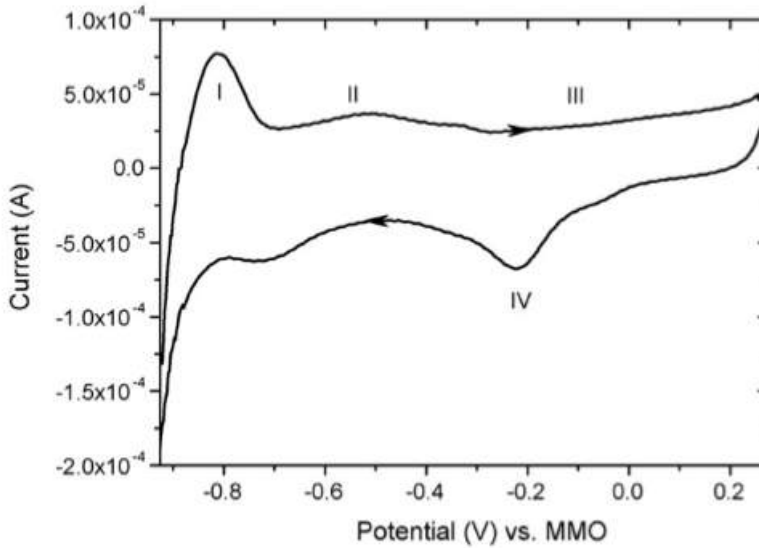
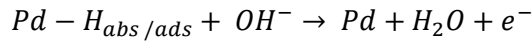


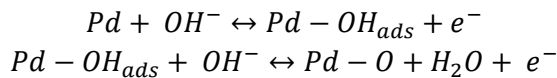
Figure 22 – Cyclic Voltammetry of a polycrystalline Pd surface in a NaOH 1M solution, scan speed 20mV/sec

From the image, four peaks can be identified:

- I. Peak related to the oxidation of the adsorbed or absorbed hydrogen on the Pd Surface (from -0.90V to -0.70V);

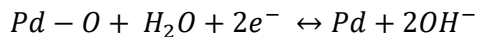


- II. Peak related to the overlapping of the OH^- absorption phenomenon, together with H_2 desorption;
- III. Peak attributed to the oxidation of Pd surface (from -0.25V to higher potentials). OH^- ions chemisorbed on the surface, transform into higher valence oxides at higher potentials;





IV. Peak related to Pd(II) reduction during the cathodic sweep:



The introduction of the ethanol in the alkaline electrolyte leads to the appearance of two new peaks, one during the cathodic scan and one in the anodic scan. Cyclic voltammetries performed in a NaOH 1M + EtOH 1M electrolyte (black) and NaOH 1M electrolyte (red), performed using the same thin layer Pd WE, an Ag/AgCl KCl sat. RE and a graphite CE are shown in **Figure 23** (scan speed 50 mV/sec).

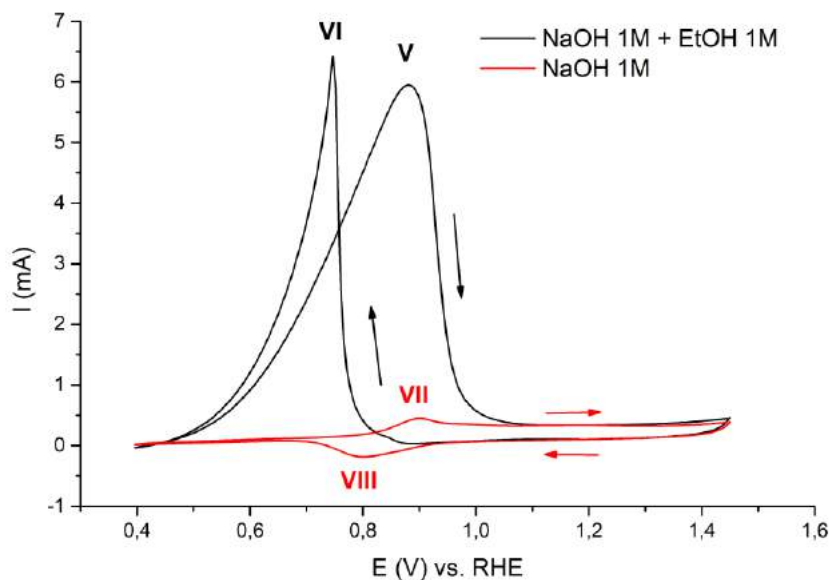


Figure 23 – A comparison between CVs performed using a Pd thin layer in NaOH 1M + EtOH 1M (black) and NaOH 1M (red); the second curve shows similar features with respect to the one shown in **Figure 22**

From this image new peaks can be identified:

- V. Anodic peak related to the oxidation of ethanol during the forward scan; this phenomenon is hindered by the deactivation of the catalytic surface, which is completed at potentials above 1.00V vs

RHE (formation of a layer of Pd(II) species above the electrode surface);

- VI. Anodic ethanol oxidation peak related to the reactivation of the catalyst, due to Pd(II) reduction to metallic Pd at potentials of about 0.80V vs RHE (see point VIII);
- VII. Anodic peak related to the *III* peak shown in **Figure 22**;
- VIII. Cathodic peak associated with the *IV* peak shown in **Figure 22**.

The comparison between these last two curves helps to understand the deactivation process. The decrease in the catalytical activity during the anodic scan (after peak V.) is paired with the oxidation of the Pd (peak VII.). On the other hand, during the cathodic scan, the reboot of the ethanol oxidation process (peak VI.) is related to the reduction of the Pd (II) to Pd (peak VIII.).

3.2 The FEXRAV Experiment

FEXRAV technique was used during ESRF experiments MA-3173 and MA-3431 to acquire the joint spectroscopic and electrochemical data of various metallic catalysts with respect to ethanol electrooxidation reaction. Pd, Pd/Au, Pt, Pt/Ru, Pt/Au nanoparticles, all dispersed in a carbonous matrix, were tested as working electrodes both in a half cell and in a full cell set-ups. Their electrochemical behaviour was examined using different electrolytes, from basic ones (KOH 2M) to alkaline electrolyte + fuel (ethanol or formiate). These experiments aimed to define a correlation between the red/ox behaviour of the metals, their reactivity toward catalytical reaction, and the deactivation process.

Extensive work was done particularly with respect to Pd used as a catalyst for the anodic reaction in Direct Alcohol Fuel Cells. This case has been selected for the well-known chemistry of palladium in an alkaline environment that, at potential larger 0.5 - 0.6 V RHE and smaller than 1.2 V RHE is oxidised to Pd(II) species. Under such circumstances, the palladium nanoparticles dispersed onto the carbon support is expected to present a shell of Pd (II) oxo-bridged compounds and a core of metallic Pd. It is well-known that palladium incurs into deactivation in alkaline fuel cell operative conditions, by oxidation from Pd⁰ to Pd²⁺. Still, it remained unclear whether

this deactivation is led by the formation of an oxide scale, or by a dissolution phenomenon which occurs on the NPs surface.

3.2.1 The FEXRAV Cell

The electrochemical cell was explicitly designed to work on the BM08 beamline and was already used for other experiments. Part of my work was focused on an upgrade of its design, to improve the experimental set-up efficiency for the Pd tests. A schematic view of the cell can be seen in **Figure 24-A**. It is made of PMMA, and can be divided into two pieces, a body and a head:

- The body contains the solution tank, together with various holes which permit the introduction of the CE and the RE, and the bubbling of gases into the liquid. The cylindrical hole that constitutes the solution tank has a radius of 10 mm and a depth of 52mm. A support screw permits the mounting of the cell on the movable support of the sample chamber;
- The cell head has a central hole to allow the free passage of the beam. Its purpose is also to block the sample on the o-ring of the body, to seal the cell.

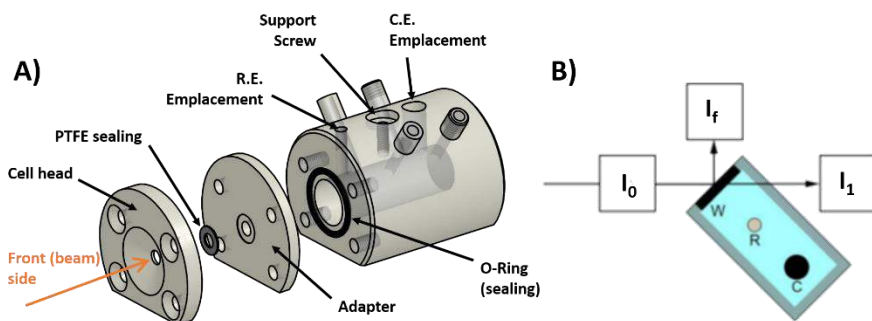


Figure 24 – A) The used FEXRAV cell, B) the top view of the cell placement with respect to the incident beam (W working electrode, R reference electrode, C counter electrode).

The cell was designed to work mainly in fluorescence mode, by adopting a 45° inclination with respect to its vertical axis (**Figure 24-B**).

3.2.2 Samples preparation & Chemicals

The catalyst nanopowder used as working electrode was synthesized at the ICCOM-CNR in Florence^{40,41}. It was made by Pd nanoparticles with a

diameter of about 5 nm, dispersed in 10% weight ratio in a carbonous powder. To prepare the working electrode, an ink composed by 100 mg of catalyst, 400 mg of water and few drops of a 5% wt. alcoholic Nafion solution was prepared. Just after a sonication process, the ink was delivered on a carbon cloth surface, to obtain a catalytical surface with a 4 mg/cm² Pd loading, and placed on the cell head to be employed as a working electrode. The use of copper tape on the free surface of the carbon cloth allowed the electrical contact between the drop-casted ink and the potentiostat. The procedure used to prepare the WE can be seen in **Figure 26**, where:

- a) This figure depicts all the pieces needed for the cell assembly;
- b) The carbon paper is centred on the cell head, a small piece of copper tape is connected to the conductive paper;
- c) The adapter is closed on the cell head assembly and centred by the fixing screws. The PTFE sealing is placed between the adapter and the carbon paper as a sealing;
- d) Preparation of the Pd ink;
- e) The ink is delivered to the central spot of the adapter by drop casting;
- f) The weight difference before and after the drop-casting process permits to define the catalytic Pd load.

Solutions used during the experiment and the reagents used are summarized in **Figure 25**.

| Use | Solution | Chemical | Product, purity, dealer |
|--|---------------------|----------|--|
| <u>Ethanol</u> <u>oxidation</u> <u>tests</u> | KOH 2M | KOH | >98%, Fluka |
| | KOH 2M + EtOH 2M | EtOH | AnalaR Normapur, 99,9%, WWR Chemicals |

Figure 25 – Reagents used for the FEXRAV experiment

The solutions were used undisareated in order to reproduce the real working conditions of a fuel cell. This led to a specific oxygen content onto the solution bulk that sometimes was seen as a cathodic discharge on the working electrode.

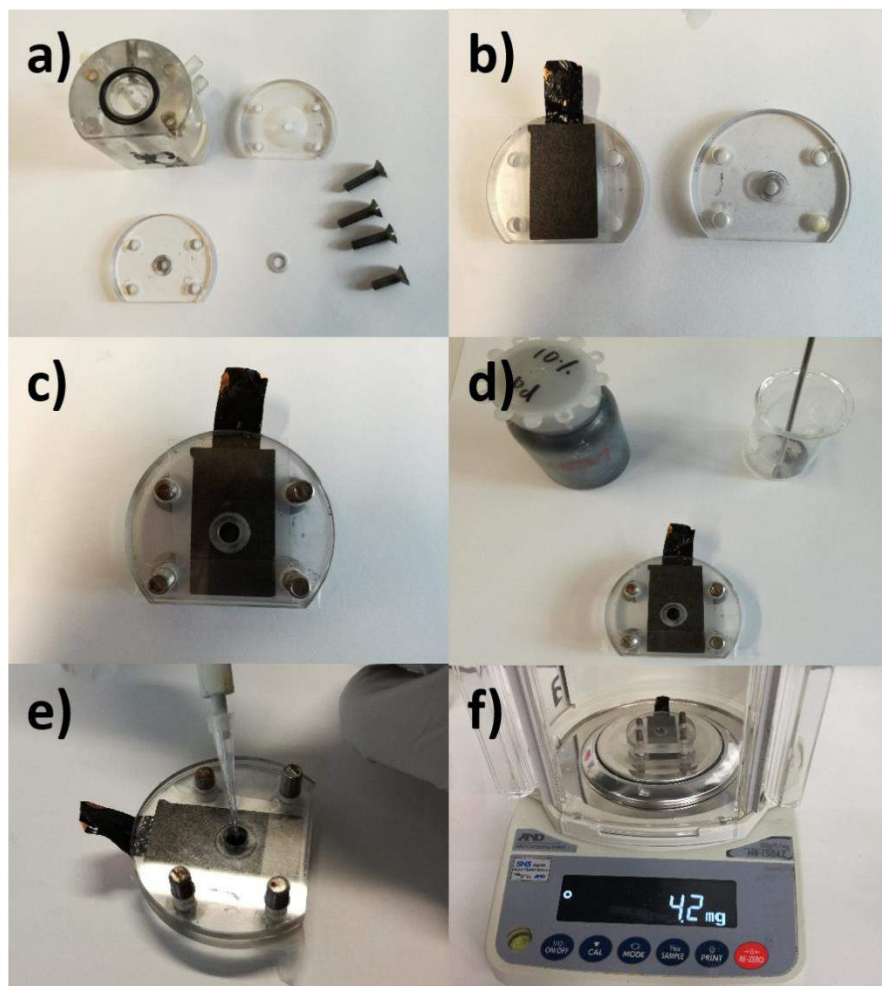


Figure 26 – WE preparation for the FEXRAV experiment

The upgraded cell also permits its use as a full fuel cell, coupling the Pd-C anodic catalyst with a cathodic catalyst for the reduction of O_2 , and adopting the particular set up visible in **Figure 27**. During the experiments, some full cell test acquisitions were made using a pyrolyzed (600 °C) Fe-Co phthalocyanine cathodic catalyst⁴² supported on K-gen Black, and a Fumateck alkaline ionic exchange membrane. The cell set/up worked correctly (see **3.2.5**) and opened the path to further in situ catalytic tests.

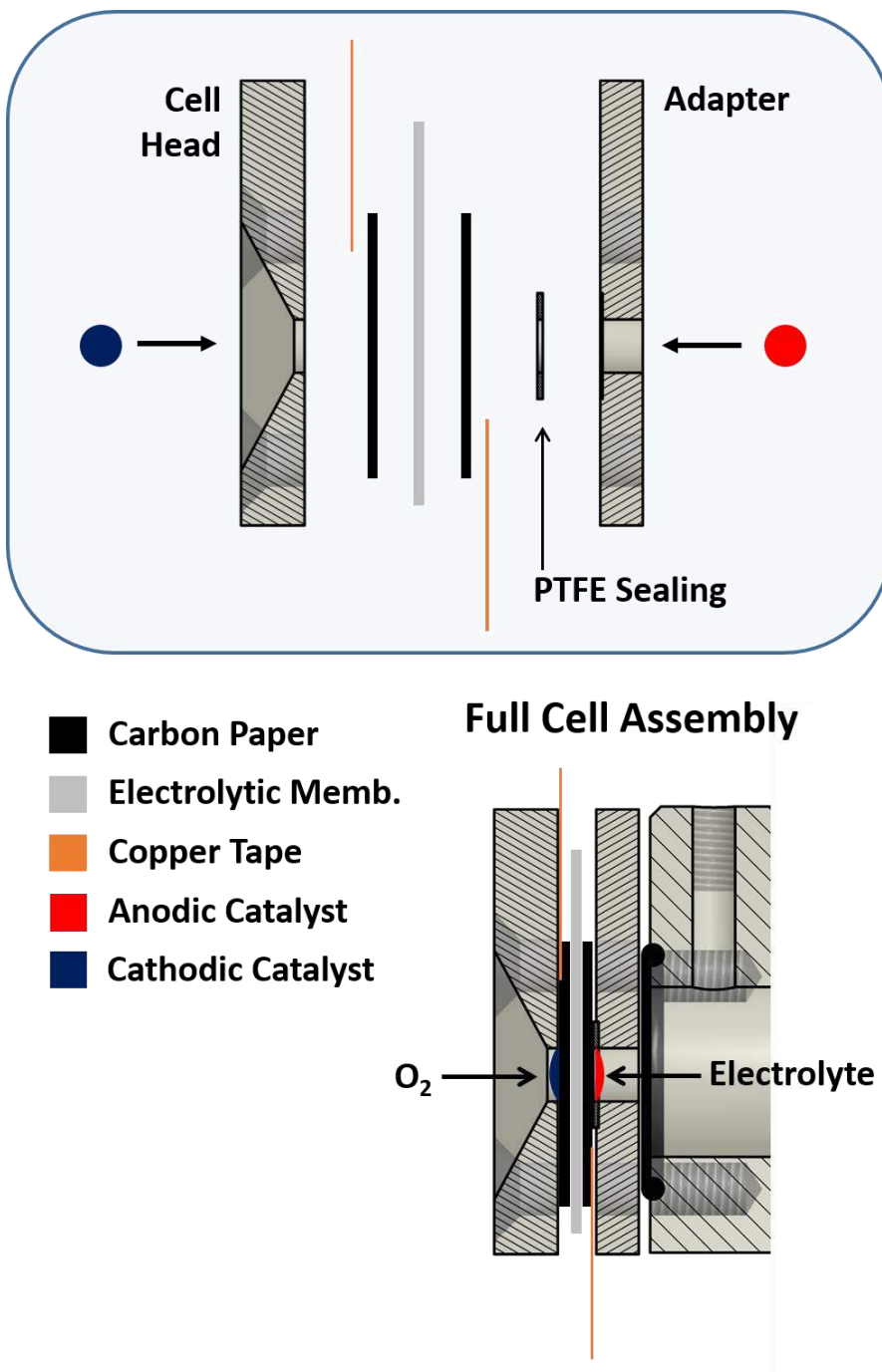


Figure 27 - Cell section depicting the set-up used to prepare the full fuel cell; thicknesses of the various layers are exaggerated for the sake of clarity

3.2.3 Experimental Set-Up

For the FEXRAV experiments, a beam energy of 24370 eV was used (an energy value in which differences between absorption of Pd and Pd(II) are maximised, see chapter **3.2.4**). Two ionization chambers, placed before and after the experimental chamber, permitted the normalization of the incident beam energy, thus eliminating the variations due to the decreasing of the current in the storage ring between two refills.

For the electrochemical acquisitions, a PAR 263 potentiostat was placed directly in the experimental hutch, permitting its use from the control room thanks to the SPEC interface. Ag/AgCl KCl sat. and a graphite rod were used as RE and CE respectively. Voltammetric scans were performed from 0.2 V to 1.2 V vs. RHE, at a scan speed of 1mV/sec.

3.2.4 Beam Energy Selection & Detection Limit

The feasibility of a quantification of the molar fractions of Pd⁰ and Pd(II) from a FEXRAV measurement resides in the correct evaluation of the changes in the spectral intensity $I(E)$ at a given energy value. Preliminary acquisition was then performed, using XAS technique on Pd(0) and Pd(II) standards. A Pd foil (considered as 100% metallic Pd) and a PdO foil (considered as 100% Pd(II)) were used as targets to define the energy on which the higher absorption change between the two oxidation states was visible. Various intermediate compositions were then calculated through a weighted linear combination of the two reference spectra.

From the obtained elaboration (**Figure 28**) in which the XAS spectra were normalized by the unitary edge jump, three considerations arose:

- The absorption edge shifts to higher energy values for Pd samples, with respect to the Pd(II);
- Two features, at 24370 and 24390 eV, respectively, exhibit an opposite behaviour. The intensity of the first peak increases with the increase in Pd(II) content, while the second one increases with the rise in the Pd content. The change for the 24370 eV is higher in intensity with respect to that at 24390 eV. Thus, we considered the former more useful for analytical purposes;
- The change in normalized intensity seems to vary linearly with the increase of the Pd(II) content.

Once defined the experimental energy, an esteem of the detection limit was performed by the comparison of the maximum variation of the fluorescence yield with its standard deviation at a constant energy value. The fluorescence signal at 24370 eV was then acquired for NPs sample kept inside the cell in open circuit potentials conditions, using a scan time of 800 seconds. From the obtained data series (**Figure 29**) it was possible to extrapolate the mean root square, and consequently an uncertainty of the order of 1% with respect to the signal. From other tests, it has also been seen that this value remained constant in a ± 50 eV range concerning the energy related to the edge jump. This amount was then considered as a limit value for the determination of Pd(II).

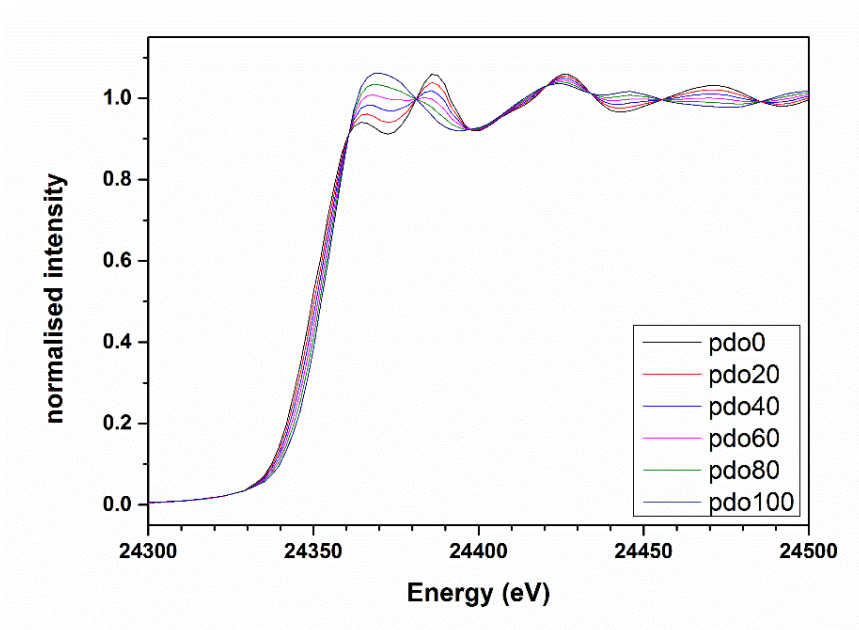


Figure 28 – The XANES spectra obtained by the standards, together with the ones theoretically calculated for different Pd/Pd(II) ratios.

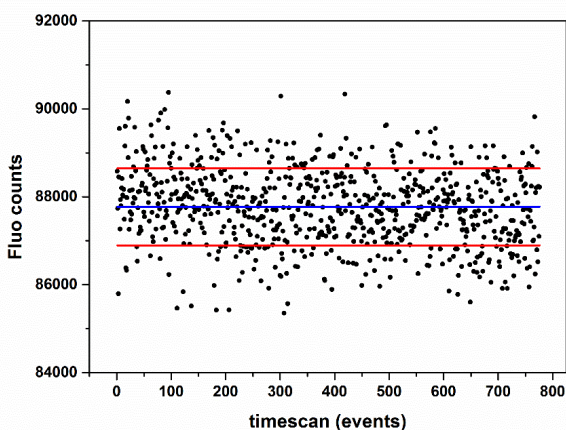


Figure 29 – The fixed energy scan performed at 24370 eV for the nanoparticled palladium under open circuit conditions

3.2.5 Results

3.2.5.1 Half-Cell Measures

Two series of data acquisitions were performed by the half-cell set-up performing voltammetric scans from 0.0V to 1.4V vs. RHE at a scan speed of 1mV/sec; two different electrolytes were tested:

- KOH 2M;
- KOH 2M + EtOH 2M.

Before each new experiment, a new electrode was prepared. It must also be reminded that at the chosen fixed beam energy value (24370 eV), the increase in the fluorescence yield is related to an increase in Pd(II) species, while its decrease is associated with the presence of metallic palladium.

First of all is worth to notice the trend of the Fluorescence yield-potential vs. time plots of these experiments. In both of the FEXRAV experiments performed using KOH 2M (**Figure 30**) and KOH 2M + EtOH 2M (**Figure 31**) as electrolytes, a definite diminishing of the XAS signal is visible in time. This phenomenon could be correlated with an effective decrease of the palladium loading on the electrode, due to the detachment of the catalyst from the working electrode surface, or to the cyclic oxidative stress induced by the positive potentials cycling, and thus to dissolution. The diminishing of the catalyst loading was also confirmed by the trend of the current during cyclic voltammetries. All the voltammetric cycles of the tests performed

using the alkaline electrolyte solely, and the electrolyte + fuel are shown in **Figure 32** and **Figure 33** respectively. In both these figures, a flattening of the curves (diminishing in peak current) is visible with the increase in the cycle number, a congruent phenomenon with the decrease of the Pd loading on the WE. It is also interesting to notice that, while in **Figure 32** the decrease in current intensity could be related to the decrease of the catalyst activity towards oxygen reduction, for the alkaline + fuel electrolyte (**Figure 33**) a current decrease in between the voltammetry cycles can be seen only in the forward scan (0.9V vs RHE), and no clear trend can be defined for the reverse scan peak (**Figure 33**, inset graph).

In the end, in **Figure 34** and **Figure 35**, the trends of both the current and the fluorescent yield for the first voltammetric cycle are reported.

From the obtained data, one thing must be pointed out. A continuous and linear decrease in the fluorescence trend can be seen for the KOH 2M Fluorescence Intensity/Potential vs time plot (**Figure 30**), attributable to a continuous decrease in the Pd loading, cycle after cycle. A similar trend was seen for the data related to the KOH 2M + EtOH 2M scans (**Figure 31**), but only for the first 4 cycles. From the 5th cycle on, a steady state was reached, with no substantial variation of the maximum and minimum fluorescence intensity between the cycles. This plateau could be possibly due to the effect of ethanol on the reduction of the Pd ions present in solution. Ethanol is in fact used as reducing agent during palladium nanoparticles preparation^{39,40}. The steady state could be then explained as it follows:

- The electrochemical oxidative stress leads to Pd dissolution, and consequently to the increase in concentration of Pd(II) into solution;
- The increase in concentration of Pd(II) triggers the ethanol-induced reduction reaction;
- At some point (here, after the 4th voltammetric scan) the ratio of the two process reaches an equilibrium.

The presence of a steady state can then be justified as a balance between the ratio of Pd electro-induced dissolution and Pd(II) ethanol chemically induced reduction.

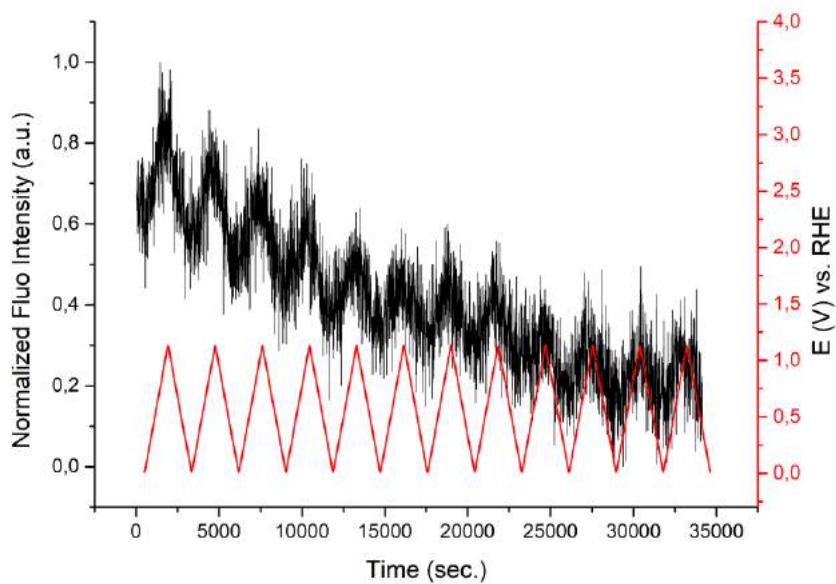


Figure 30 – Plot of the Fluorescence yield/potential vs. time for the test performed in KOH 2M electrolyte

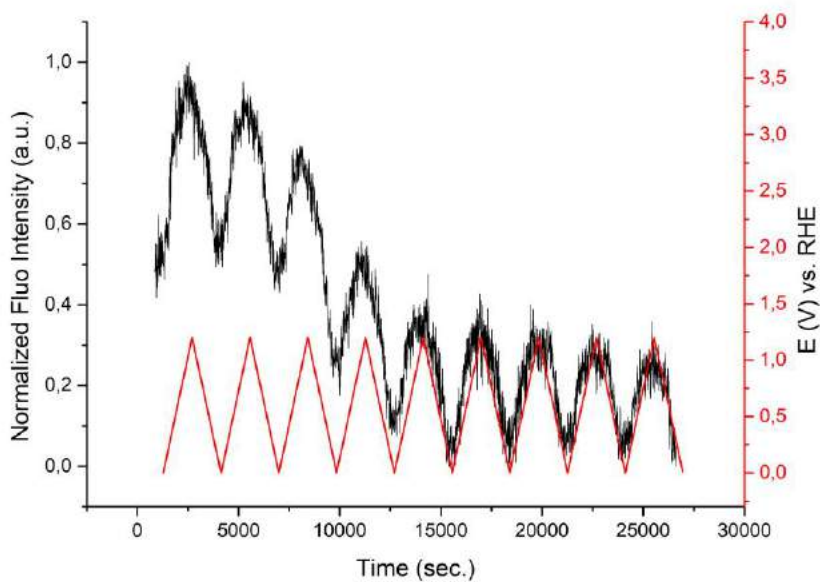


Figure 31 – Plot of the Fluorescence yield/potential vs. time for the test performed in KOH 2M + EtOH 2M electrolyte

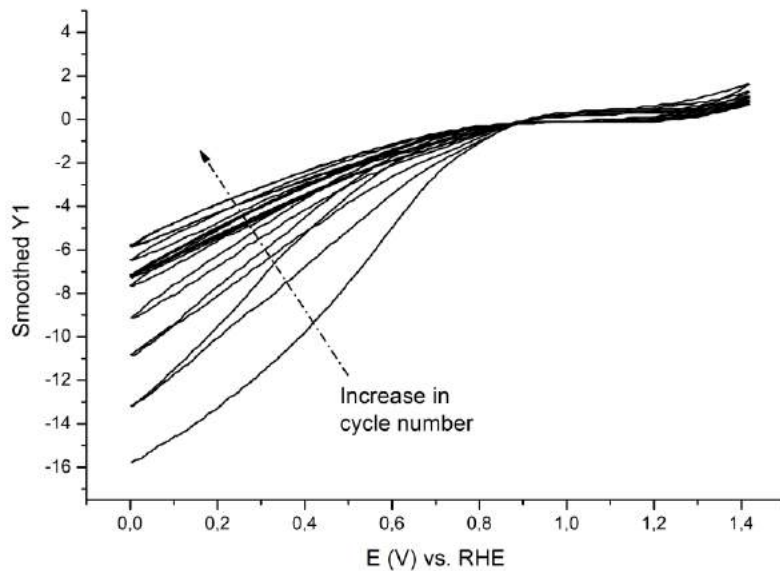


Figure 32 – Voltammetric trend of the test performed in KOH 2M electrolyte

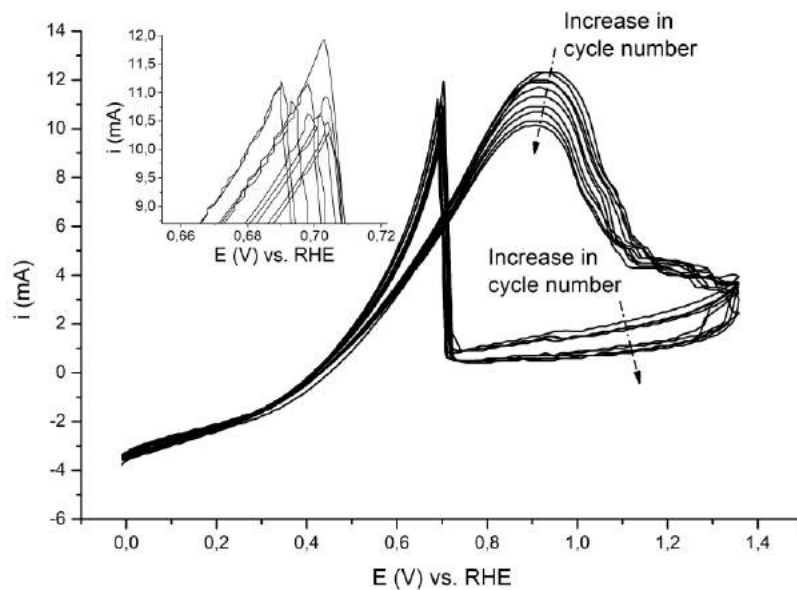


Figure 33 – Voltammetric trend of the test performed in KOH 2M + EtOH 2M electrolyte

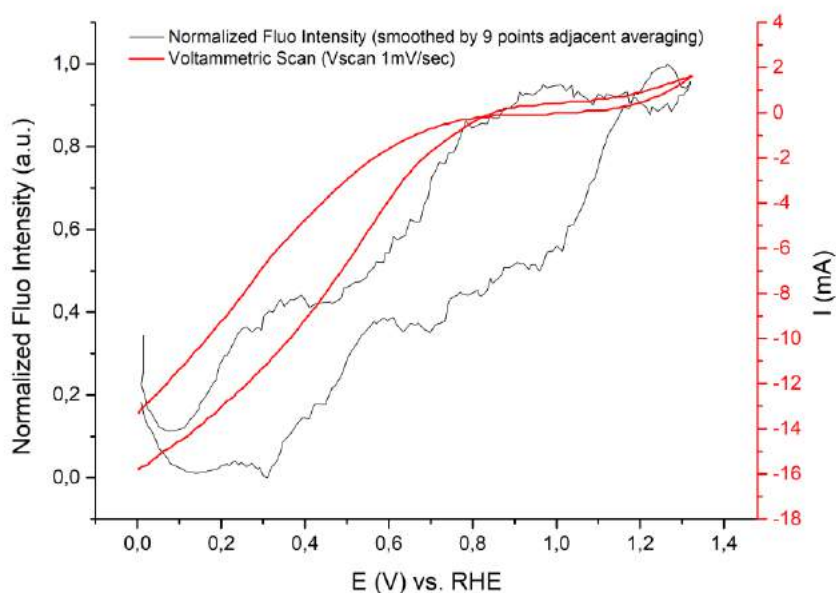


Figure 34 – Plot of the fluorescence yield/current vs. potential for the 1st voltammetric cycle performed in KOH 2M electrolyte

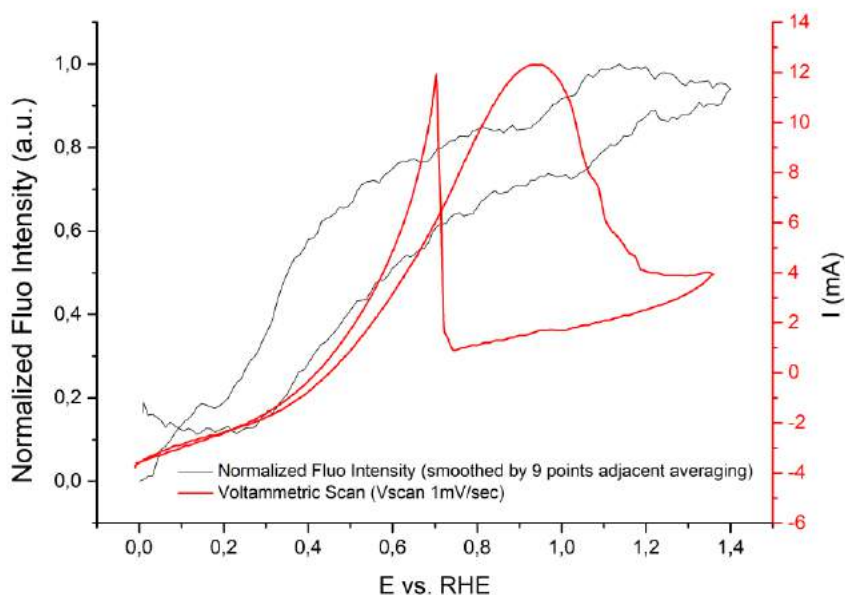


Figure 35 – Plot of the fluorescence yield/current vs. potential for the 1st voltammetric cycle performed in KOH 2M + EtOH 2M electrolyte

3.2.5.2 Fuel Cell Measures

A FEXRAV experiment was also performed in the full fuel cell configuration, using the abovementioned alkaline + fuel electrolyte and experimental set-up. The Fluo Int./Potential vs. Time plot of this experiment can be seen in **Figure 36**. A fluorescence trend similar to the one seen in **Figure 31** (for the half-cell experiment in the same electrolyte) is noticeable. Of particular interest the trend of the fluorescent signal at the end of the voltammetric cycles (after five hours), where the cell was maintained at its open circuit potential (OCP). An important increase in fluorescence intensity was visible under these conditions, meaning an increase in the Pd content on the sampled electrodic volume. This phenomenon was in accordance with the results obtained in the half-cell set-up for the same electrolyte. Again, chemical deposition (induced by ethanol) probably occurred, this time without the electrochemical dissolution effect induced by voltammetric scans.

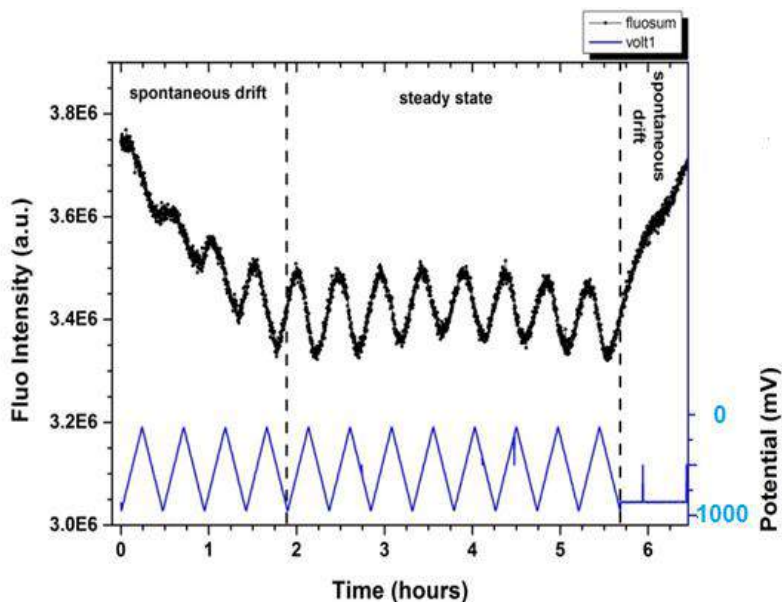


Figure 36 – The Fluorescence variation during the various CVs in the full fuel cell set-up, using KOH 2M + EtOH 2M electrolyte; the potential is related to Ag/AgCl KCl sat.

3.2.6 Study on Pd deactivation using FEXRAV and Computational Speciation Models

Data acquired during the FEXRAV experiments were compared to a theoretical Pourbaix diagram and coupled with a computational speciation model prepared using the Phreeqc software, specifically designed for such calculations. The aim of this work was mainly to shed some light on the nature of Pd in this particular aqueous environment during the potential change, especially regarding the form in which the palladium deactivates. The theoretical models suggested the formation of the Pd(II) hydroxo complex $\text{Pd}(\text{OH})_4^{2-}$ during the anodic scan, a result that confirmed the dissolution process. The entire article can be found in *Appendix A: Article "Computational Speciation Models: A Tool for the Interpretation of Spectroelectrochemistry for Catalytic Layers under Operative Conditions"*.

3.3 The GI-FEXRAV Experiment

3.3.1 Why combining GIXAS and FEXRAV?

FEXRAV technique proved to be a powerful instrument to study the chemical behaviour of catalysts during the electrochemical stimulus. Thanks to this technique we were able to follow the chemical evolution of Pd in the whole water electrochemical window. However, the use of this method to study dispersed systems could show a limitation. Nanoparticles are in fact well known for their high surface to volume ratio. This means that a portion of the single particle, generally the outer shell, participates in the electrochemically induced reactions, while the core remains untouched. Still, the incident x-ray samples all the catalyst volume; the output XAS signal could then be mediated by the centre of the particle. This phenomenon, dependent on the particle size, leads to lower signal to noise ratios and finally to slower acquisition times for the XAS spectra. A practical example regarding the used Pd nanoparticles can then be addressed. Previous studies^{33,43} on these nanodispersed systems showed that the voltammetric cycling led only to the oxidation of a few Pd layers on the surface of the particles, resulting in smaller differences between the fluorescence absorption signal attributed to the Pd^0 and the one assigned to the Pd^{2+} . In principle then, the chemically active volume can be increased, decreasing NPs dimensions down, till the obtainment of particles constituted by few

atoms, all of them participating in the chemical processes. Such small clusters are not easy to prepare and stabilize by chemical synthesis but could be grown directly on surfaces, using electrochemical deposition, as an example by forming 2D ordered structures. Mainly Under-Potential Deposition phenomenon, a well known technique by our group at the University of Florence, could be exploited to prepare and design catalytical atomic layers or submonolayers. At this point, a new problem could arise; monolayered systems could not be studied efficiently using the standard FEXRAV set-up, in which the beam is focused on a small sample spot. As an example, during the previous FEXRAV experiments with the Pd NPs, an incident beam of 2 mm x 0.5 mm hits the sample at 45°; this means that the beam covers an area of about 1.41 mm² with a rough Pd loading of 4 mg/cm², resulting in a number of irradiated Pd atoms of $3.19 \cdot 10^{18}$ (only a little fraction of them, from 10% to 40% participates effectively to the catalytical process). The same irradiated surface of a monolayer of Pd atoms contains roughly about 10¹³ atoms, a number five orders of magnitude lower in respect to the NPs sample, and this leads to a lesser number of absorption phenomenon and a lower fluorescence yield consequently. To increase the output signal intensity, XAS grazing incidence technique (GIXAS) could be used. This method permits to sample entirely very thin layers, using a beam with a very low incident angle with respect to the sample surface and, thus, is perfect to study monolayers. Angles below 0.5° (the value usually adopted for GIXAS) between the x-ray beam and the sample permit, in fact, to irradiate a more significant sample portion, thus enhancing the output fluorescence signal intensity. As an example, considering the same beam parameters used for the previous calculations (2 mm hor. x 0.5 mm vert.), and a beam hitting a horizontal Pd monolayered surface with an angle of 0.5°, the irradiated area results in about 114 mm², thus exciting more than 10¹⁵ atoms, two orders of magnitude more in respect to the same sample analysed in the 45° set-up. The irradiated sample area could be further increased by the use of smaller incident angles or by different beam dimensions, leading to a number of excited atoms far higher with respect to the 10¹⁸ atoms previously seen for the nanoparticle ink, at the cost of a vast irradiated area.

In the end, the combined use of GIXAS and FEXRAV (from now on called **Grazing Incidence FEXRAV** or **GI-FEXRAV**) could ideally permit to overcome

the limitations due to nanoparticles surface to volume ratios, by sampling all the electroactive volume, and to increase the intensity of the fluorescent signal by exciting a more significant amount of sample atoms in respect to traditional FEXRAV. To couple these two techniques, two final issues related both to the electrochemical cell design and to the catalytical surface preparation had to be resolved (**Figure 37**):

- **The experimental cell has to be redesigned, to permit its simultaneous use as an electrochemical cell and as a grazing incident support;**
- **Ordered model Pd catalytically active surfaces, with a wide area and a very thin palladium layer, had to be prepared.**

In the following chapters of this thesis the work done to prepare the GI-FEXRAV experiment is reported, together with the first experimental data obtained using this technique.

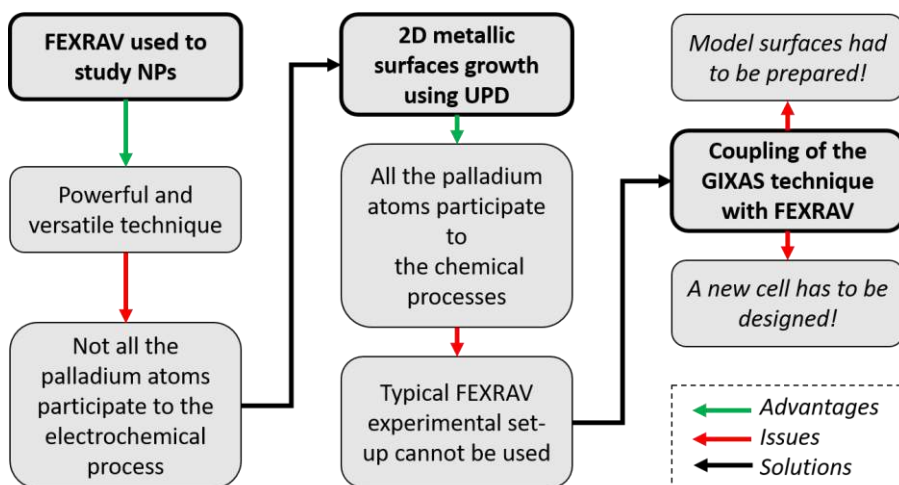


Figure 37 – A flowchart showing the various issues encountered during the GI-FEXRAV experiment preparation

3.3.2 GI-FEXRAV cell

The cell used for the GI-FEXRAV experiment was designed and commissioned by me, to overcome the particular sample placement required for the experiment. The following criteria were considered during cell drawing:

- 1) The catalytical surface has to be placed face up on the bottom of the electrochemical cell;
- 2) An extended electrode surface has to be exposed inside the solution, in order to permit the lower possible angle for the grazing incidence measurements;
- 3) Cell walls has to be as thin as possible on the side of the fluorescence detector, in order to minimize the radiation scattering due to the plastic barriers;
- 4) The conductive film on the glass has to be present both inside and outside the electrochemical cell, in order to permit a stable electronic contact with the potentiostat, without introducing other metals inside the solution;
- 5) The conductive film area has to be minimized, in order to decrease output current during cyclic voltammetries, and then preventing potentiostat current channel saturation. No electrode has to be on the path of the beam.

In order to overcome all these criticalities, the design that can be seen in **Figure 38** and **Figure 39** was finally adopted.

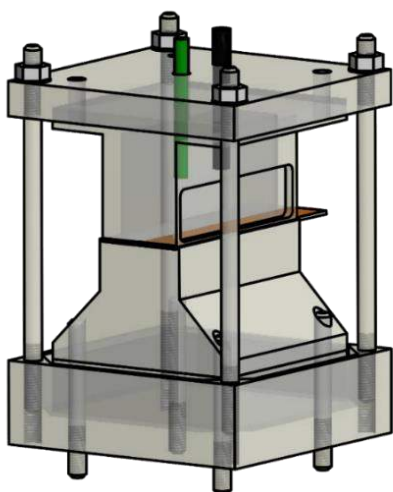


Figure 38 – From the cell design (left) to the commissioned cell (right)

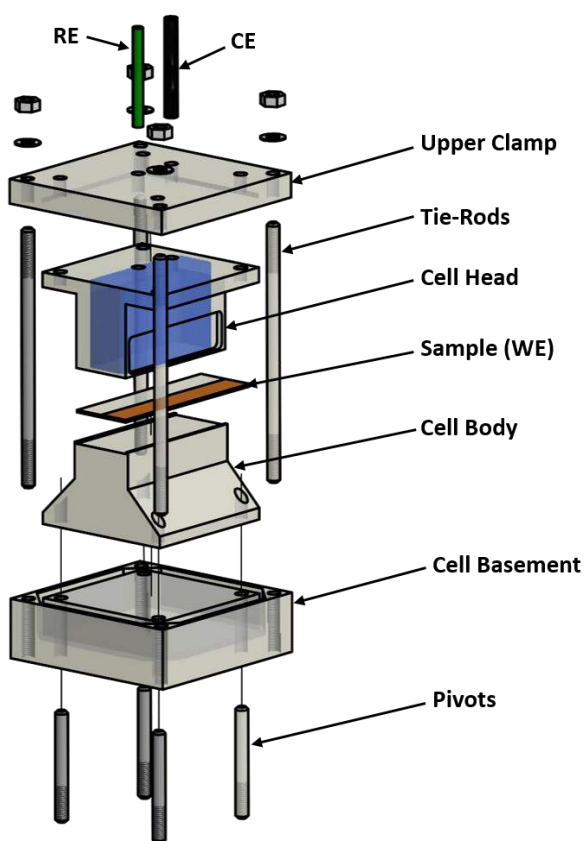


Figure 39 – An exploded view depicting the parts that compose the cell

In this configuration, the electrochemical cell is created by the sample surface (bottom) and by the cell head (which is basically a reversed basin). The sealing of the cell towards electrolyte spilling was granted by the high level of flatness of both the sample surface and the machined bottom side of the head. The tank was designed to hold approximately 10 cm^3 of the electrolytic solution. The chosen geometry permitted the use of the GIXAS technique using the geometry visible in **Figure 40** & **Figure 41**. Following criteria 1), 2) & 3); an extended portion of the sample surface is placed in contact with the solution along the x-axis, and a wall thinning on the detector side permits to minimize the dampening of the output fluorescence intensity. In agreement with criteria 4), the electrical contact was granted by the continuous metallic film which exits in the back of the cell. In the end,

following criteria 5), the electroactive surface was diminished by templating the metallic film during its preparation.

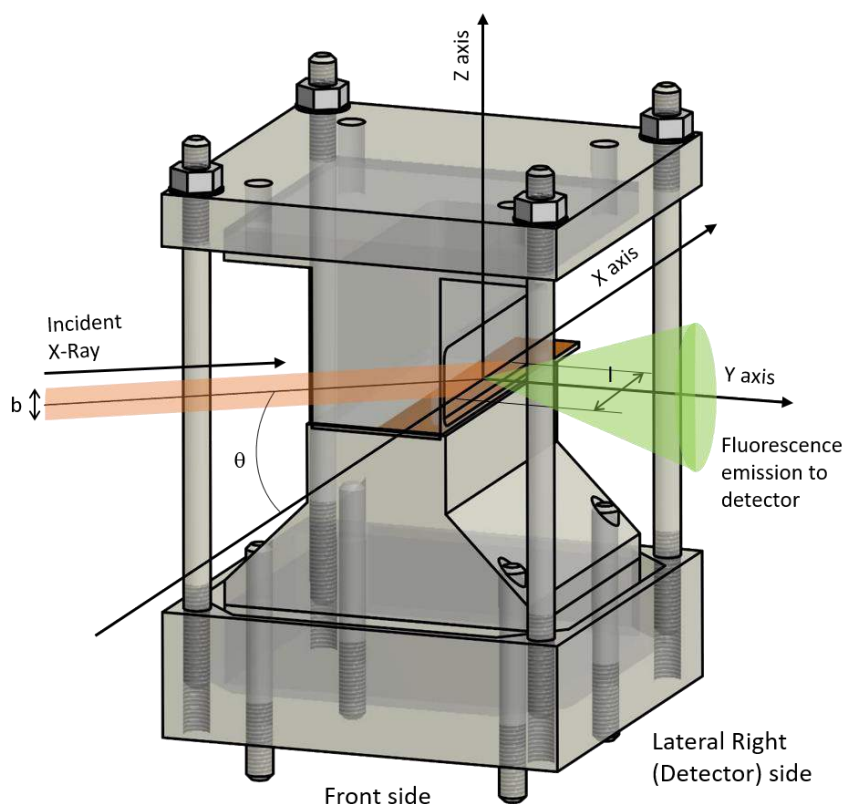


Figure 40 – A schematic of the GIXAS technique applied to the cell

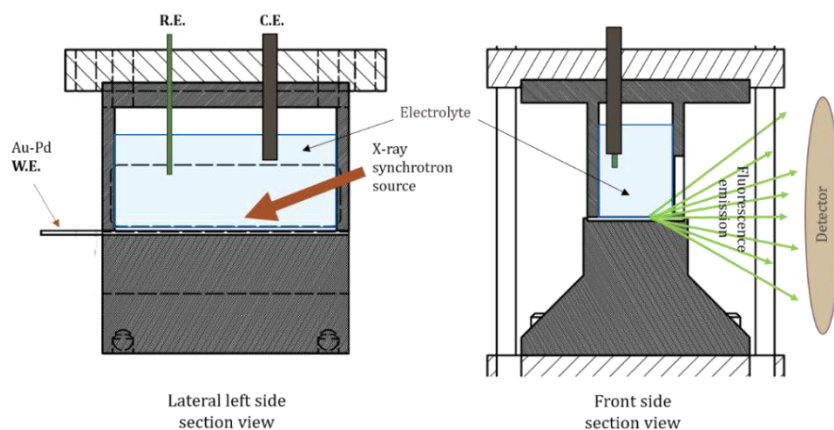


Figure 41 – Two more views to permit a better understanding of the GI-FEXRAV experiment

The sputtered surface permits the ideal division of the cell in two sides (as in **Figure 42**):

- A left side in which only the counter and reference electrode are placed;
- A right side devoted to the XAS measurements.

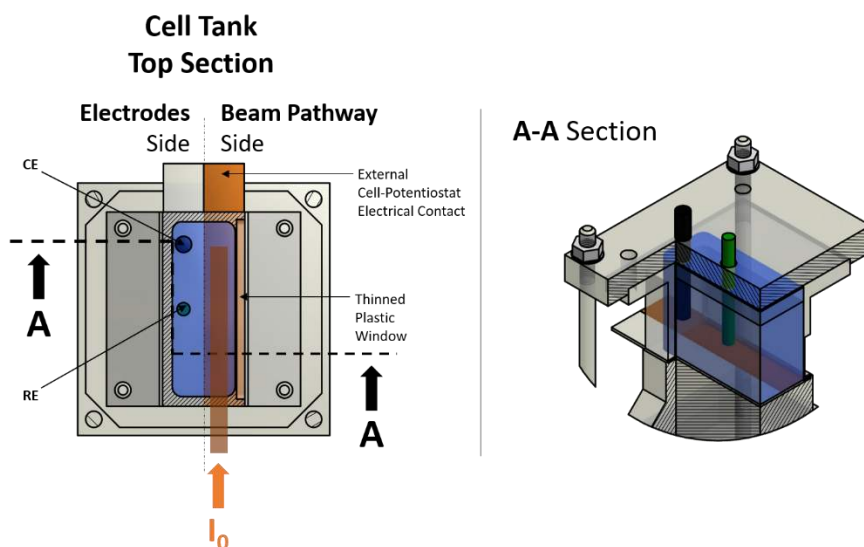


Figure 42 – Cell sections to show electrodes placement

The whole cell was made using PMMA and was machined at the INFN workshop of Sesto Fiorentino. The cell and cell components schematics can be found in *Appendix B: FEXRAV/GIXAS Cell Schematics*.

3.3.2.1 *GI-FEXRAV Cell Preparation*

The following procedure, schematized in **Figure 43**, was used to mount the cell:

- a) Tie-rods are screwed to the cell basement;
- b) Pivots are then inserted in the inner holes of the cell basement;
- c) Cell body is centred on the basement using the pivots;
- d) The working electrode (coated glass slide) is asymmetrically placed in the guide carved in the upper part of the cell body;
- e) The cell head (constituted primarily by an upside down basin) is gently lean directly on the surface of the electrode;

- f) The upper clamp is centred by the tie-rods, and placed directly on the cell head;
- g) Pivots are removed from the basement, and screwed to the GIXAS motor;
- h) The cell is then filled with the chosen electrolyte, the counter and working electrodes are inserted into the topmost holes;
- i) Once prepared, the cell is finally mounted into the experimental chamber thanks to the previously fixed pivots.

The catalyst deposit was performed directly in cell after its assembly, using the procedures in **3.3.3**.

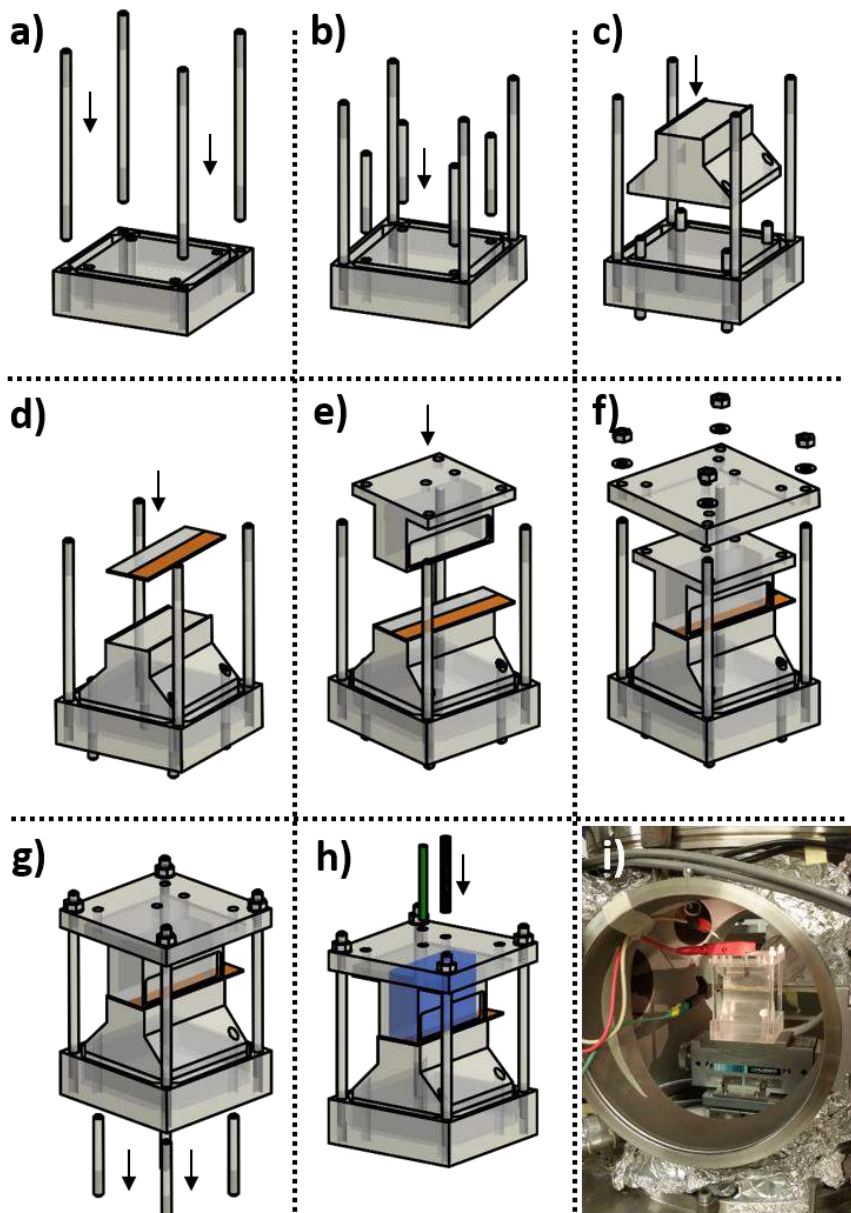


Figure 43 – The various steps needed to prepare the cell

3.3.3 Catalytical Model Surfaces preparation

In order to perform the GI-FEXRAV experiment, Pd model surfaces, with an electrochemical behaviour similar to the Pd nanoparticles, had to be prepared. UPD demonstrates as an optimal technique to obtain such monolayered structures but, in order to perform these depositions, a particularly ordered surface has to be used. Usually, UPD is performed on monocrystalline Au⁴⁴ or Ag^{6–8,10} surfaces with a specific crystallographic orientation, and a small geometrical area. On the contrary, in our experiment, a broad surface was required; such a monocrystalline surface would be either impossible to prepare in our laboratory or too much expensive to buy. To bypass these practical issues, the decision to test the UPD on polycrystalline surfaces was taken.

This idea arises from the lecture of a vast number of publications^{45–49} in which glass slides covered by thin layers of different metals were used as working electrodes. Particularly gold surfaces, with their tendency to rearrange by the (111) crystallographic pattern, showed promising for our purposes. Again, a wide array of publications regarding UPD on these Au surfaces was present, some of these referring to methods to obtain palladium mono or submonolayers exploiting UPD^{50–52}. Direct Pd UPD deposition is possible in principle, but it leads to the formation of about two Pd monolayers on a monocrystalline Au (111) electrode⁵³.

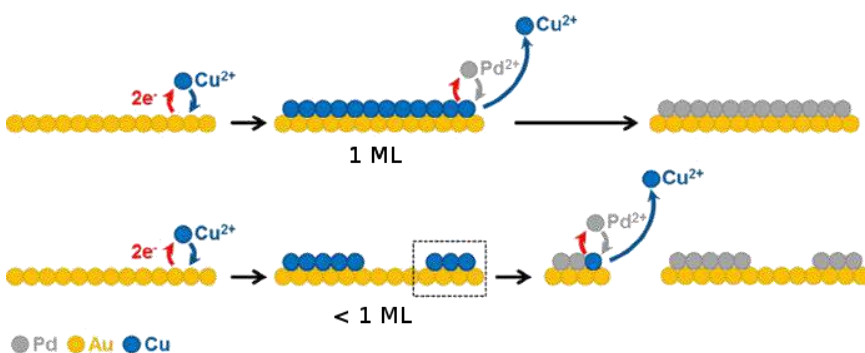


Figure 44 – Scheme of the deposition processes: a) UPD of Cu on the polycrystalline Au (111) surface, (B) SLRR between Cu and Pd, (C) the final Pd surface

In order to achieve a smaller palladium loading, another procedure was chosen, based on:

- 1) The deposition of a sacrificial metal;

2) Its subsequent substitution with Pd using Surface Limited Redox Replacement (SLRR)

Copper was chosen for point 1), due to its dual UPD phenomenon, which permits different surface coverages, a 0.6 monolayers coverage and a 1 monolayer coverage above Au (111), and thus an increased flexibility on the extent of palladium coverage.

A scheme of the procedure used is shown in **Figure 44**, while in the following chapters, a detailed description of the work done to obtain and characterize these Pd/Au surfaces is shown.

The whole chapter **3.3.3** can be schematized as follows:

- Preparation of metallic conductive surfaces by magnetron sputtering methods and thermal treatments;
- AFM characterization of the obtained surfaces;
- Cu UPD tests on the surfaces;
- SLRR between Pd and Cu;
- Alcohols oxidation tests;
- XPS characterization of the Pd/Au surfaces.

3.3.3.1 Chemicals

In **Figure 45** the solutions used for the catalytical surface preparation and testing are shown:

| Use | Solution | Chemical | Product, purity, dealer |
|--------------------------------|---|--------------------------------|---------------------------------------|
| <u>Cu UPD solution</u> | H ₂ SO ₄ 0,1M + CuSO ₄ 1mM | H ₂ SO ₄ | AnalaR Normapur, 95%, WWR Chemicals |
| | | CuSO ₄ | Analytical grade, 65%, Carlo Erba |
| <u>Pd SLRR solution</u> | HClO ₄ 0,1M + PdCl ₂ 0,1 mM | HClO ₄ | Analytical grade, 65%, Carlo Erba |
| | | PdCl ₂ | Cabro S.P.A. |
| <u>Ethanol oxidation tests</u> | NaOH | NaOH | >98%, Fluka |
| | NaOH + EtOH | | |
| | | EtOH | AnalaR Normapur, 99,9%, WWR Chemicals |

Figure 45 – List of the used reagents, together with the prepared solutions

3.3.3.2 Substrate Preparation

Polycrystalline Gold (111) surfaces were prepared using sputtering methods commonly employed to metallize object for Scanning Electron Microscopy (SEM) analysis. Microscope slides were used as base inert support for the deposition of the metals, due to their certified and continuous flatness (within .00011" per inch). Prior to deposition, glass surfaces were cleaned by:

- 1) A 10 minutes sonication cycle in Acetone (technical);
- 2) Rinsing using milli-q water ($R = 18.0 \text{ M}\Omega \cdot \text{cm}^{-1}$);
- 3) A 10 minutes sonication cycle in EtOH (100%, reagent grade);
- 4) Rinsing using milli-q water;
- 5) Drying by a nitrogen flux.

Two magnetron sputtering machines, EMITECH K575X Turbo Sputter Coater and EMITECH K550X Sputter Coater, located at the CE.M.E. facility of the Florentine CNR institute, were used to obtain first a 150 nm thick tantalum deposit as bond coat and then 70 nm thick gold surface deposit (**Figure 46**) on the surfaces of the glass slides.

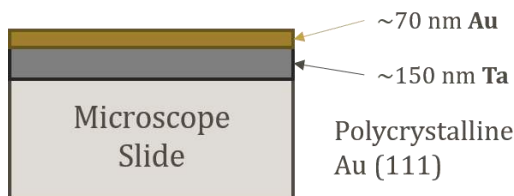


Figure 46 – A section of the obtained Au/Ta surface

The parameters used to obtain the deposits are the following:

- **Ta** deposit: 8 minutes sputtering at 100mA (10-3bar chamber pressure)
- **Au** deposits: 8 minutes sputtering at 50mA (10-2bar chamber pressure)

Metallic layer thicknesses were calculated by using deposit weights and considering a homogeneous growth of the films only on one of the main

surfaces of the glass substrate. Various deposition tests, performed also varying the position of the glass slide with respect to the coater rotating slit, were performed in order to assess the weight variability of the substrates, but no significant deposit change has been noticed both for the Au and the Ta. The specified thicknesses were needed to obtain metallic surfaces with a low ohmic drop.

The gold substrates were then heat treated using both flame annealing and oven annealing in order to define, by AFM and electrochemical methods, changes in their surface. Four different treatments were tested on the sample surfaces:

- a. No thermal treatment (crude surfaces);
- b. Flame annealing;
- c. Oven annealing (3 hours);
- d. Oven annealing (6 hours).

Flame annealing was performed using a mini-blowtorch, placing the prepared glass on a thick (4mm) copper plate (in order to disperse the heat), and by slow rastering of the surface using the blue tip of the butane flame. Between each rastering cycle, the surface was let to cool down for about 30 seconds. During this treatment the surface passes from a pure gold colour to a pink reflex, and then again, to a pure (yet darker) gold colour; the heat treatment was stopped after this last transition (about 10 rastering cycles).

Oven annealing was performed inserting the samples in an oven at room temperature, increasing T till 500°C, waiting a different amount of time (3 to 6 hours) and then turning off the oven. The presence of the samples inside the oven for both the heating and the cooling cycles was necessary in order to minimize thermal stress in the glass slide, and thus to avoid its breaking. A slow nitrogen flow was maintained inside the oven chamber during the heat treatment in order to minimize possible oxygen interaction with the as-prepared surface.

3.3.3.3 *Substrate Analysis*

After the various annealing processes, the first series of considerations was performed by observing the samples. The various treatments led to different macroscopic surface finishings, visible by naked eye. Flame annealed samples, as already specified, tended to acquire a darker gold colour with

respect to the untreated samples, while in both the oven annealed sample series the presence of surface spot defects was visible. Notably, on the 3 hours annealed sample surfaces, few millimetric creases appeared, while for the 6 hours annealed samples smaller but numerous ridges were often seen (**Figure 47**). Cohesion tests performed mounting and unmounting the obtained substrates in the cell also showed a more significant probability of exfoliation of part of the gold layer above the tantalum for both the oven annealed samples in respect to the un-annealed and flame annealed ones.

This tendency was probably attributable to the different thermal expansion coefficients of the materials constituting the electrode. Just considering the linear expansion coefficients, we can notice values of about $8.5 \cdot 10^{-6} \text{ k}^{-1}$ for ordinary glass, $6.5 \cdot 10^{-6} \text{ k}^{-1}$ for tantalum and $14.2 \cdot 10^{-6} \text{ k}^{-1}$ for gold. This means that, during heating, the topmost and bottommost layers tend to elongate more in respect to the middle tantalum layer. Particularly gold, which has an expansion coefficient doubled in regard to the tantalum, expands more with respect to the substrate, inducing stresses in the layer interface, and then producing detachment between the two metallic layers.





| Sample | Top sample view | Notes |
|-----------------------------------|---|---|
| <i>No annealing (as prepared)</i> |  | Homogeneous sample |
| <i>Flame annealing</i> |  | Darker center colour, gets darker on the border |
| <i>Oven annealing (500°C, 3h)</i> |  | Crease presence (few but big) |
| <i>Oven annealing (500°C, 6h)</i> |  | Crease presence (more but small) |

Figure 47 – Macroscopic changes on the sample surfaces after the annealing processes

Finally, an AFM investigation was performed to assess changes in the topography of the samples after the annealing treatment. Measures on the prepared surfaces were performed using the Pico Scan Molecular Imaging AFM present in our laboratory, used in contact mode with force set point of 0.1V. The used tip was an NP-10 Veeco, a nonconductive silicon nitride triangular tip with a k of 0.12 N/m. Images were acquired with a frame of

512x512 points, with a scan speed of 1.2 lines/second. The first acquisitions were made on the no annealing samples, to define topological changes in between the various zones due to the sputtering process. A set of different series of images on three different substrates (prepared at different times with the same methodology) was performed, but no change in topological data between the samples centre and various sample spots was seen. A new series of sample acquisitions was then performed on the heat-treated samples. Images shown in **Figure 48** are referred to central sample points, in the crease-free zones for the oven annealed surfaces.

By looking the images, an evident change in topography can be assessed:

- a. **No Annealing Samples** acquisitions show the presence of a bumpy surface, with spherical features of less than 0.1 μm horizontal dimensions.
- b. In **Flame annealed samples** similar features are visible. Their dimensions seem to be a little smaller with respect to sample (a.); also some deeper spots between the particles are visible;
- c. In the **Oven Annealed (3h) samples**, a precise reconstruction of the surface was appreciable. Gold seems to be agglomerated, showing a peculiar “brainy” pattern with more prominent valleys between the heights;
- d. Again, in the **Oven Annealed (6h) samples** a similar topography in respect of samples (c.) can be seen. This time the overall structure seems more compact, with the formation of surface scales.

From the obtained images, roughness data was extrapolated using the Gwyddion software package. A set of four line acquisitions was taken from the central point of the variously annealed samples. This process was repeated for two samples for each annealing procedure. In **Figure 49**, an esteem of the average roughnesses, together with the maximum deviation from the average, can be found.

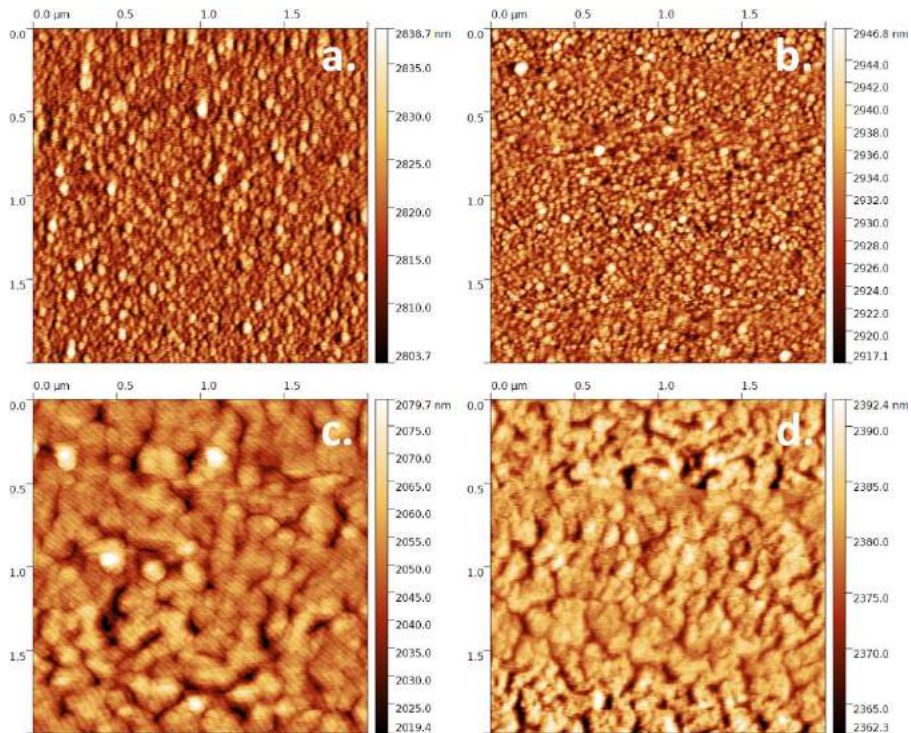


Figure 48 – AFM images of a) No annealing sample, b) Flame annealed sample, c) 3h Oven Annealed Sample, d) 6h Oven Annealed Sample

| | No annealing | Flame Annealing | Oven Annealing (3h) | Oven Annealing (6h) |
|---------------|---------------|-----------------|---------------------|---------------------|
| R_a [nm] | $3,7 \pm 0,5$ | $2,9 \pm 0,2$ | $2,6 \pm 0,7$ | $2,4 \pm 0,3$ |
| R_q [nm] | $4,9 \pm 0,3$ | $3,6 \pm 0,3$ | $3,3 \pm 1$ | $3,0 \pm 0,4$ |
| R_t [nm] | 30 ± 2 | 20 ± 2 | 22 ± 8 | 17 ± 1 |
| R_{tm} [nm] | 23 ± 2 | 16 ± 2 | 15 ± 4 | $12,7 \pm 0,6$ |

Figure 49 – Roughness parameters obtained from the AFM images

The reported roughness parameters are:

- R_a (Arithmetical mean deviation of the roughness profile);
- R_q (Root mean square deviation of the roughness profile);

- R_t (Total height of the roughness profile);
- R_{tm} (Total height average of the roughness profile).

3.3.3.4 UPD of Cu on Polycrystalline Au (111)

The quality of the surfaces was first tested in respect of the underpotential deposition of copper. Cu UPD above monocrystalline Au (111) is an extensively studied phenomenon^{54–57}; the comparison between voltammetries executed on monocrystalline Au (111) surfaces and on our iso-oriented polycrystalline Au (111) surfaces helped to define the feasibility towards the UPD phenomenon. On a clean monocrystalline Au (111) surface, voltammetries performed using H_2SO_4 0.05M + $CuSO_4$ 1 mM electrolyte show the presence of two distinct UPD peaks at potentials that precedes the bulk deposition potential of copper (**Figure 50**, potentials are related to the Ag/AgCl KCl sat. electrode).

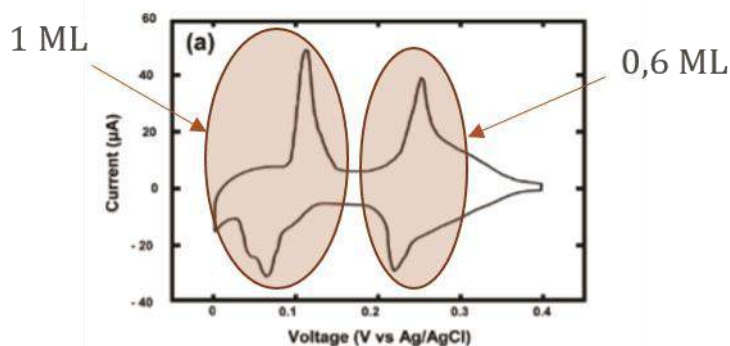


Figure 2. (a) Steady-state cyclic voltammogram for Cu UPD on Au-(111) in 0.05 M H_2SO_4 and 1 mM $CuSO_4$ solution. Potential sweep rate: 5 mV/s. (b) EC-STM image of the honeycomb $(\sqrt{3} \times \sqrt{3})R30^\circ$ structure obtained at +0.15 V. Bias voltage: -150 mV. Tunneling current: 20 nA.

Figure 50 – Cu UPD phenomenon on monocrystalline Au (111)

The first cathodic peak at a potential of 0.22V is related to the electrodeposition of 0.6 ML of copper above the Au surface, with a $(\sqrt{3} \times \sqrt{3})R30^\circ$ structure, while the peak at potential 0.08 V can be attributed to the 1 ML Cu deposition. At potentials below 0 V the bulk copper deposition occurs. Same voltammetric tests were performed on the prepared substrates, as described also in Vincenzo Dell'Aquila's bachelor thesis⁵⁸. The Au-Ta surfaces were mounted in the cell and used as working electrodes, adopting the same 0.05M H_2SO_4 + 1m $MCuSO_4$ electrolyte cited

in literature. The EC cell was completed by an Ag/AgCl KCl sat. reference electrode, and a graphite rod electrode as counter electrode. Cyclic voltammetries were acquired by linearly varying potential between 0.45V and -0.60V, using a scan speed of 50 mV/sec. The in-cell exposed working electrode surface had a rectangular shape, with dimensions of 54 mm x 8 mm. In **Figure 51** a review of the performed cyclic voltammetries can be seen.

As also described by Dell'Aquila, a series of voltammetric tests were performed on different substrates prepared using the same heat treatment, to define the reproducibility of the substrate preparation. As shown in **Figure 52** little changes in the voltammetric behaviour toward Cu UPD were noticed between the samples treated by the same annealing process, while a substantial difference was seen in between the heat treatment series.

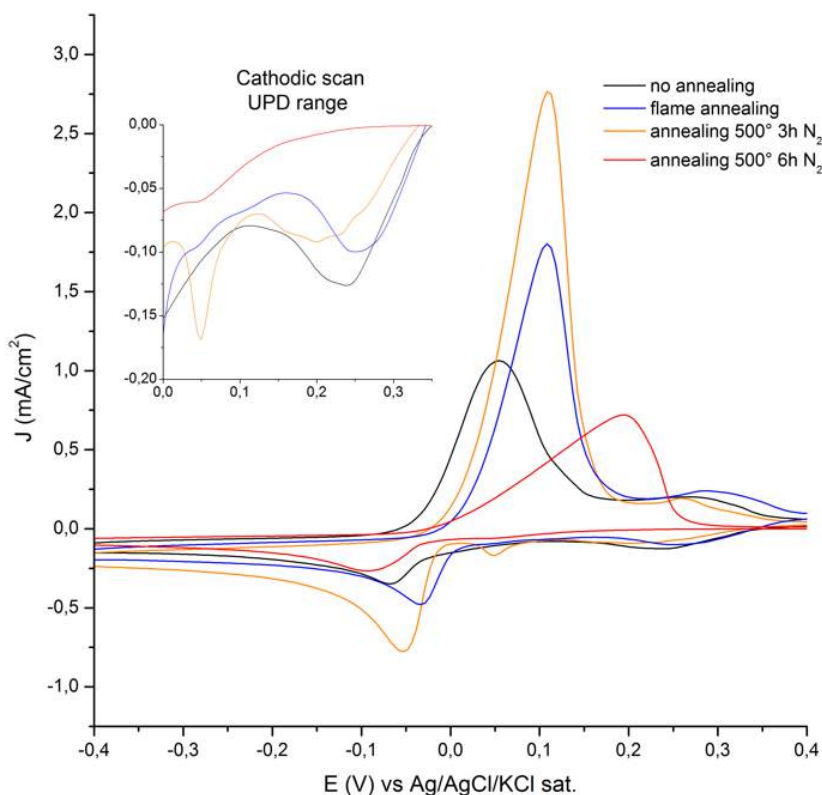


Figure 51 – CVs performed in the H₂SO₄ 0.1M + CuSO₄ 0.1 mM solution using the different substrates prepared

A comparison between the reference voltammetry on Au (111) (**Figure 50**) and our tests performed on the heat treated surfaces (**Figure 51**) was then performed. From the inset graph of **Figure 51**, a peak related to the 0,6 ML deposition (0.22V) can be seen for all the heat-treated samples, while the 1 ML peak (0.08V) is clearly visible only for the oven annealed substrates, just before the bulk deposition peak. In order to prepare the samples for the subsequent Surface Limited Redox Replacement process, we decided then to obtain a 0,6ML UPD deposition of copper. Cu depositions were then performed by potentiostatic deposition, applying a potential of 0.22V for 5 minutes using the abovementioned sulfuric acid + copper sulphide solution.

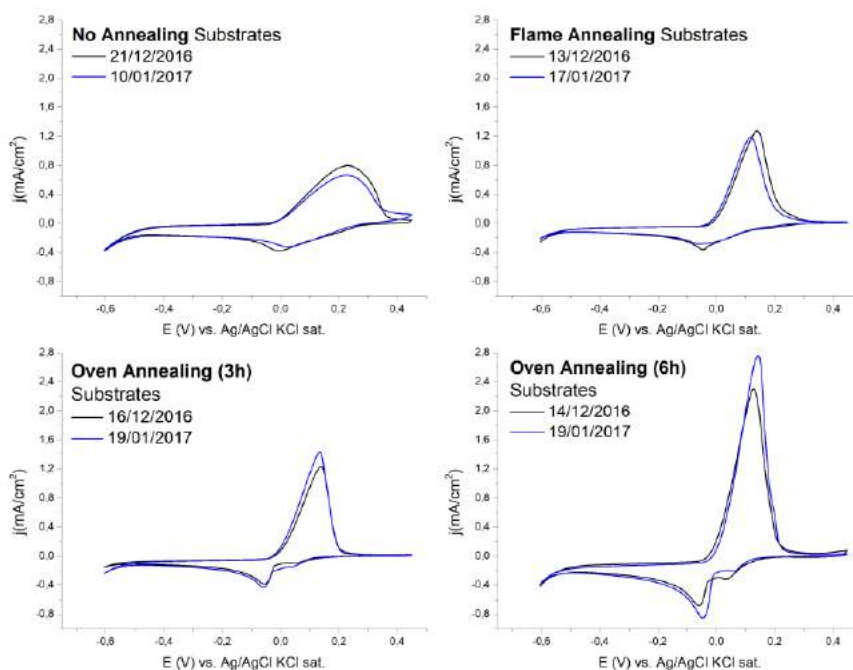


Figure 52 – Reproducibility tests of the electrochemical behaviour of the surfaces toward Cu deposition – H_2SO_4 0.05M + CuSO_4 1mM electrolyte, CVs from 0.45V to -0.60V, scan speed 50 mV/sec

3.3.3.5 SLRR of Pd from Cu & Alcohol Oxidation Tests

Once performed the Cu UPD deposition, we proceeded with the Surface Limited Redox Replacement by merely turning off the potentiostat, rinsing the cell with deionized water, and then adding a PdCl_2 0.1mM + HClO_4 0.1M solution, as specified in literature⁵⁹. The solution was left in the cell for about 10 minutes to permit a complete exchange between Cu adatoms and Pd

ions. The cell tank was finally emptied and rinsed again with deionized water, prior to the introduction of the catalytic test solutions.

3.3.3.6 Ethanol oxidation tests

Various catalytical tests were performed on the as-obtained surfaces using different alcohols (Methanol, Ethanol, Ethylenglycol, and Glycerol) in alkaline KOH solutions in a concentration between 0.1M and 2M. Results of these tests were presented elsewhere⁵⁸. These investigations were performed primarily to define if an effective Cu-Pd substitution had occurred on the electrode surface and to assess the best catalytical activity between the annealed substrates.

Focusing on the substrates reactivity toward ethanol electrooxidation, in Figure 53 the CVs performed on heat treated surfaces, using the alkaline fuel electrolyte prior and after the Pd deposition process, showed an evident change in the electrochemical behaviour of the surfaces (**Figure 53**), with the comparison (after the Cu UPD and the Pd SLRR) of the typical palladium curve for the ethanol oxidation.

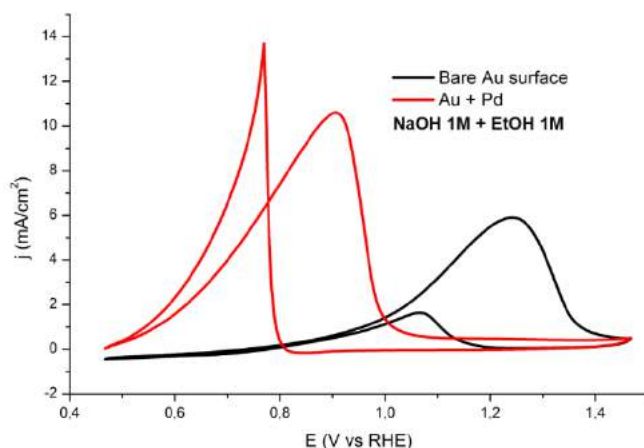


Figure 53 – CVs in a NaOH 1M + EtOH 1M solution using as WE the bare flame annealed surface (black) and the Pd 0.6 ML on Au flame annealed surface (red), scan speed 50 mV/sec

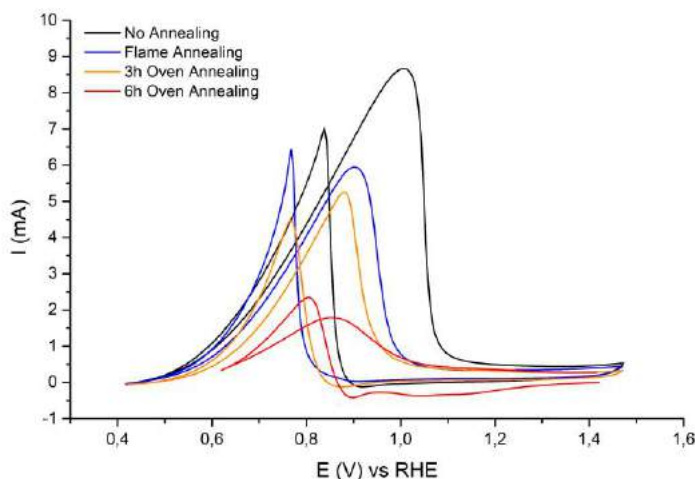


Figure 54 – Comparison of voltammetries on 0.6 ML Pd surfaces towards ethanol oxidation (NaOH 2M + EtOH 2M electrolyte) for different substrate heat treatments; CE graphite rod, RE Ag/AgCl KCl sat., scan speed 20 mV/s

A comparison between the various flame annealed samples was also performed; in **Figure 54** the voltammetries related to the differently annealed substrates, using NaOH 2M + EtOH 2M as an electrolyte, are shown.

From the chosen series, the “no annealing” sample seems to be the one with the higher oxidation current, followed by the flame annealed one, the 3h oven annealed one, and finally, the 6h oven annealed one. The increase in current and the broader potential window in which both oxidation phenomena occur (the one during the anodic scan and the one during the cathodic scan) can be attributed to a higher catalyst loading on the palladium surface.

3.3.3.7 *Comparison between the electrochemical behaviour of UPD Pd and Pd NPs towards ethanol oxidation*

A comparison between the ethanol oxidation voltammetries obtained in EtOH + NaOH solution, between Pd NPs catalyst and 0.6 ML coverage Pd thin film catalyst (on a flame annealed gold surface) is shown in **Figure 55**. Voltammetries were performed with the same electrochemical set-up adopted in the previous chapters, using a scanning speed of 1 mV/sec.

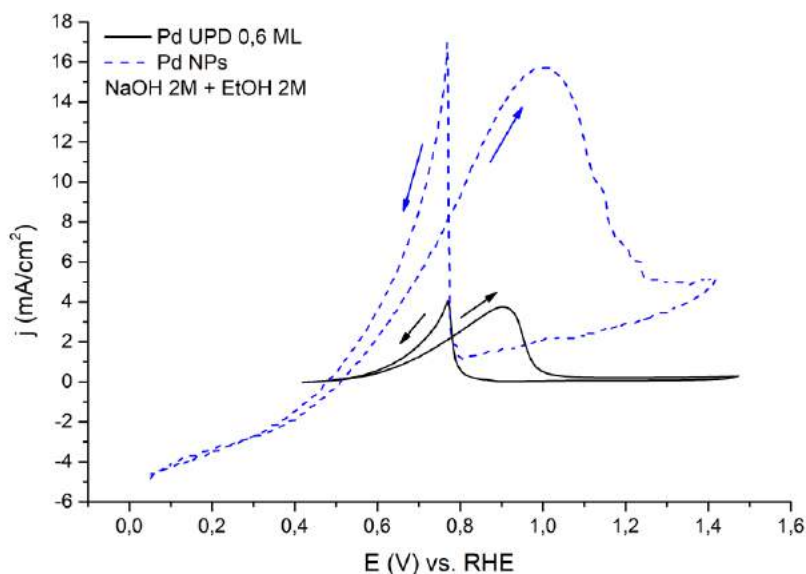


Figure 55 – EC comparison of the ethanol oxidation phenomenon between a thin film surface (black) and the Pd NPs deposition used for the previous FEXRAV experiment, 1mV/sec.

The area used to obtain current densities was calculated with the following assumptions:

- The Pd film electrodic area has been estimated by considering the exposed geometrical area of the electrode (54 mm x 8 mm), and by multiplying this value by the ML coverage of Pd (0.6);
- The Pd nanoparticles total electrodic area has been calculated starting by the load in the powder (4 mg/cm²), by considering an average particle radius of 2.5 nm, and a palladium density equal to the one shown by the bulk (12,023 g/cm³).

This comparison has then to be considered a rough esteem of the effective activity of the samples towards alcohol electrooxidation. Despite the current, it was mainly interesting to notice a similar electrochemical behaviour for the two samples, with a lower ohmic drop (slope) related to the thin layered samples. The electrochemical behaviour of the films, together with the high degree of reproducibility of the production process,

permitted to adopt the obtained catalytical surfaces as model surfaces for the study of Pd deactivation.

3.3.3.8 XPS surface characterization

XPS studies were performed on the catalytically active surfaces to assess the presence of copper after the redox replacement, and to give an esteem of the Pd coverage above the surface after the galvanic exchange.

The chemical surface composition of the samples was studied using a custom built XPS. The sample was kept in an ultra-high vacuum (UHV) chamber and targeted by a non-monochromatic X-ray source (VSW-TA10 Mg K α radiation, 1253.6 eV), with an operative power of 100 W (10kV, 10mA). A VSW-HA100 hemispherical analyser mounting a 16 channel detector and operating in fixed pass energy mode (22eV) was used. Data analysis was performed removing the inelastic background by Shirley's method⁶⁰, the spectra were fitted using mixed Gaussian and Lorentzian line shapes for each component, and imposing an equal FWHM for all the components of the same element. The spectra were calibrated by using the 4f 7/2 transition of gold at 84.0 eV, as internal reference⁶¹.

In **Figure 56** the percent coverages of Pd in respect of the Au surface found for every substrate.

| | No Annealing | Flame Annealing | Oven Annealing (3h) | Oven Annealing (6h) |
|--|--------------|-----------------|---------------------|---------------------|
| <u>Pd atoms every 6 Au surface atoms</u> | 4,20 | 3,91 | 3,57 | 3,53 |
| <u>Pd ML above Au surface</u> | 0,70 | 0,65 | 0,60 | 0,59 |

Figure 56 – Results of the XAS investigation

In some three hours oven annealed samples (2 samples on 3 tested) and in one (over 3 tested) of the six hours oven annealed samples, a signal related to copper was also visible. This was probably due to the formation of copper islands (or due to crevice entrapment of the Cu deposit) during the UPD process, and the subsequent palladium substitution only on their surface. On the contrary, copper was not found in all the analysed “no annealing” and “flame annealed” samples.

3.3.3.9 *Final Considerations on prepared sample surfaces*

The various tests performed on the Pd/Au surfaces confirmed the production feasibility of thin submonolayers of catalytically active deposits, usable during the GI-FEXRAV experiment. However, in order to conduct the test, a surface heat treatment had to be chosen. The various features of the different heat treated surfaces were then compared, as reported in **Figure 57**. A brief description of the results of the comparison follows:

- **Macroscopic homogeneity:** *No annealing* samples and *flame annealed* samples showed the best degree of surface macroscopic uniformity in between the samples; the presence of creases (inhomogeneities) on the surfaces of both the oven annealed samples discouraged their use for the GI-FEXRAV experiment;
- **Gold Layer Adhesion:** Detachment between the gold topmost layer and the tantalum bond coat often occurred during the assembling of the cell (step e. in the GI-FEXRAV cell preparation chapter) using both the oven annealed samples, while it happened sporadically on the no annealed samples. No detachment was seen during operative conditions for the flame annealed samples.
- **Surface Roughness:** Lower roughness values were seen for the 6 hours oven annealed sample, followed by the 3 hours oven annealed one, by the flame annealed and finally by the no annealed ones.
- **Cu UPD Peaks:** For the no annealing samples, during the electrochemical tests performed with respect to the UPD of Cu, the 0.6 ML was clearly visible, while the 1.0 ML was masked by a peak probably related to the bulk deposition. The 1 ML peak was evident from all the other heat treated substrates, while the 0.6ML coverage peak was only visible for the flame annealed and the 3 hours oven annealed sample.
- **Pd Coverage and Cu presence after SLRR:** after the deposition of approx. 0.6 ML of Cu, and its substitution with Pd, XPS measurements showed a net decrease of the rough Pd coverage from the least annealed surface (no annealing, 70% coverage) to the most annealed one (6 hours oven annealed, 59% coverage). Copper-related signals were also visible in both the “oven annealed”

samples, probably due to the formation of copper 3d islands, rather than 2d layers, during the deposition phenomenon.

- **Activity towards Ethanol Electrooxidation:** All the tested substrates showed a similar voltammetric behaviour with respect to the ethanol electrooxidation, with forward and reverse scan peaks due to the deactivation and reactivation of the Pd layer. Difference between the voltammetries was seen in the maximum current density and in the peak area, indicative of the catalytical surface available. No bimetallic Au/Pd effect was seen, as compared to⁶².

All these considerations led to the use of the flame annealed surfaces as base surfaces for the experiment. The flame annealed samples showed, in fact, an excellent catalytical activity in between the series, a quite homogeneous macroscopic and microscopic surface, with the smallest variation in roughness between the analysed AFM acquisitions, and an excellent adhesion of the Au substrate to the tantalum bond coat and finally a clear 0.6 ML peak respect to the Cu deposition. Another advantage was related to their quick preparation; un-annealed samples were flame annealed directly prior their usage, via a 10 minutes procedure.

| Features\Samples | No annealing | Flame Annealing | 3h Oven Annealing | 6h Oven Annealing |
|--|--------------|-----------------|-------------------|-------------------|
| <i>Au layer macroscopic homogeneity</i> | A | A | B | C |
| <i>Au layer adhesion</i> | B | A | C | D |
| <i>Surface roughness</i> | D | C | B | A |
| <i>Cu 0,6 ML peak</i> | A | B | C | / |
| <i>Cu 1,0 ML peak</i> | / | C | B | A |
| <i>Approx. Pd surficial coverage (after Cu 0,6ML substitution)</i> | 0,7 | 0,65 | 0,6 | 0,59 |
| <i>XPS Cu signal after Pd SLRR</i> | No | No | Yes | Yes |
| <i>Activity towards ethanol oxidation</i> | A | B | C | D |

Figure 57 – A summary of the properties of the various tested thermal annealed samples; for each feature, a ranking was evidenced using a letter range, from A (representing the best result in respect of the feature) to D (the worst result)

3.3.4 Acquired Data

3.3.4.1 Ex Situ Experiment

In order to assess the technical feasibility to detect a small amount of Pd on our prepared substrates, a first XAS test was performed on a gold/tantalum glass covered by 0.6 ML of palladium deposit. For this experiment, the slide was placed directly in the cell basement, without the cell head (solution tank) as in **Figure 58**.

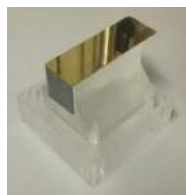


Figure 58 – The cell set-up used for the Ex-Situ experiment

The whole assembly was then mounted in the experimental chamber, and a GIXAS measure ($\theta = 0.4^\circ$, beam height $b = 200\mu\text{m}$, beam width $w = 4\text{mm}$) in fluorescence mode was acquired, varying the incident energy from 24100 eV to 25200 eV, across the K edge of Pd. The XANES region of the obtained spectra was then compared with the ones acquired using Pd and a PdO standards as targets (**Figure 59**).

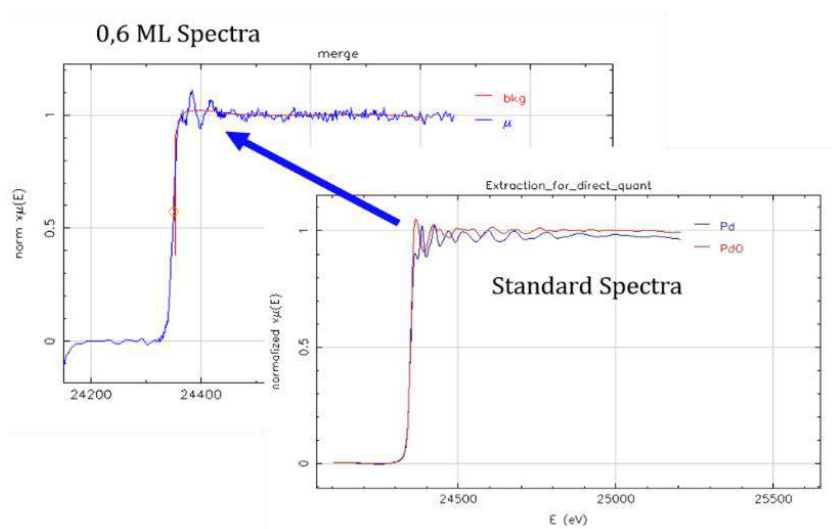


Figure 59 – Comparison of the 0.6 Pd monolayers XANES spectra (upper left) and the two standard spectra (lower right)

The comparison showed a definite resemblance between the near edge fingerprint of our sample and the one of the metallic palladium standard, thus confirming the presence of Pd⁽⁰⁾ above the slides. These Spectra were treated using the Athena software, designed explicitly for XAS spectra analysis.

3.3.4.2 *In Situ Experiments*

The same 0.6 ML Pd sample was also used to test the GI-FEXRAV technique. The cell was filled using a NaOH 2M solution, an Ag/AgCl KCl sat. electrode was used as RE, while a graphite rod constituted the CE. The spectroscopic parameters used for the experiment are shown in **Figure 60**.

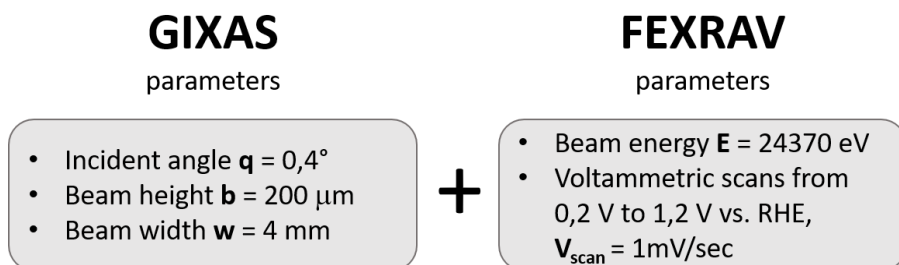


Figure 60 – The GIXAS and FEXRAV parameters used for the experiment

The horizontal sample alignment towards the beam can be seen in **Figure 61**.

For this first in situ test, during voltammetries, no absorption coefficient variation was noticeable, due to the matrix effect which led to the scattering of almost all the exiting fluorescence radiation. To minimize this effect, two different strategies could be actualized in principle:

- A change in the beam dimensions and in the sample-beam alignment:** in principle, a decrease in beam width w and a decrease in the 2 mm space between the beam and the cell wall (referring to **Figure 61**);
- A change in sample Pd loading:** an increase in the palladium content on the surface, leading to a higher fluorescence intensity.

The first solution, despite being the easiest to apply, wasn't feasible due to line pre-refurbishment status during the experiment. We decided then to repeat the test using a sample with a more significant catalytical loading.

Another substrate was then prepared, this time using a direct galvanostatic Pd deposition⁵³, producing about 10 ML of Palladium onto the Au surface.

Cell Front Section

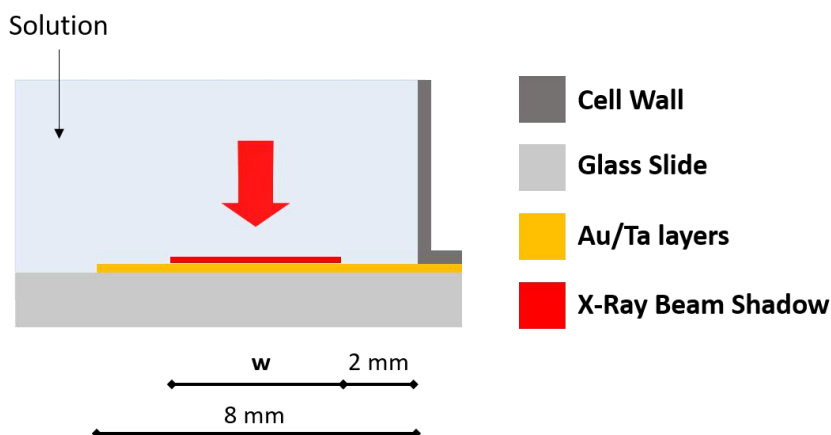


Figure 61 – Front cell section scheme depicting Sample-Beam geometrical displacement

The new acquisition is visible in **Figure 62** and **Figure 63**, it was prolonged for about 10 hours and clearly showed a similar result with respect to the measures obtained using the plain FEXRAV technique on dispersed nanoparticles. No substantial variation (decrease in current intensities) between the various CV cycles was noticed this time. Also, the comparison between the first FEXRAV cycles, in **Figure 34** and **Figure 63**, showed the presence, for the thin layer Pd deposit, of a cathodic peak at about 0.8V vs RHE, and of an anodic plateau at more positive potentials. These two features weren't visible during the previous scans performed on the dispersed system, demonstrating a higher level of the order of the model surface.

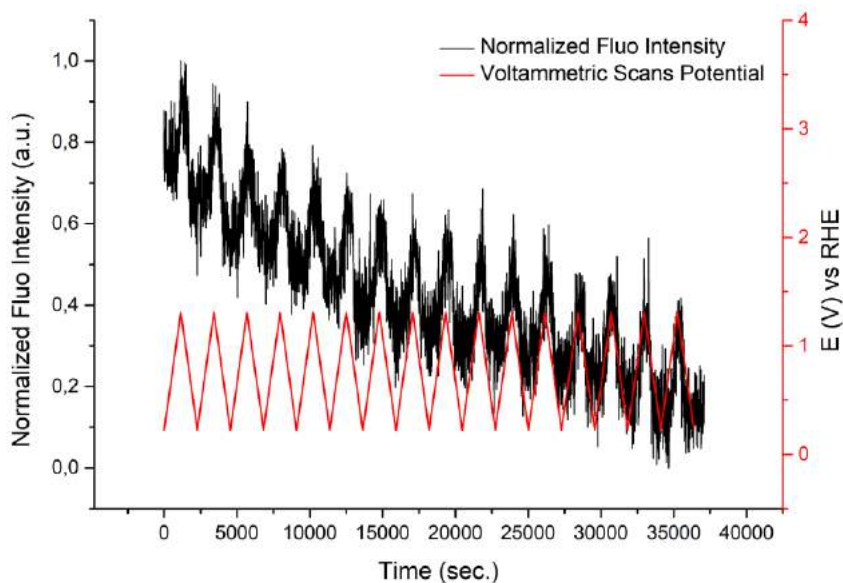


Figure 62 – GI-FEXRAV continuous acquisition of 16 CV cycles on the Pd 10 ML sample, NaOH 2M electrolyte

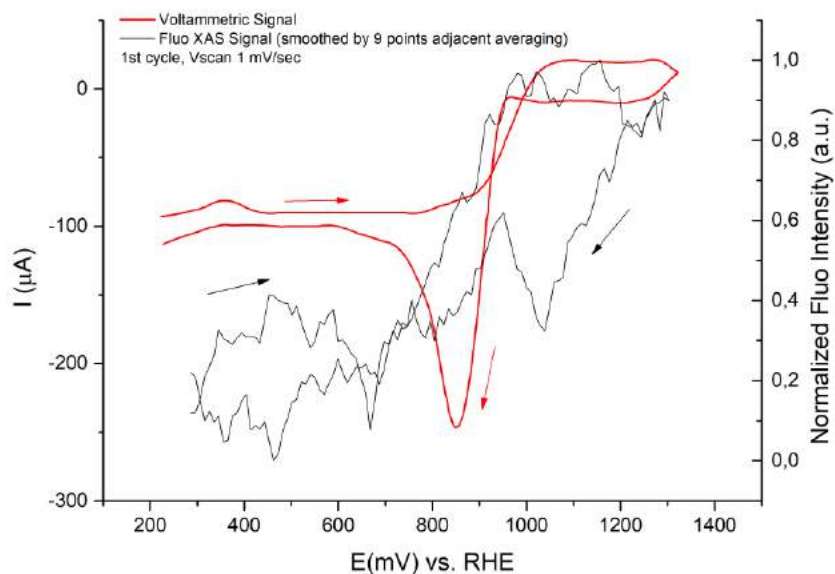


Figure 63 – Variation of fluorescent signal coupled with cyclic voltammetry for the 15th scan cycle

A final XAS acquisition was performed in fluorescence mode, after the GI-FEXRAV run, targeting the liquid phase. The purpose of this test was to acquire evidence of some Pd dissolution event that could have been occurred during the cycling of the cell, for this reason, the XAS scan was performed around the palladium edge (from 24100 eV to 25200 eV), like in the ex-situ measure. Despite the decrease in intensity of the fluorescent yield, sign that a diminishing of the Pd content on the electrode has occurred, the obtained spectra did not show the typical Pd edge jump. This lack of signal was again attributed to the low concentration of dissolved Pd ions into a big volume of solution, and to the dampening of the emission due to solution scattering.

3.3.5 Topography of the sample after the GI-FEXRAV experiment

An advantage in using model surfaces consists in the possibility to study surface modifications before and after the sample duty cycles, by means of Scanning Electron Microscopy or Atomic Force Microscopy, to define changes in surface morphology. In this chapter, the preliminary studies performed on the 10 ML Pd sample are shown. AFM acquisition was completed at the PSCM facility of the ESRF, using an MFP3D Asylum Research AFM in tapping mode. **Figure 64** collects the images acquired before every preparation step, from the no annealed surface (a.), to the annealed one (b.), passing by the surface after Pd direct deposition (c.) and finally to the surface after the GI-FEXRAV experiment (d.). While the first two images (a. & b.) did not vary significantly from the ones acquired in our lab during substrate testing, and no variation can also be seen from the bare Au surface (b.) and the same surface covered by Pd (c.), a significant change in topography was seen on the surface after the x-ray/voltammetric cycles (d.).

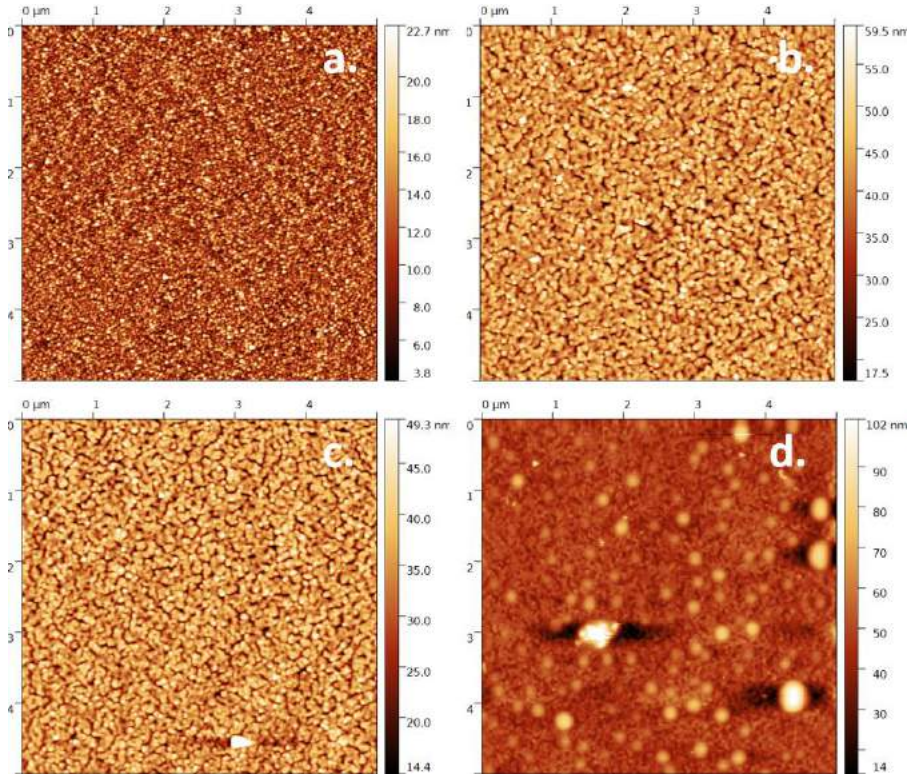


Figure 64 – Substrate surfaces: **a.** before annealing, **b.** after annealing, **c.** after the deposition of 10 MLs of Pd, **d.** after the GI-FEXRAV experiment

From these images, the appearance of spherical caps of approximately 300 - 500 nm diameter was clearly visible. This bumpy surface was present only in the x-ray beam path; on the beam free zones, the surface seemed somehow flattened in respect of the initial surface (**Figure 65**).

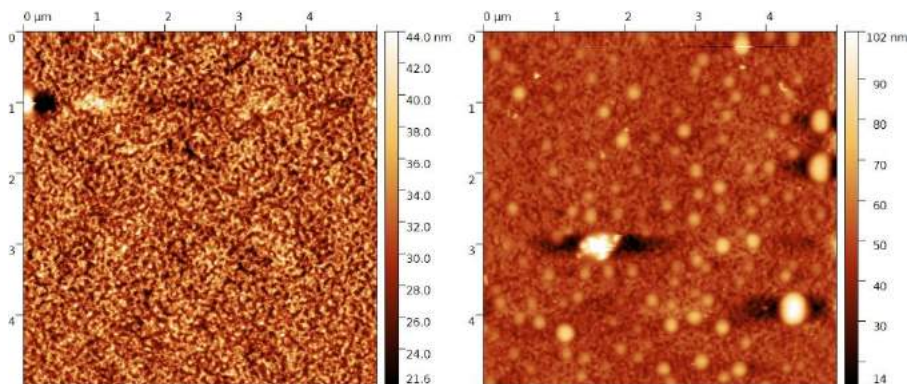


Figure 65 – The 10 ML sample after the GI-FEXRAV experiment; Surface hit by the x-ray (right) and beam-free surface (left)

These structures were probably produced to some x-ray induced ripening phenomenon. However, we were unable to perform a SEM-EDX characterization, in order to define the nature of the newly created structures.

4 Electrodeposition and characterization of aluminium metal films from Ionic Liquids (ILs)

4.1 Introduction

The work done in the framework of the European Project SCAL-UP (<http://scalup.eu>) focused on the development and on the understanding of the aluminium electrodeposition process from Ionic Liquids, in order to produce a pilot plant for the scaling up of the typical lab deposition process. The task of our unit during this research was focused on the determination of the best deposition conditions in order to obtain thin aluminium layers of technical and industrial interest. Mainly, it was focused on automotive and energy industries; various deposition attempts were performed on plastic bumper trimmers for automotive aesthetics and on turbine vanes, to produce Al thermal barriers and/or bond coats.

4.2 Ionic Liquids

The most accepted definition of Ionic Liquid is “a molten salt which is liquid at temperatures below 100°C”. Ionic liquids are in fact made by a mixture

of salts, usually by organic cations and inorganic anions, which show phase transition when mixed together. The name of this class of solvents was first addressed in the '70⁶³ when the first few mixtures of ionic liquids were used as a media for organic synthesis and/or catalysis. During the years many advancements have been made in order to tailor ionic liquids for specific purposes; The so-called 1st generation ionic liquids, based on bi-substituted Imidazole salts ($R^I R^{II} \text{Mim}^+ \text{Cl}^-$ with R^I and R^{II} as aliphatic chains, as an example) and Aluminium Chloride have been supplanted by 2nd generation ionic liquids (less moisture sensitive, due to the presence of solely organic molecules) and Deep Eutectic Solvents (DESs). In fact, research had increased enormously the number of available ionic liquids, year after year, due to the possibility of mixing a wide array of different salts to form a liquid; some esteem addressed the knowledge of more than 2000 different ionic liquids in 2016, each one with its own distinct physical and chemical characteristics. But what is the main advantage of Ionic Liquids with respect to the commonly used Water and Organic media? Apart from the difference between single ionic liquids⁶⁴, the whole class shows significant benefits in regard to the other widely used types of solvents (aqueous and organic), in fact acquiring the best properties between the two (**Figure 66**).

| | Water | Organic Solvents | Ionic Liquids |
|---------------------------------------|-----------|------------------|-------------------|
| Conductivity | Low | Low | High |
| Vapour Pressure | Mid | High | Negligible |
| Thermal Stability | High | Low | Mid |
| Flammability | No | High | No |
| Electrochemical Window | 1,23V Max | Wide | Wide |
| Catalyst for Organic Reactions | No | Yes | Yes |

Figure 66 – Comparison of the features of water-based, organic based and Ionic Liquid electrolytes.

First of all, they show excellent thermal properties; like molten salts, ILs have a negligible vapour pressure, an excellent thermal stability and no flammability. The shown durability during heating has also contributed to their fame of “green solvents”, solvents with a low environmental impact;

ideally, they can be used and purified continuously without loss and with little degradation of their constituents.

Other interesting features are related to their electrical properties; their high ionic conductivity (they are made solely by ions) and their wide electrochemical window (from 4V to 6V, depending on the used salts) contributed to increase the interest for these media also for their exploiting as inert electrolytes for lab and industrial purposes. Many studies regarding their use as electrolytes in energy storage and conversion (batteries and fuel cells) have been performed during the last two decades. For the same reason, a great effort in research has been undertaken in order to use them as electrolytes for the deposition of metals, especially for species which cannot be deposited using traditional solvents, due to deposition potentials far outside to the electrochemical stability window of water. A significant effort was mainly devoted to the research on the electrodeposition of Aluminium from 1st generation ionic liquids, a process both easy to achieve and delicate regarding the conditions in which the ionic liquids have to be kept.

One of the significant issues related to 1st generation ILs behaviour (and in general to all ionic liquids) is their moisture sensitivity. Ionic Liquids are in fact formed solely by salts, which show a certain degree of hydrophilicity if left in open air. While this kind of pollution of the liquids could be secondary for some applications (like catalysis or organic reactions), it poses a significant limit on their usage as electrolytes, mainly when some water sensitive salts are dissolved inside the IL. Another issue is related to the higher viscosity of the liquids in comparison to the other media. Being composed mainly of large ionic species, these electrolytes display a specific movement hindrance of the molecules inside the solution bulk. In the end, we have to cite again the enormous number of ionic liquids that can be formed mixing different salts; each one of these ILs can be considered a solvent on its own, with its particular behaviour in respect to physical and chemical processes.

For all these reasons, little is still known about these systems, with the ionic liquids topic growing more and more of interest in the scientific community. More recently this kind of solutions attracted attention as electrolytes for electrochemical processes: the advantages of such type of media are

several. But the complexity of the organic molecules forming the salts, and consequently their cost, often poses a barrier to the widespread industrial usage of ILs.

4.3 Aluminium

Aluminium is the second most used metal in the world. Its properties include low density, high thermal and electrical conductivity, high relative tensile strength, superior malleability, easy machining and an excellent corrosion resistance. Al importance resides primarily in its usage as a base component for low weight alloys, for specific technological purposes in which high mechanical and chemical resistance, together with low weight, are required (Aeromotive, engines, energy devices...).

Its exploitation by humankind is quite recent. Despite its high abundance in the earth crust (it is the second metal by abundance, after Fe), Al purification from its ores posed a significant limit to Al industrial exploitation till the beginning of the 20th century (Due to the complexity of its refining, in the 19th century, aluminium was considered more rare and precious than gold or silver). The first success in obtaining a pure form of Aluminium from its ores dates 1825, by the hand of Danish chemist Hans-Christian, but we have to wait till 1886 for the first relatively inexpensive way to extract pure aluminium from its oxides by means of electrolysis (Hall-Heroult Process⁶⁵) and till 1887 for a method to obtain alumina from bauxite, the most common Al ore (Karl Joseph Bayer method⁶⁶). Nevertheless, despite all the efforts to lower the costs of a mass production process, the conjunction of these two methods was not considered viable until the beginning of 1900. Today the Bayer and Hall-Heroult processes are still used to produce bulk aluminium. The production starts from Al ores (like bauxite, containing high concentrations of Aluminium oxides and hydroxides). The mineral is crushed, dried and grounded; a small quantity of water is added in order to form a paste, which is dried under a steam flux in order to remove most of the silicon content. The obtained powder is then loaded into autoclaves, and treated with lime-caustic soda in order to separate aluminium oxide rich slurry from the admixture, which settles down as red mud). The slurry is then roasted in precipitators for various days, in order to make the Al_2O_3 settle at

the bottom. The electrolytic process implies the use of molten cryolite (Na_3AlF_6) at 950°C . Electric currents are induced in the mixture at 400kA, producing the break of the bond between the aluminium and the oxygen, and making liquid aluminium settle at the bottom of the reduction cell. This process, although still used today, is entirely energy consuming; for this reason, the majority of the manufacts produced today are obtained by recycling old Al items.

Apart from the bulk aluminium production, the market is moving more and more towards thin layer metal coatings. Its chemical, thermal and electrical properties could be useful in various industrial processes, in order to obtain artefacts with particular surface properties. In addition, its aesthetic features, the possibility to colourize aluminium surface by means of anodization, render thin Al layers an interesting solution for the design and fashion industry.

4.4 Electrodeposition of Aluminium from Ionic Liquids

The main issue related to aluminium usage in the form of thin films is the impossibility to electrodeposit it by means of conventional water-based electrolytes. Until today, the majority of the Al thin film production, both for aesthetic and technical purposes, is obtained using Physical Vapour Deposition (PVD) or Chemical Vapour Deposition (CVD) methods. These methods involve high temperatures, high vacuums, a lot of electrical energy and a significant amount of dead time to prepare the reaction chambers in between the deposition processes. Over the years various alternatives to these methods, via electrodeposition from different electrolytes, were tested. Aluminium was successfully deposited using the SIGAL process⁶⁷ during the '80s, but the involvement of toluene as an electrolyte in high-temperature environment posed great safety problems to the spoilage of this method in mass production. A safer and easy-to-use solution, discovered during the late nineties, relied on ionic liquids. It has been seen that the conjunction of an imidazole salt ($\text{R}'\text{R}''\text{Im}^+ \text{Cl}^-$, with RI and RII short aliphatic chains) with aluminium chloride (AlCl_3) created a substance that was liquid at room temperature; the first chloroaluminate ionic liquids were born. Some subsequent studies highlighted the possibility to obtain metallic

aluminium via electrolytic processes only from combinations of salts with molar ratios between [1:1.25] and [1:2.5] $R^I R^{II} \text{ImCl} : \text{AlCl}_3$ ⁶⁸; This because only these mixtures, called acidic⁶⁹ permitted the formation of the electroactive species Al_2Cl_7^- , responsible for the electrodeposition process. Many imidazole salts were tested to form ionic liquids; HmImCl, MmImCl, EmImCl, PmImCl, BmImCl were all studied for this application, leading only to small deposit variations during the aluminization process.

For our tests, the chosen ionic liquid was composed by 1-Buthyl-3-Methyl Imidazole Chloride (**Figure 67**) and Aluminium Chloride (BmImCl AlCl_3), used in molar ratios between [1:1.5] and [1:2]; it was produced by IoliTec (Germany), one of the partners of the consortium, and was used without further purification.

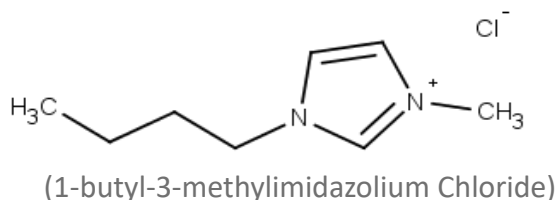
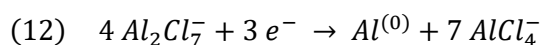


Figure 67 – The BmIm Cl molecule

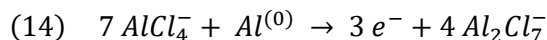
The following scheme summarizes the reactions which take place inside the ionic liquid. The first reaction (11) is related to the formation of the electroactive species Al_2Cl_7^- , responsible for the deposition phenomenon:



This species is sensitive to the ratio in which the two base salts are mixed; a significant decrease in aluminium chloride with respect to the imidazole salt leads in fact to the formation of a small quantity of dimer, to a more “basic” ionic liquid, and to the impossibility to deposit Al. The dimer can react with more AlCl_3 molecules, forming N order polymers but only the dimer seems to be responsible for the deposition process. During the electrochemical process, we can finally have the discharge of the electroactive species (12):



And the Al_2Cl_7^- regeneration, in the bulk of the IL (13) or on the anode, when it is made of aluminium itself (14).



In the end, it is important to notice the degradation reaction of aluminium chloride by means of atmospheric moisture (15). This reaction occurs in every chloroaluminate ionic liquid and is particularly dangerous because it is strongly exothermic.



The aluminium hydroxide is an electroinactive species and tends to precipitate inside the liquid as a dark grey powder, while hydrochloric acid is freed in the environment, posing a danger for both operator and machinery (corrosion issues). This last reaction is crucial for the working life of the ionic liquid because it could lead to a fast depletion of the electroactive species from the ionic liquid, and also to a worsening of the obtained deposit. IL moisture degradation is, in fact, the first limit for the industrial exploiting of the method; environmental water has to be kept low (at least below 50 ppm H₂O) in order to grant a long working life of the liquids. In an in-line set-up, this could be quite difficult to achieve (the SCAIL-UP project was mainly focused on that topic), while during lab-scale tests, environmental moisture can be kept under control using a glove box. For our experiments, an ITECO glovebox with a custom design was used. The internal environment was kept under nitrogen (Grade N4.0) under a slight overpressure (about 0.3 bar with respect to the outside pressure). Low levels of moisture were also maintained by the use of phosphoric anhydride inside the main chamber, and by regularly circulating the process gas through zeolite filter. A better explanation of the deposition process can be found in paragraph **6.1**.

4.5 Study on the deposition conditions

Many issues remained unresolved regarding the effect of mixing and temperature on the obtainment of Al-coated surfaces. In order to shed some light on this topic, a campaign of deposition tests was endured. Particular interest has been paid on the effect of sonication on the crystallographic growth of Al; in the literature, there was no evidence regarding a study on the influence of this mixing methodology in changes in texture, surface

morphology and corrosion resistance on the obtained metallic layers. To better define sonication influence on the final coating, in respect of other mixing methods, and on temperature increase, a series of deposits were obtained, first introducing temperature and mixing alone, and then trying to mesh the two effects on the same bath, as schematized in **Figure 68**.

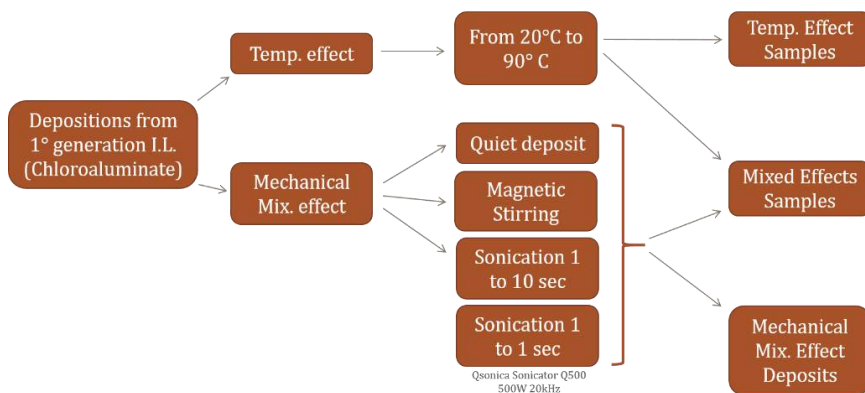


Figure 68 – The experiment scheme

Three samples for each different deposition condition were prepared by galvanostatic deposition. Deposition yield, as well as potential/time curves, were recorded and analysed. The obtained samples were then characterized by Scanning Electron Microscopy (SEM), X-Ray Diffraction (XRD), Roughness analysis, OCP and corrosion tests. The results of this experiment were published in the article which can be found in *Appendix C: Article “Aluminium Electrodeposition from Ionic Liquid: Effect of Deposition Temperature and Sonication”*.

4.6 Rotating Hull Cylinder (RHC)

Planar Hull Cells (HC) are commonly used by Plating Industries worldwide to establish operating parameters, to perform daily maintenance (studies on the ageing of the electrolytic baths) and in considering modifications or improvements in a defined plating process. In fact, Hull Cells are small test electrochemical cells, with a rectangular trapezium shape, in which a planar anode is placed in front of an angulated (45°) cathode (**Figure 69**).

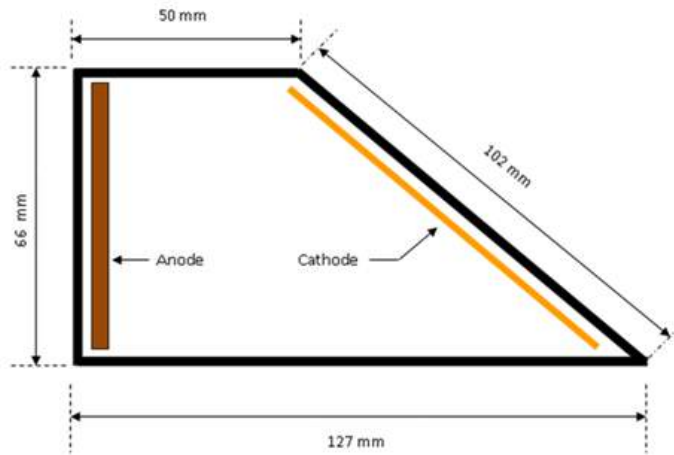


Figure 69 – A traditional Hull Cell scheme

The particular geometry used permits to obtain metallic deposits on the cathode with different degrees of current density and different surface finishing, thus evaluating both phenomenologically and theoretically (using a current distribution model) the best parameters in order to obtain a specific surface finishing during industrial processes. These tests could also be used in order to define the exploiting of an electrolyte or to assess the effect of special additives on the finishing⁵.

Ordinary planar Hull Cells have certain limitations that hinder their predictive power in respect to the real electroplating process. In electroplating industry, the majority of the used baths is maintained under some kind of mixing, in order to increase the mass transport of the species, thus maximizing the effect of the levelling agents present in the bath. This mixing phenomenon cannot be reproduced in a planar Hull Cell without

losing parameters determination accuracy. To overcome this problem, a particular kind of Hull Cell was designed, called Rotating Hull Cylinder (RHC)^{70,71}. In its core design, this cell is made by a circular chamber with an external circular anode, an internal rotating cylindrical cathode and an inert barrier in between the two electrodes (**Figure 70-2**). This particular design permitted both to differentiate an array of current densities on the cathode, thus modifying the hydrodynamic conditions of the bath by the variation of the rotating speed of the central electrode.

4.6.1 Design of the Cell

RHC was first designed the nineties (there is a US patent N. US5228976 from 1990), but no evidence of the use of such devices to study the electrodeposition process in ionic liquids is present in literature till today. Nowadays, few commercial cells are present and aren't designed to withstand the harsh ionic liquid environment for a long time without corroding and falling apart. Also, these cells are designed to perform ex-situ measurements; a test electrolyte sample is usually taken from the bath and placed inside the cell vessel in order to use the apparatus. The particular sensitivity of the chloroaluminate ionic liquids to the atmospheric moisture renders this procedure unviable, especially if we need to draw the ionic liquid from the pilot plant and take it outside the glovebox.

In order to overcome these related issues, I've managed to design and build a particular RHC, following two major guidelines:

- The cell has to be chemically resistant to the ionic liquid environment at temperatures below 150°C;
- The cell has to be used in situ, directly in the pilot plant, to avoid electrolyte degradation.

The main corrosion related issues were resolved during the design by choosing chemically inert plastic or ceramic materials. For pieces in direct contact with the ionic liquids, PTFE (Teflon) was used. To permit a smooth and long lasting rotation of the cathode along its axis, a ceramic Zirconia ball bearing was chosen, a solution which granted us an optimal chemical resistance and cleaning ease. Zirconia shows, in fact, a good compromise between HCl/IL resistance and cost; it is a conventional material for ball

bearings working in low pH environments at high temperatures, and it is also used as inert media in nanoparticles synthesis in various ionic liquids⁷². A test on the behaviour of both metallic and ceramic ball bearings was performed towards exposure to the IL, both inside the liquid (BMImCl/AlCl₃ [1:1.5]) and in a rich gaseous HCl environment. The spent ionic liquid was used for these tests. In order to enrich its HCl content, it was handled under the fume hood, reproducing the worst working conditions for the IL. Two samples of metallic and ceramic ball bearings were then inserted into the ionic liquid. After a week, the metallic bearings tended to clog due to the formation of corrosion by-products, while no such problems were seen for the ceramic ones; after a clean-up by acetone and water, the zirconia BBs reacquired the natural rolling qualities.

RHC Cathode rotation was permitted by a stepper motor; this particular type of actuator was preferred to the more common DC current motors for the following motifs:

1. Stepper motors have no direct contact between stator and rotor, thus preventing clogging due to rust formation (Common in DC current motors);
2. Metallic stepper motor ball bearings can be easily changed with ceramic (zirconia) ones;
3. Stepper motors can be easily programmed to achieve precise rotation speeds without the need of a feedback system (like the ones needed for their DC counterpart). Feedback systems are usually mechanical or optical and sensitive to dirt and ageing. On the contrary, the speed of stepper motors is controlled by current pulses from an external circuit; rendering, in fact, difficult for the stepper motors to be affected by environmental biases.

The used actuator was an SY42STH47-1206a bipolar stepper motor bought on RS (www.rs-components.com). The control on the cathode rotation was executed using an Arduino Uno board as a microprocessor, and an ADAFRUIT TB6612 (www.adafruit.com) as a motor driver for the stepper motor. A DC 12V 2.4A power supply permitted to reach 500 RPM, more than enough for the system we wanted to study. The rotation speed of the cathode was set using a custom made program. A complete summary of the

cabling, the program used and the cell design can be seen in *Appendix D: RHC Schematics*.

In order to permit the Cell usage directly in the pilot plant, a particular upside down design was also adopted; no liquid container for the electrolyte was then needed, as in the commercialized RHCs (**Figure 70**). This enabled the direct immersion of the deposition chamber inside the pilot plant's bath. Also, easiness in electrodes change was considered:

- The circular external anode could be easily changed unscrewing the four outer bolts, making possible the use of any foil material.
- The internal rotating cylinder used is a standard industrial 8 mm diameter brass tube, inserted into the ball bearing and fixed to the stepper motor spindle by a splint or by a stepper motor flexible shaft adapter.

These fixing solutions permitted the use of any different combination of foil anode and tube cathode materials for a two-electrode cell set-up.

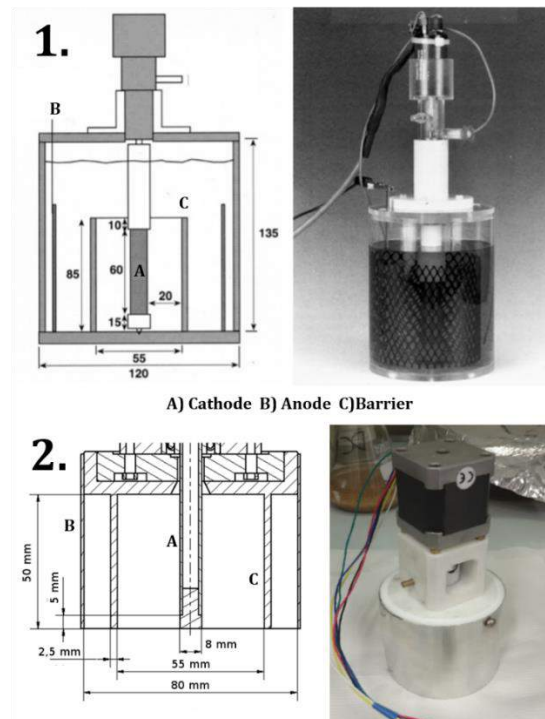


Figure 70 – Comparison between commercial RHCs (1.) and our RHC design (2.)

In the end, the designed RHC proved to be quite cheap, the total cost of the material needed to build it from scratch was below 100 €.

4.6.2 Testing of the cell & FEA model

One of the aims of the cell development was the study of a predictive model for the deposition phenomenon from chloroaluminate ILs, with the aid of a Finite Elements Analysis (FEA) theoretical model. This was done in order to define a procedure to optimize current density, length of the cathodes and rotation speed for this innovative RHC design, to obtain a current density distribution along the rotation axis of the cathode resembling the profile typical of the HC for ILs.

But, to refine the model, some experimental data from deposition samples were needed. The cell was firstly tested towards an aqueous electrolyte, specifically the **Watts high pH Bath** for the electrodeposition of Nickel, prepared as follows:

- Nickel Sulphate (240g/l);
- Nickel Chloride (45 g/l);
- Boric Acid (30 g/l);
- Temperature 40°C;
- pH 4.5-5.6;
- Current density 2 A/dm².

For these depositions, a Mixed Metal Oxide grid was used as the anode. Common 8 mm industrial brass cylinders were used as cathodes, without any further surface mechanical treatment. Before their usage, the tubes were sonicated in acetone for 5 minutes, washed using bidistilled water, dipped for 1 minute in a 0.1 HCl solution and finally rinsed with bidistilled water. Only the outer surface of the cylinders was in contact with the electrolytic bath, thanks to a plastic screw placed on the bottom, preventing the contact between the ionic liquid and the inner surface of the brass tube. In order to obtain different current densities, Ni deposits were produced varying rotation speed (0 RPM, 150 RPM, and 300 RPM) and varying tip length. The obtained coated tubes were then cut, embedded in a plastic matrix, and the obtained cross sections were analysed using optical microscopy to get the thickness evolution of the Ni coating along the cathode axis (**Figure 71**).



Figure 71 – A Ni deposit obtained using the cell with a rotating speed of 300 RPM (left) and the sample preparation performed to obtain deposit thicknesses (right)

A theoretical model of the process was then prepared using COMSOL Multiphysics FEA program, coupling Navier-Stokes⁷³, Nernst-Planck⁷⁴ and First Maxwell equations in a system of partial differential equations⁷⁵ (**Figure 72**).

$$\begin{aligned} k \nabla^2 \mathbf{v} - \rho (\mathbf{v} \cdot \nabla \mathbf{v}) - \nabla P &= 0 \\ \nabla \cdot \mathbf{v} &= 0 \\ \frac{\partial C_i}{\partial t} + \nabla \cdot (-D_i \nabla C_i - Z_i u_i F C_i \nabla \phi_i + \mathbf{v} C_i) &= R_i \\ -\nabla \cdot (\sigma \nabla \phi_i) &= \rho \end{aligned}$$

Figure 72 - The equation system used for the simulation

This method has proven reliable for the description of general electrochemical processes carried under mixing conditions⁷⁵. The simulation domain was defined exploiting the axial symmetry of the RHC. Also, for the resolution of the system, boundary conditions such as pressure, velocity field, electrolyte potential and concentration of the electroactive species were introduced. To optimize the setup three control variables were used, corresponding to parameters that are tunable in our new RHC:

1. Average current density applied to the cathode;
2. Length of the cathode;
3. Rotating speed.

They have been swept very finely, and the profiles were normalized with respect to the average current density and compared with the analytical

solution of the cell. An optimal adherence between the model and the experimental results was found (**Figure 73**); it was considered as a proof of a good robustness of the device under working conditions.

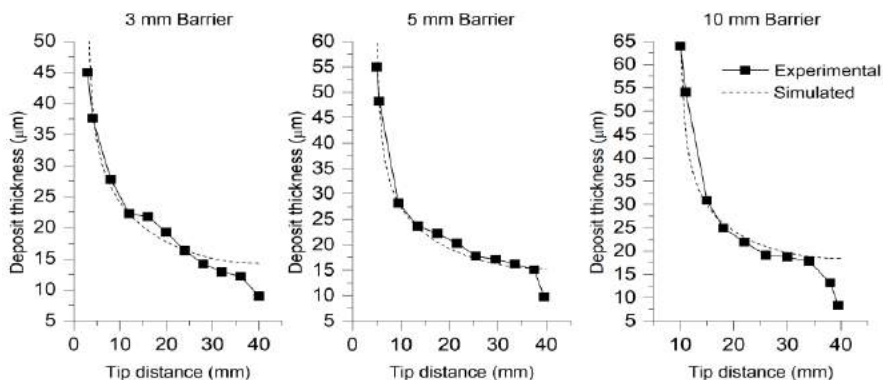


Figure 73 – Comparison between the experimental (continuous line) and the simulated (dotted line) thicknesses of various Ni deposition samples, obtained with a rotation speed of 300 RPM

The variation between the simulated and experimental thicknesses that is visible on the topmost zones of the samples (tip distance >35 mm) can be attributed to the meniscus effect, not considered in the simulated model.

The cell was then tested towards deposition of aluminium from ionic liquids. The IL used was BMImCl/AlCl₃ [1:1.5], while the anode and the cathode were respectively a pure (99,9%) Al foil, and 8mm brass tubes (the same used in the nickel tests). Prior to deposition, the cathode was prepared by immersion in HCl 0.1 M for about 1 minute, rinse with water and by acetone. Anode was left for about 2 minutes in a NaOH 0.1 M solution and then cleaned with water and acetone. Once mounted, the RHC was moved inside the glove-box pre-chamber, under vacuum conditions, for about 15 minutes, in order to get rid of adsorbed water molecules.

The depositions were then performed galvanostatically, using a current density of 5mA/cm², and with a deposition time of 2 hours. Depositions were conducted with a rotation speed of 150 RPM and 300 RPM, varying the tip height; an example of one of the obtained samples can be seen in **Figure 74**.

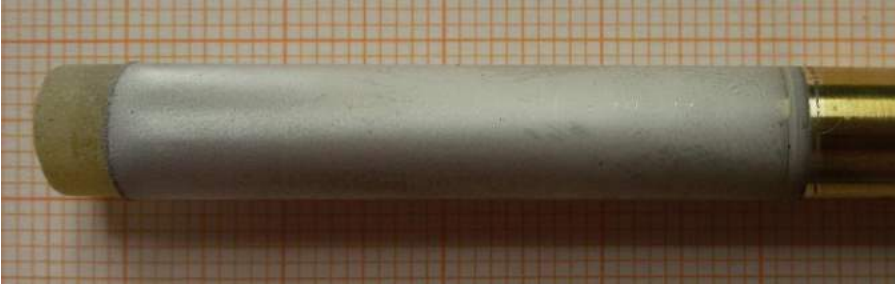


Figure 74 – An Al deposit obtained at a rotation speed of 300 RPM

4.7 Electrodeposited Aluminium as thermal barrier in turbine vanes

Turbines are highly sophisticated devices, designed to work for long duty-cycles in high temperature and harsh environment. Many industrial processes are supported by these devices, especially in the energetic and oil and gas field; their faults or even an efficiency loss could lead to an enormous economic loss, and eventually to the halting of the processes in which are involved. For these reasons, each turbine component is highly engineered to fulfil its work duty for the longest time possible.

The primary cause of fault by these devices can be identified as high-temperature corrosion on turbine vanes. These parts are placed along the turbine rotor, their erosion could, as an example, unbalance the turbine shaft during operation, leading to vibrations, to the deterioration of the ball bearings and in the damaging of the whole device. The corrosion phenomenon is due to oxygen and sulphur diffusion onto the blade alloy surface. The morphology of the corrosion layers is then typically characterized by a thick, porous layer of oxides with the underlying alloy matrix depleted in chromium, followed by internal chromium-rich sulphides

76–78.

A considerable research effort has been made to design thermal barriers for these components, as protective coatings to prevent interdiffusion processes. The most common thermal barriers are nowadays made by a thick aluminium coating above the vane surface. Aluminium results in an optimal material for this purpose. It forms a continuous and self-healing alumina oxide scale on the surface, preventing the inward diffusion of oxygen or sulphur into the base alloy. The aluminization process is commonly performed by Chemical Vapour Deposition (CVD) or pack cementation; these methods require a significant extent of time to prepare samples, costly consumables and high temperature. Also, some homogeneity problems could arise for the aluminization of complex shapes and cavities. Al Electrodeposition, on the other hand, had proven to be a perfect candidate in the obtainment of thick, continuous and homogeneous deposits, even for substrates with a complex shape. For this reason, a comparative study on the high-temperature corrosion resistance of two different aerospace alloys (CoNiCrAlY and Inconel 738) aluminized by pack

cementation and Ionic Liquid Deposition has been performed. The coated samples were aged using isothermal test; during this process coating composition, thickness, hardness and crystallographic features were analysed to define changes in the anticorrosion properties between the two production methods. This article can be found in *Appendix E: Article “Aluminizing via Ionic Liquid Electrodeposition and Pack Cementation: A Comparative Study with Inconel 738 and a CoNiCrAlY”*.

5 Conclusions

5.1 FEXRAV experiments and Pd deactivation

The work done with respect to the study of the deactivation of palladium, used as anodic catalyst for direct alcohol fuel cells, was conducted using novel in-situ synchrotron techniques. Such methodologies proved to be very powerful, allowing us to map almost simultaneously both the nature of the inquired species and their electrochemical behaviour. However, the difficulty in obtaining beam time poses a limit to the exploitation and development of such methodologies. Notably, FEXRAV proved to be a versatile tool to investigate the nature of the phenomena occurring on the electrodic surface, permitting the user to follow the evolution of a system under electrochemical stimulus in real time. The only drawback of this methodology is related to the need to optimize this technique with respect to the system we want to study; for this reason, a particular tweaking of the experimental set-up has to be performed for each studied system.

During the course of my PhD, I've firstly managed to implement the FEXRAV technique for the study of dispersed catalytical metal particles, with a focus on the behaviour of palladium used as an anodic material for DEFCs. The new FEXRAV cell design permitted a precise acquisition of the fixed energy XAS signal (see **3.2.5**) in a half fuel cell set-up and showed promising also to obtain electrochemical/XAS data of catalysts using a working full fuel cell configuration. Moreover, the new technique which combined the grazing

incidence geometry with the FEXRAV technique, the GI-FEXRAV technique, showed promising for the acquisition of the same set of data, also granting the following advantages:

- No issues related to the use of dispersed systems (like surface/volume signal mediation, difficulty in preparing the ink and in reproducing the same catalytical loading between different tests);
- Higher signal with a lower catalytical loading (the grazing incidence geometry permits to sample a full fraction of the electrode, thus enhancing the fluorescence yield);
- Possibility to study the model surfaces before and after the cycling (to define changes in surface morphology, as an example);
- Possibility to finely tailor the catalytical surfaces, changing the degree of coverage and metal/metals used as catalysts, through the use of E-ALD and SLRR methods.

Regarding the study of the palladium deactivation process, significant evidence of its dissolution during anodic scans were collected. This phenomenon was visible during both the half-cell and the full fuel cell experiments, and it was also confirmed by chemical speciation models. A competitive chemical deposition mechanism, produced by ethanol as a reducing agent, was also suggested. Only this phenomenon could, in fact, justify the levelling of the fluorescence intensity curves seen in the KOH + EtOH experiments, and the subsequent increase in the signal once the oxidative potential went over (seen in the full fuel cell experiment, paragraph **3.2.5.2**). A ripening process can be suggested for these systems, as also seen in Kevin Zucchi's Bachelor thesis⁷⁹. Here, the same catalyst nanoparticles were studied using Transmission Electron Microscopy (TEM) identical location methods⁸⁰ before and after oxidative cycles in both KOH and KOH + EtOH electrolytes. This study highlighted, especially for the alkaline + fuel electrolyte, a certain degree of ripening of the palladium nanoparticles, with the disappearance of the smallest entities, and the increase in the dimension of the biggest ones. The reported results confirmed this trend, but more work will be needed to better understand this phenomenon and to optimize also the newly presented techniques.

5.2 Aluminization from Ionic Liquids

The work on the aluminium electrodeposition from 1st generation ionic liquids helped to better understand the influence of process parameters on the obtainment of the final coatings and, despite its industrial orientation, permitted a better understanding of the phenomenon that guides these operations. This research work also allowed to define the best operative conditions for the pilot plant, in order to obtain thick aluminium coatings on real substrates, like turbine vanes. The research effort helped also to design and produce a new Rotating Hull Cell, which demonstrates as a reliable device to study diffusion phenomenon in the industrial set-up. This device will be surely helpful to study the behaviour of newly designed electrolytic baths, thanks also to its design flexibility. The obtained coatings were in the end characterized with respect to hot corrosion resistance by the isothermal test. The experimental results showed a lower resistance of the samples obtained by ILs compared to the Pack Cementation samples. Despite the experimental outcome, the research undergone on the development of the deposition process will be surely useful in future for the study and improvement of other industrial processes based on “exotic” electrolytes.

6 Appendix

6.1 Appendix A: Article “Computational Speciation Models: A Tool for the Interpretation of Spectroelectrochemistry for Catalytic Layers under Operative Conditions



JES FOCUS ISSUE ON MATHEMATICAL MODELING OF ELECTROCHEMICAL SYSTEMS AT MULTIPLE SCALES IN HONOR OF JOHN NEWMAN

Computational Speciation Models: A Tool for the Interpretation of Spectroelectrochemistry for Catalytic Layers under Operative Conditions

G. Montegrossi,^a A. Giaccherini,^{b,x} E. Berretti,^b F. Di Benedetto,^{a,c} M. Innocenti,^{b,x,z} F. d'Acapito,^d and A. Lavacchi^e

^aIGG, CNR, Florence 50121, Italy

^bDepartment of Chemistry, Università degli Studi di Firenze, Florence 50019, Italy

^cDepartment of Earth Sciences, Università degli Studi di Firenze, Florence 50019, Italy

^dIOM, CNR, c/o ESRF, Grenoble 38043, France

^eICCOM, CNR, Florence 50019, Italy

In this study, the first coupled FEXRAV and chemical speciation modelling study of the Pd deactivation is presented. Due to the high brilliance of synchrotron light, FEXRAV can investigate deeply buried surfaces. More specifically, we directly analyzed the evolution of the Pd/C catalytic layer during a voltammetric cycle, through a specifically designed electrochemical cell. Still, we observed a complex interfacial chemistry of Pd, which impairs a straightforward interpretation of FEXRAV data. Exploiting thermodynamic chemical speciation modelling we were able to overcome this issue. The study leads to three main results: 1) the confirmation of the relationship between the change of the Pd/Pd(II) ratio and the change of the Fluorescence intensity 2) the investigation of the deactivation mechanism 3) the identification of the relevant species leading to the electrodisolution of Pd under operative conditions. This study opens new perspectives for the application of the chemical speciation modelling to the study of the deactivation mechanism of Pd in Pd/C catalytic layers under operative conditions in different electrolytes.

© The Author(s) 2017. Published by ECS. This is an open access article distributed under the terms of the Creative Commons Attribution 4.0 License (CC BY, <http://creativecommons.org/licenses/by/4.0/>), which permits unrestricted use of the work in any medium, provided the original work is properly cited. [DOI: 10.1149/2.071171jes] All rights reserved.



Manuscript submitted April 3, 2017; revised manuscript received July 21, 2017. Published August 11, 2017. This paper is part of the JES Focus Issue on Mathematical Modeling of Electrochemical Systems at Multiple Scales in Honor of John Newman.

In recent times, Palladium-based electrocatalysts proved to be able to promisingly substitute Pt in several electrocatalytic applications due to their lower cost and higher availability.¹ Moreover, Pd catalysts resulted very effective in direct alcohol fuel cell (DAFC). One of the benefits consists in the bypass of the deactivation process occurring in Pt catalysts due to reaction with CO.^{2,3} Nowadays, the main issue still preventing full exploitation of such electrocatalytic materials is their anodic deactivation, which is not fully understood and manageable. In fact, although the origin of the deactivation has been related to the formation of an oxide layer on the Pd surface, its formation mechanism is still an open question.⁴ Moreover, other studies suggested that Pd electrodes are also subjected to electrodisolution under operative condition.⁵ In principle, the latter process is competitive with the formation of the oxide layer and it is not observable by means of ex-situ techniques. In this context, a natural follow-up of the conventional ex-situ experiments are in situ/operando spectroelectrochemical measurements, performed to investigate the competition between these two processes under operative conditions. For operative conditions, we refer to the strongly anodic and basic conditions usually applied to the catalytic layer for the electrooxidation of alcohols. In the same context, the catalytic layer is usually intended as the place where the interaction between the electrolyte, the catalysts and the support occurs.⁶ Several in-situ/operando techniques applied to catalysts are reported in literature, most of them are carried out on model systems with specific surface preparation or they require concentrated materials (i.e. on Pd electrodes).^{7–10} As shown by Minguzzi et al., the Fixed Energy X-ray Absorption Voltammetry¹¹ enables the direct study of the oxidation state for chemical species under operando conditions. Recently, our group reported an operando study of Pd half-cell through FEXRAV.¹² Our results pointed out that FEXRAV alone is not able to clearly distinguish the different species of the same valence state (i.e. Pd(II)). Hence, even considering only the contribution due to the formation of the oxide layer (PdO) and the electrodisolution of Pd (Pd²⁺ solvated species) to the deactivation process of Pd/C electrocatalyst, the analysis of the experimental data could not identify which

process is prevailing. On this basis, our aim is to present an integrated theoretical-experimental method to draw a conclusion on this subject.

Methods

Details of the FEXRAV experiment.—Recording the time evolution of the sample response to X-rays at a fixed energy close to the absorption edge of an element, FEXRAV reckons the valence states of such element even in a complex matrix under an electrochemical stimulus (i.e. during a cyclic voltammetry).^{11,13} Thanks to the high penetration of X-rays, it delivers information on X-ray absorption data through the walls of an electrochemical cells, with only minor design changes with respect to a standard electrochemical cell. Thus, it constitutes an ideal tool to investigate standard catalytic layers in operative conditions. In the setup hereby discussed, the lower detection limit is evaluated to be approximately 10¹³ atoms/cm². In order to perform our experiments we used a standard three electrode cell, specifically designed (3D model in Figure 1a) to be mounted in the experimental XAS chamber of the LISA beamline at ESRF.¹⁴ The schematic of the experimental setup is presented in Figure 1b.

In the FEXRAV study of the Pd half cell, Pd/C nanostructured catalysts were involved. The Pd/C catalysts were synthesized according to the procedure reported in Refs. 15,16. The anode catalytic ink was prepared by mixing and sonicating the Pd/C catalyst (100 mg) with water (400 mg) and a 5 wt% nafion solution. The final charge of Pd on the electrode is approximately 4 mg/cm², a target loading selected to achieve the optimal sensitivity in the FEXRAV experiment. The electrochemical measurements have been performed by means of a PAR263 potentiostat installed at the BM08 beamline. The results obtained studying two different electrolytic solutions are presented in this paper: 1) KOH 2 M and 2) EtOH 2 M + KOH 2 M.

Concerning the beamline set up, the monochromator was equipped with Si(311) flat crystals, with an energy resolution $\Delta E/E \approx 10^{-5}$, a spot size of about 2×0.5 mm and a flux at the sample position up to

^xElectrochemical Society Member.

^zE-mail: andrea.giaccherini@unifi.it; minnocenti@unifi.it

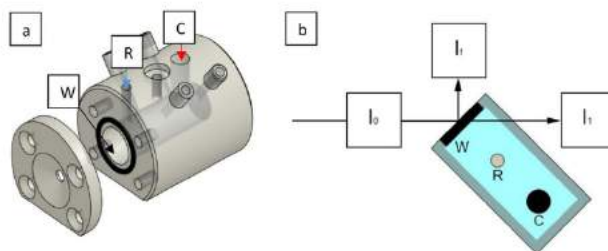


Figure 1. a) 3D model of the electrochemical cell used during the FEXRAV measurements with the position of the working electrode (W), reference electrode (R) and counter electrode (C); b) experimental setup for fluorescence (I_f) and transmission (I_t) measurements. I_0 is the incoming monochromatic X-ray radiation.

10^{10} ph/s. All spectra were registered at room temperature, with reference to a metal foil, simultaneously analyzed in a second chamber located after the former. According to this procedure, the energy calibration was let available during the whole measurement. Reference materials were: elemental Pd under the form of a metal foil (Goodfellow) and PdO (Sigma Aldrich). This latter sample was prepared dispersing and homogenizing an appropriate amount of microcrystalline powders in cellulose, and pressing the mixture to a self-supporting half inch pellet.

Numerical modelling.—Phreeqc formalism.—We performed our calculation under the *phreeqc* formalism,¹⁷ taking into account aqueous species equilibria in a reference database. The solid phases are considered through dissolution/precipitation reactions, and their stability is reported as the logarithm of equilibrium constant of formation (log K) at standard temperature and pressure condition (i.e. 25 °C and 1.0132 bar) from the master species.^{18,19} Only one master species is associated to each element or element valence state (for instance Fe^{3+} for ferric iron), one to the hydrogen ion, one to water and (formally) one to the aqueous electron. In this work, $\text{Pd}^{2+}_{(aq)}$ acts as master species while all the other species coming from the dissolution of metallic Pd in the half cell are secondary species ($\text{Pd}(\text{OH})^+_{(aq)}$, $\text{Pd}(\text{OH})_2$, $\text{Pd}^+_{(aq)}$, etc.). The master species are the “building blocks” used in the *phreeqc* formalism to write all chemical equations: they are related to the secondary species, in fact, by means of formation reactions involving the master species as a reactant (e.g. $\text{Pd}^{2+} + 2\text{OH}^- = \text{Pd}(\text{OH})_2$, $\text{Pd}^{2+} + e^- = \text{Pd}^0$, etc.) and the relative equilibrium constant logarithms are included in the calculation (as a function of temperature). These species are present in a single phase, an aqueous solution. On this ground, the aim of the *phreeqc* formalism is the definition of a system of algebraic homogeneous equations describing the equilibrium conditions for different thermodynamics variables such as the activities of aqueous species (including water), ion-exchange species, surface-complexation species, gas-phase components, solid solutions, pure phases, aqueous charge balance, gas-phase equilibria and ionic strength. Such algebraic system is assembled taking into considerations all the residual function (denoted by f) describing the relevant equilibria. The residual functions are defined as the difference between a global constant and the combination of specific variables for each species or phases. Hence, for each set of values of the thermodynamics variables, defining a certain state of the system, the residual functions describe the “distance” of the state from the equilibrium. On this basis, the equilibrium condition corresponds to the set of values for the thermodynamics variables that let all the residual functions equal to zero. To compute the results, each residual function is reduced to contain a minimum number of variables (called the unknown masters), so that the number of functions equals the number of variables. The unknown masters for aqueous solutions are the natural log of the activities of master species ($\ln a_m$), the natural log of the

activity of water ($\ln a_{H_2O}$), the ionic strength (μ), and the mass of solvent water in an aqueous solution (W_{aq}). The system is then computed and solved by means of the Newton-Raphson technique, which proceeds through the assembling of a Jacobian matrix containing the derivatives of the residual functions by the unknown master. Thus, this matrix describes the thermodynamics of the multi-equilibria system and its diagonalization leads to the equilibrium conditions. The analytic expression of each residual function and of the related derivatives has been developed and implemented in the *phreeqc* software. For instance, the equilibrium between the aqueous phase and pure solid phases is described under the following assumptions:

- 1) The activity of the pure phase is 1.0
- 2) The additional unknown master for each pure solid phase is the mole of the pure phase present in the system (n_p , where p refers to the p^{th} phase)
- 3) The mass-action law holds

Under this assumptions the pure phase equilibria are described by the mass-action law:

$$K_p = \prod_m \frac{c_{m,p}}{a_m}$$

Where K_p is the equilibrium constant with the p^{th} phase, $c_{m,p}$ is the stoichiometric coefficient of the aqueous master species (positive if the product of the desorption reaction and negative otherwise), a_m is the activity of the m^{th} species (it is an unknown master). Eventually, M_{aq} is the number of aqueous master species.

On this basis a new residual function can be defined:

$$f_p = \ln K_p - \sum_m c_{m,p} \ln a_m$$

The total derivative of the residual function in terms of the unknown master is:

$$d f_p = \sum_m c_{m,p} d \ln a_m$$

Chemical speciation in aqueous solutions is not uniquely defined but depends on the theoretical formulation of mass-action equilibria and activity coefficients (e.g. Davis, Pitzer or Debye-Huckel activity model);¹⁷ in other words, the numerical solution of the system is model-dependent. Some aqueous speciations can be analytically determined, but operational definitions and assumptions are still unavoidable. Accordingly, the equilibrium is computed with a reaction-path calculation, i.e. a sequence of mass-transfer calculations that follows defined phase (or reaction) boundaries during incremental steps of reaction progress.

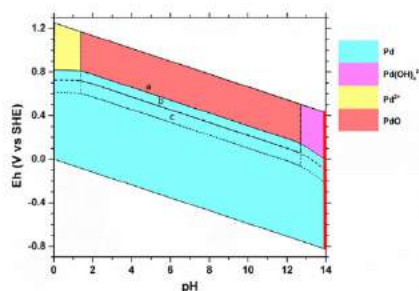


Figure 2. Pourbaix diagrams of the Pd-O-H system a) $[Pd] = 1 \cdot 10^{-3}$ mol/kgw b) $[Pd] = 1 \cdot 10^{-6}$ mol/kgw c) $[Pd] = 1 \cdot 10^{-10}$ mol/kgw.

In this study, the considered gas species, i.e. $H_2(g)$ and $O_2(g)$, are computed defining the corresponding partial pressures, and in the database are present the dissolution reactions (e.g. $O_2(g) = O_{2(aq)}$) and the corresponding constants. Accordingly, the presence of oxygen or hydrogen in any redox reaction is linked to their partial pressures. These latter are monitored as the result of an evolving chemical system in any given thermodynamic conditions.

The Pd-O-H system.—Numerical models for the chemical speciation require comprehensive thermodynamic databases. Although today's geochemical databases are quite complete, including the most common reactions and reaction constants, some equilibria typical of specific environments may be not present. Accordingly, the thermodynamic properties of some chemical species relevant to our model have been checked, and added, to the *phreeqc* *water4qt.dat* database.³⁰ Specifically, Palladium hydroxylates have been added according to the work of Mountain and Wood.²³

Modelling of the predominance charts and of the FEXRAV signals.—In the present study, the relationships between the main phases of the Pd-O-H system (Pd and water solution) are studied through the use of Eh versus pH (or “Pourbaix”) diagrams, calculated according to the point-by-point mass balance method (referred also as the grid method).^{22,23} Under this approach, a grid is defined by the span of the potential (Eh—with respect to the standard hydrogen electrode), pH and the chosen resolution (0.01 logarithmic units in both the Eh and pH axes, in the present case). Then, the chemical speciation for a given total amount of the element of interests is computed according to the *phreeqc* formalism³² for each given point of the grid. The results are rendered directly by coloring each species differently and plotting each point of the grid with the color of the predominant species (as depicted in Figure 2). The predominant species (in the aqueous or solid phase) is identified as the species with the highest amount (moles) at the equilibrium.

The modelling of the FEXRAV signal relies on its dependence on the Pd chemical speciation in the Pd-O-H system. For a given amount of Pd, the chemical speciation is computed at each potential applied during the voltammetric scan. Thus, the Pd-bearing species exhibiting the higher amount of moles is considered prevalent, whereas species with an amount less than 10^8 times lower than the former are neglected in the presentation of the results.

Results

Pourbaix predominance charts.—The predominance charts were computed in a grid limited by the conventional water stability field from 0 to 14 pH units. The choice of the concentration of the master

species were dictated by the possibility of an immediate comparison with selected Pourbaix diagrams available in the literature: Mountain and Wood,²³ Naoto²⁴ and Pourbaix et al.²⁵ It is noteworthy to mention that the former articles refer to calculations performed using the mass balance method, and including results calculated by using up to five different databases, whereas the latter presents results obtained using the “line method” (i.e. depicting the boundary defined by Nernst equations). Figure 2 shows the Pourbaix diagram for the Pd-O-H system, where our point-by-point mass balance approach leads to very close agreement with all the cited works. Only a small difference can be evidenced between the Pourbaix et al.²⁵ study and the present one, and near the stability boundary of water, where our calculations predict the predominance of $Pd(OH)_4^{2-}$ (Palladium tetrahydroxylate), whereas Pourbaix et al. reports PdO_2^{2-} .²⁵

As the total amount of Pd assumed in the calculation increases, the only changes in the plot deal with the Pd/Pd(II) boundary, because higher Pd contents stabilize the solid phases. This is due to fact that Pd solubility, dependent on speciation, is in any case limited. Under the operative conditions (pH = 14 and anodic potential), the relevant boundary is $Pd/Pd(OH)_4^{2-}$ while the fractional amount of PdO is generally two orders of magnitude lower with respect to both Pd and $Pd(OH)_4^{2-}$.

Fluorescence.—The simultaneous acquisition of the electrochemical and FEXRAV signals from the electrochemical layer required a specific choice of the energy of the incident X-ray beam. Figure 3a depicts two X-ray Absorption Near Edge Spectroscopy (XANES) spectra of the reference materials, Pd and PdO. The difference between the XANES spectra of Pd and PdO is apparently maximized at 24370 eV. It is worth to notice that at this energy, the higher is the signal intensity, the lower is the fraction of Pd(0) contributing to the signal. On this ground, FEXRAV signals have been registered by means of the Fluorescence detector, while performing a cyclic voltammetry from -0.2 V to 1.2 V (RHE) with a scan rate of 1 mV/s, irradiating the electrochemical cell with a monochromatic persistent beam set up at 24370 eV. Apparently, at anodic potential we observe an increased signal intensity, and at the end of the cathodic scan the fluorescence signal is lower than at the beginning of the anodic scan (Figure 3b).

Speciation.—The chemical speciation modelling of this system under the voltammetric stress can be efficiently implemented defining analytical fractional amount readily usable. To this end, we calculated a “slice” of the Pourbaix diagram in operative condition (red vertical line in Figure 2) corresponding to the range of potential applied to the electrode. Then a polynomial function has been fitted on the numerically calculated fractional amounts against Eh. Such function constitute the esteem of the fractional amount, as a function of Eh, used to follow the chemical speciation during the voltammetry. The speciation models revealed that Pd and $Pd(OH)_4^{2-}$ are the most relevant species. In fact, the third species by abundance (PdO) has a fractional amount not higher than $3 \cdot 10^{-4}$ while the other Pd-bearing species are always lower than 10^{-7} . Regarding the effect of ethanol on the equilibrium speciation the results for a KOH 2 M and EtOH 2 M solution are equivalent to the one for the solution KOH 2 M since the only effect of the EtOH at the equilibrium is to be oxidized to CO_2 and H_2O . However the reaction is so slow that it has no practical meaning in our context. Hence, for our purposes the Pd-O-H and Pd-C-O-H systems are equivalent.

Comparison between experiment and modelling.—Figure 4 shows the FEXRAV data for a KOH 2 M solution together with the corresponding calculated speciation distribution. The FEXRAV signal shows a periodic oscillation in response to the potential ramps. A further apparent feature of Figure 4, is that the oscillation between maxima and minima in the FEXRAV signal (whose shape, amplitude and phase are almost constant throughout the whole experiment) are combined with a general linear trend decreasing the signal intensity. This suggest that FEXRAV intensity is eventually not only determined by alternation of different redox states of solid Pd-bearing species.

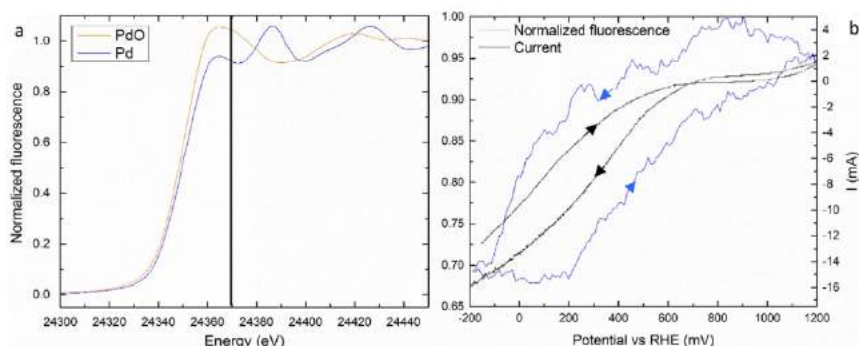


Figure 3. a) XANES spectrum for Pd and PdO standards b) The black curve is the current measured and the blue curve is the fluorescence signal from the electrode interface in a KOH 2 M solution.

The speciation model is in close agreement with the FEXRAV signal. Since the fractional amounts result from the equilibrium computation, their maxima and minima correspond, as expected, to the maxima and minima of the potential ramps. One can notice that the maxima of the FEXRAV occur after (approximately 0–200s) the maxima of the fractional amount of $\text{Pd}(\text{OH})_4^{2-}$ in the catalytic layer. In the same way, the minima of the FEXRAV occur after (approximately 1000–1400s) the maxima of the fractional amount for Pd. This pattern is constantly reproduced for all the performed voltammetric cycles.

Figure 5 depicts the comparison between the results of a FEXRAV experiment (KOH 2 M and EtOH 2 M) solution with the speciation calculations for a KOH 2 M. Again, a good agreement between experimental data and the speciation model is achieved for all the voltammetric cycles. If compared to Figure 4, the main difference is the shape of the oscillations. For the solution of KOH and ethanol, the oscillation amplitude appears wider than with a solution of KOH only. Regarding the general trend of decreasing intensity observed in the FEXRAV of the half-cell filled with KOH, an almost linear decrease is observed also in the case of KOH and ethanol, but it is limited up to the 4th voltammetric cycle, whereas after the 5th cycle a pseudo steady state is established. Interestingly, the ethanol in the electrolyte seems to make the maxima (or minima) of the FEXRAV signal occurring before the maxima (or minima) of the fractional amount for $\text{Pd}(\text{OH})_4^{2-}$ along all the voltammetric cycles. This trend is clearly opposite to what observed in Figure 4.

Discussion

The Pourbaix diagrams of Figure 2, used to model the chemical speciation of the Pd-O-H, reveal an excellent agreement with the literature. No differences between the present and the latest published stability fields^{21,24} are observed. The only small difference was found in the comparison with the Pourbaix et al. findings,²⁵ who couldn't take in account the chemistry of hydroxypalladiates at the time. In their paper, these authors reported the diagrams with the hypothetical predominance of PdO_2^{2-} ions where we find the predominance of $\text{Pd}(\text{OH})_4^{2-}$. As discussed by Pourbaix et al. themselves, the confirmation of their hypothesis was impaired by the lack of a thorough thermochemical characterization of hydroxypalladiates. However, the predominance of $\text{Pd}(\text{OH})_4^{2-}$ was firstly predicted by Mountain and Wood²¹ exploiting the thermochemical characterization published by Chandrasekharan in 1974.²⁶ The latter was not accounted before 1988 when Mountain and Wood²¹ applied the mass balance method to de-

scribe hydrothermal processes involving Pd species. An almost perfect agreement occurs between the present and Mountain and Wood's²¹ charts. It is our opinion that the reproducibility of the literature's predominance charts by our approach enables its use as a tool to predict the evolution of chemical speciation in the Pd-O-H system during a voltammetric scan. Following the Mountain and Wood's calculation, the role played by the $\text{Pd}(\text{OH})_4^{2-}$ species appears crucial for the interpretation of FEXRAV data.

Regarding the comparison between simulated and experimental FEXRAV data, the first part of this discussion is focused on the analysis of the chosen electrochemical and spectroscopic operating conditions. These conditions were, in fact, dictated by a mediation between the requirements of both voltammetry and XAS spectroscopy. At least two main choices are relevant:

- 1) The choice of monitoring FEXRAV through the Fluorescence detector is due to the sampling depth of the relative signal. At 24370 eV, the attenuation length of X-rays in the catalytic layer is estimated around 10 μm (i.e. smaller than the layer thickness).^{5,27} Hence, the signal received by the Fluorescence detector is relative only to the catalytic layer.
- 2) The very low scan rate (1 mV/s) was aimed at improving the sampling time and to achieve the best possible signal-to-noise ratio (SNR) in the Fluorescence detector. As a side consequence, at this rate the system approaches the Nernstian equilibrium. Thus, the results of our thermochemical description based on the mass balance method (i.e. at the thermodynamic equilibrium) can provide an appropriate description of the chemical environment at the electrode interface. This reflects the excellent agreement we found between the FEXRAV measurements and the calculated chemical speciation of Pd.

According to the recent literature, the spectral feature at 24370 eV, although being chosen in the present study from the comparison of Pd and PdO XANES spectra, is not specifically diagnostic for PdO, and can be safely used to assess only the generic oxidation of Pd to Pd(II).^{28–31} In fact, the XANES signals are mostly sensitive to the oxidation state of an element, and less sensitive to its local coordination and structure.¹² Hence, from the spectroscopic point of view, PdO and $\text{Pd}(\text{OH})_4^{2-}$ cannot be easily discriminated, whereas the redox change from Pd to Pd(II) can be easily monitored, even using a single fixed energy of 24370 eV (Fig. 3a).

The comparison between the trend of the current and FEXRAV as a function of the potential in the Figure 3b qualitatively suggests that Pd undergoes the same oxidation process reported in References 28–31

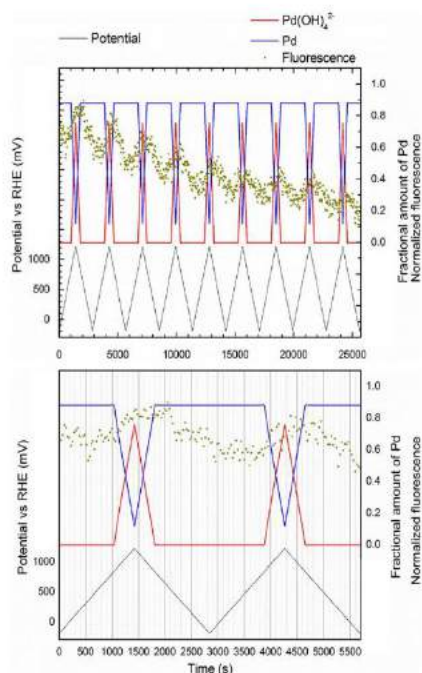


Figure 4. Experimental FEXRAV signal and calculated fractional amount of the relevant species, Pd and $\text{Pd}(\text{OH})_4^{2-}$, during a potential scan rate of 1 mV/s. The electrochemical cell was mounted in the three electrode scheme, and filled with a KOH 2 M solution. FEXRAV signal was detected through the Fluorescence detector. (a) is the overview of the entire voltammetric scan (b) is a closeup of the first two cycles.

However, these works are related to catalytic processes completely different with respect to the oxidation process, observed in the anodic half-cell of a DAFC. Hence, although we expect the oxidation of Pd to $\text{Pd}(\text{II})$, we cannot safely confirm that the increase of the FEXRAV intensity in Figure 3b is linked to this phenomenon without a speciation model. The calculated speciation as a function of time (Fig. 4) allowed to conclusively state that the relevant species are Pd and $\text{Pd}(\text{OH})_4^{2-}$ and that the fractional amount of PdO is negligible. Indeed, the oscillatory increase of FEXRAV, when applied potential values approach 1000 mV vs RHE, is explained in terms of a temporary predominance of the oxidized $\text{Pd}(\text{OH})_4^{2-}$ species over the reduced Pd species.

The explanation of the general decreasing trend, observed in the full experiment with KOH (Fig. 4) and only partially in the experiment with KOH and EtOH (Fig. 5) deserves a further discussion. Since the $\text{Pd}(\text{OH})_4^{2-}$ is soluble, the total amount of Pd in the catalytic layer progressively decreases due to the diffusion process. To approximately quantify the effect of the diffusion, we should consider that roughly a quarter of the total time of the voltammetric scan ($t \approx 700$ s) is spent under diffusion limited condition. In addition, the diffusion coefficient for $\text{Pd}(\text{OH})_4^{2-}$ is assumed to be $D = 6.14 \cdot 10^{-8} \text{ m}^2/\text{s}$.^{33,34} On this basis, the thickness of the diffusion layer is 13 μm ($\delta = \sqrt{4Dt}$).³⁵

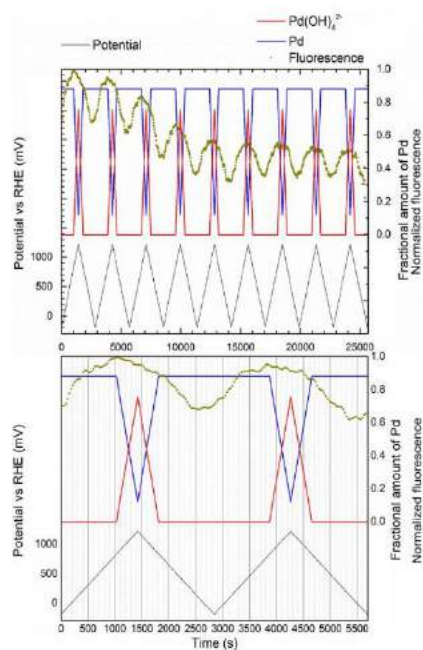


Figure 5. Experimental FEXRAV signal and calculated fractional amount of the relevant species, Pd and $\text{Pd}(\text{OH})_4^{2-}$, during a potential scan rate of 1 mV/s. The electrochemical cell was mounted in the three electrode scheme, and filled with a KOH 2 M and EtOH 2 M solution. FEXRAV signal was detected through the Fluorescence detector. (a) is the overview of the entire voltammetric scan (b) is a closeup of the first two cycles.

Thus, both the thickness of the catalytic layer (roughly 100 μm) and the sampling depth for Fluorescence (roughly 10 μm) signal are negligible if compared to the thickness of the diffusion layer. Therefore, the increasing of the diffusion layer thickness over time, depletes the total Pd content from the catalytic layer (hence also the sampling volume), resulting in a net and progressive decrease of the average FEXRAV signal revealed by the Fluorescence detector. These results are in line with the considerations provided by the review study of Giden.³ Two main differences between the experimental data for the KOH 2 M solution (Figure 4) and the KOH 2 M + EtOH 2 M solution (Figure 5) where revealed:

- 1) the fluorescence peaks for the KOH 2 M occur after the correspondent peaks in the speciation model (after the inversion of the potential), whereas the peaks KOH 2 M + EtOH 2 M solution occur before the calculated peaks (before the inversion of the potential);
- 2) the decrease of the averaged fluorescence signal is linear for KOH 2 M solution while it stops after the 4th cycle for the KOH 2 M + EtOH 2 M solution.

These discrepancies are probably related to mechanistic and kinetics differences between the process occurring in the two electrolytes, and deserve further investigations, still in progress.

Conclusions

In this paper we present a modelling procedure of the chemical speciation (namely the mass balance method) which proved to be very useful in the interpretation of the results recorded by means of a new application of the FEXRAV technique.

Basically, we have shown that while experimental FEXRAV data registered through the Fluorescence detector can easily correlate with the potential applied to a Pd-bearing catalytic layer, an attribution of the changes in the chemistry responsible of the changes in the FEXRAV signal cannot be appropriately reached. The proposed numerical modelling approach clearly points out a chemical speciation dependent on the applied potential where changes of the relative amounts of Pd and Pd(II) are responsible for the change of FEXRAV intensity during the voltammetric scan. Moreover, we were able to identify the main Pd(II) species involved in the process was identified as $\text{Pd}(\text{OH})_2^{2-}$. On this ground, our study was able to confirm the prevalence, under the operative conditions, of the electrodisolution processes of Pd over the formation of the oxide layer.

It is opinion of the authors that this approach is of general interest in helping the analysis of data coming from spectroscopic techniques used to detect speciation features, in particular when working near equilibrium.

Acknowledgments

The authors warmly acknowledge Carlo Bartoli (ICCOM-CNR) for his technical assistance in the realization of the Electrochemical cell, as well as Dr. Alessandro Puri and Dr. Giovanni Ornzio Lepore (IOM-CNR), for their contribution in the adaptation of the cell to the experimental set up of the BM08 LISA beamline. Their high skills and their motivation were fundamental to the success of the experimental part of this study. Dr. Claudio Zaffaroni is also acknowledged for having supported the initial stages of this study. XAS data were performed at the BM08 "LISA" beamline (ESRF, Grenoble, France) during the MA-2153, 08-01-996, MA-2936 and MA-3173 experimental beam-times. ESRF is gratefully acknowledged for provision of synchrotron radiation and for provision of the technical infrastructure. FDB and

MI benefited for departmental funding (ex 60%). Gabrielli Technology and Bluclad srl are acknowledged for contributing to fund this study, as well as is acknowledged the Italian CNR, for support.

References

1. European Commission, *Critical Raw Materials for the EU*, (2010).
2. V. Raghavani et al., *ChemSusChem*, **5**, 1266 (2012).
3. C. Bianchini and P. K. Shen, *Chem. Rev.*, **109**(9), 4183 (2009).
4. L. Wang et al., *Electrochim. Acta*, **177**, 100 (2015).
5. M. Grdelt, M. Łukaszewski, G. Jerkiewicz, and A. Czerwinski, *Electrochim. Acta*, **53**, 7585 (2008).
6. A. Livauchi, H. Miller, and F. Vizza, *Nanotechnology in Electrocatalysis for Energy*, **115**, (2013).
7. F. Zaza, *Chem. Soc. Rev.*, **43**, 7624 (2014).
8. B. L. Meier, S. D. Ebbesen, and L. Leffers, *Chem. Soc. Rev.*, **39**, 4643 (2010).
9. S. Campisi et al., *J. Phys. Chem. C*, **120**, 14027 (2016).
10. L. Wang et al., *J. Power Sources*, **195**, 8036 (2010).
11. A. Minguzzi et al., *Anal. Chem.*, **85**, 7009 (2013).
12. D. G. Montegrossi, D. A. Giachnerini, D. F. Di Benedetto, D. W. Giurlani, and D. A. Livauchi, in *MSE*, (2016).
13. E. Achilli et al., *Journal of Spectroscopy*, **2014**, 2014 (2014).
14. A. Balena et al., *Nut. Neurosci. Lett. Struct. Neurosci.*, **19**, 14 (2014).
15. P. K. Shen and C. Xu, *Electrochim. Commun.*, **8**, 184 (2006).
16. C. Xu, P. K. Shen, and Y. Lin, *J. Power Sources*, **164**, 527 (2007).
17. B. D. L. Parkhurst and C. A. J. Appelo, *Exch. Organ. Behav. Teach. J.*, **D**, 326 (1999).
18. H. C. Helgeson, J. M. Delany, H. W. Nesbitt, and D. K. Bird, *Am. J. Sci.*, **278**-A (1978).
19. J. W. Johnson, E. H. Oelkers, and H. C. Helgeson, *Computers & Geosciences*, **18**(7), 809 (1992).
20. J. W. Ball and D. K. Nordstrom, *U.S. Geol. Surv. Water-Resources Invest. Rep.*, **91-183**, 1 (1991).
21. B. Mountain and S. A. Wood, *Economic Geology*, **83**(3), 492 (1988).
22. H. Huang, *Metals*, **6** (3), 23 (2016).
23. A. Giachnerini, G. Montegrossi, and F. Di Benedetto, *Minerals*, **6**, 79 (2016).
24. N. Takeno, *Natl. Inst. Adv. Ind. Sci. Technol. Tokyo*, **285** (2005).
25. M. J. N. Pourbaix, J. Van Muylder, and N. de Zoubov, *Platin. Met. Rev.*, **3**, 47 (1959).
26. M. Chandrasekharan, M. R. Udupa, and G. Aravamudan, *Press. Pergamon Britain, Gi. Discuss. Exp.*, **36**, 1417 (1974).
27. B. L. Henke, E. M. Gullikson, and J. C. Davis, *At. Data Nucl. Data Tables*, **54**, 181 (1993).
28. J. B. Brazier et al., *Catal. Struct. React.*, **3**, 54 (2017).
29. D. Koziej et al., *Phys. Chem. Chem. Phys.*, **11**, 8620 (2009).
30. G. L. Chiarello and D. Ferri, *Phys. Chem. Chem. Phys.*, **17**, 10579 (2015).
31. J. Nilsson et al., *ACS Catal.*, **5**, 2481 (2015).
32. M. Newville, *Rev. Mineral. Geochemistry*, **78**, 33 (2014).
33. W. P. Griffith, S. D. Robinson, and K. Swars, *Gmelin Handbook of Inorganic Chemistry - Pd*, (1989).
34. R. Vissers and Y. L. Mogenssen, *Liet. TSR Moksl. Akad. Darbai S.*, **1**, 49 (1966).
35. A. J. Bard et al., *Electrochemical Methods Fundamentals and Applications*, (2000).

6.2 Appendix B: FEXRAV/GIXAS Cell Schematics

Index of the design sheets:

| | |
|----------|----------------------|
| Pag. 110 | Assembly Views |
| Pag. 111 | Bottom Exploded View |
| Pag. 112 | Top Exploded View |
| Pag. 113 | Cell Body |
| Pag. 114 | Cell Head |
| Pag. 115 | Upper Clamp |
| Pag. 116 | Lower Clamp |
| Pag. 117 | Tie-Rods & Pivots |

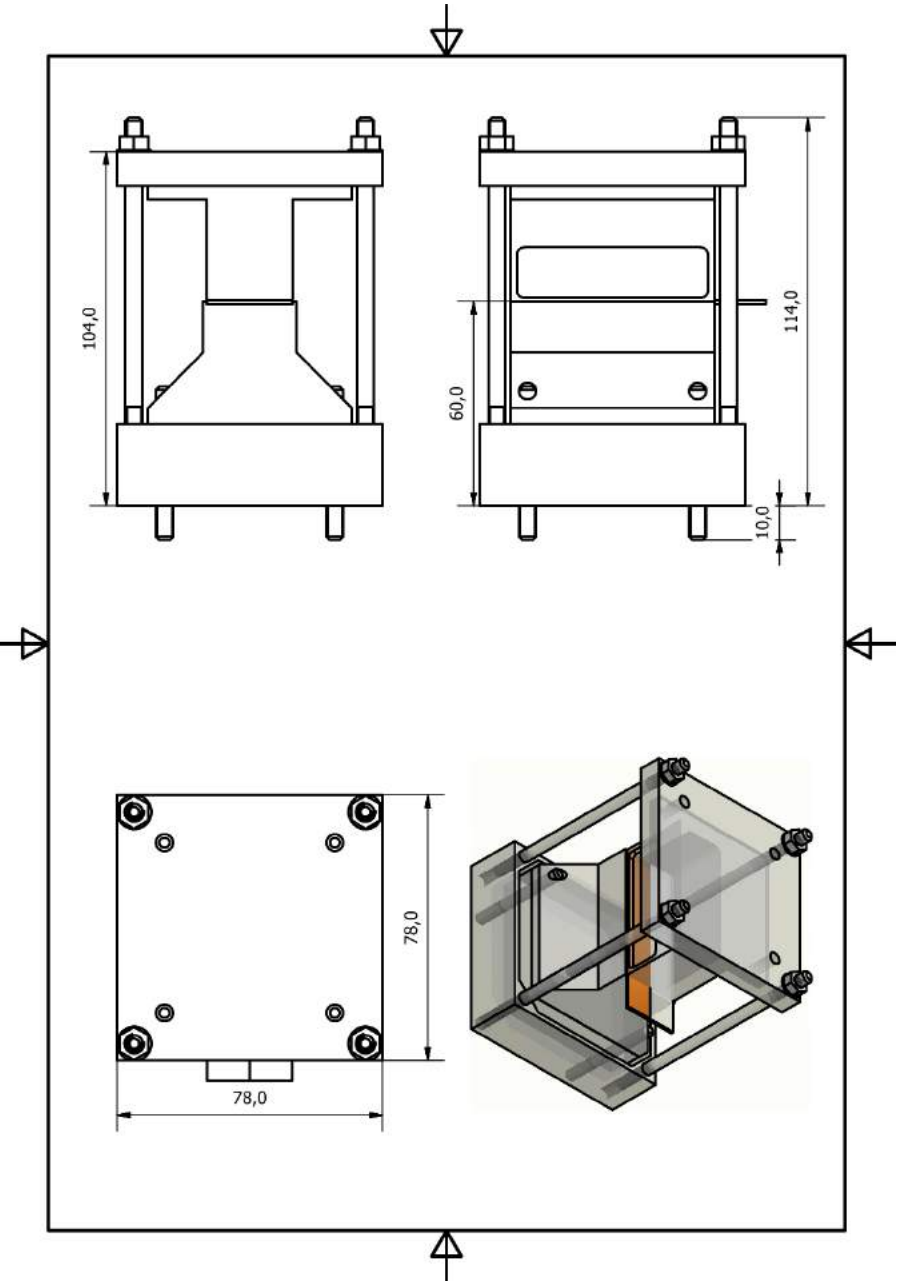


Figure 75 – Assembly views

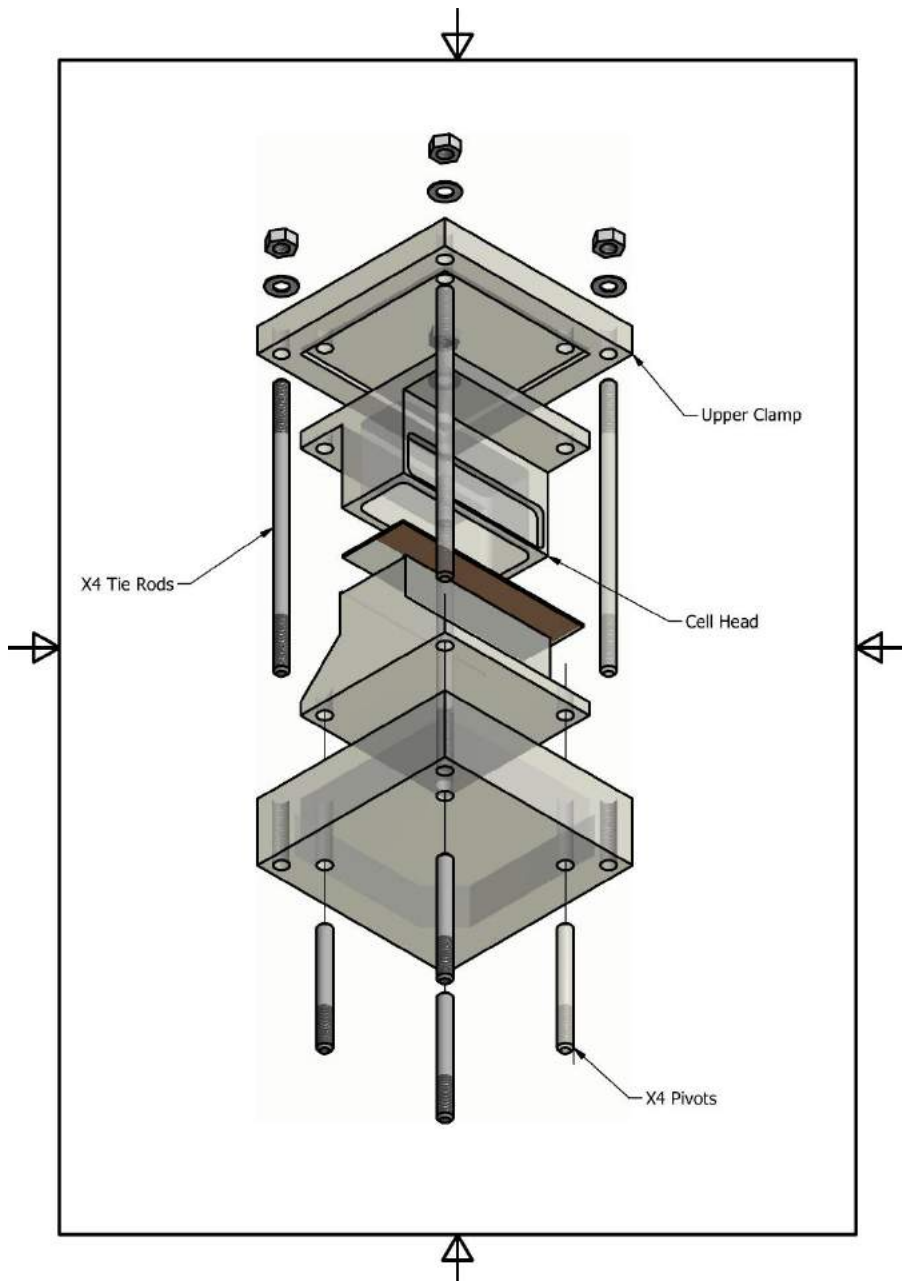


Figure 76 – Bottom exploded view

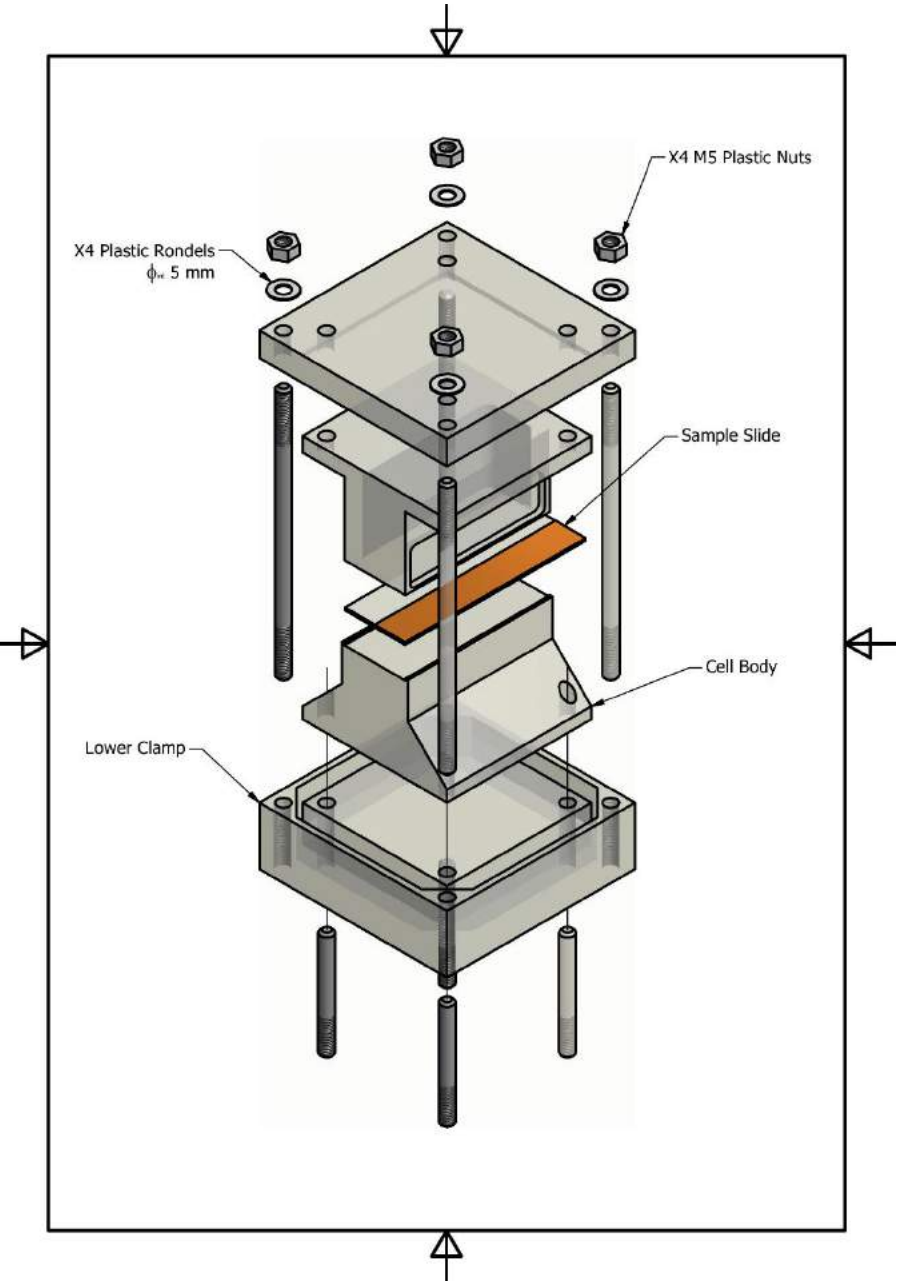


Figure 77 – Top exploded view

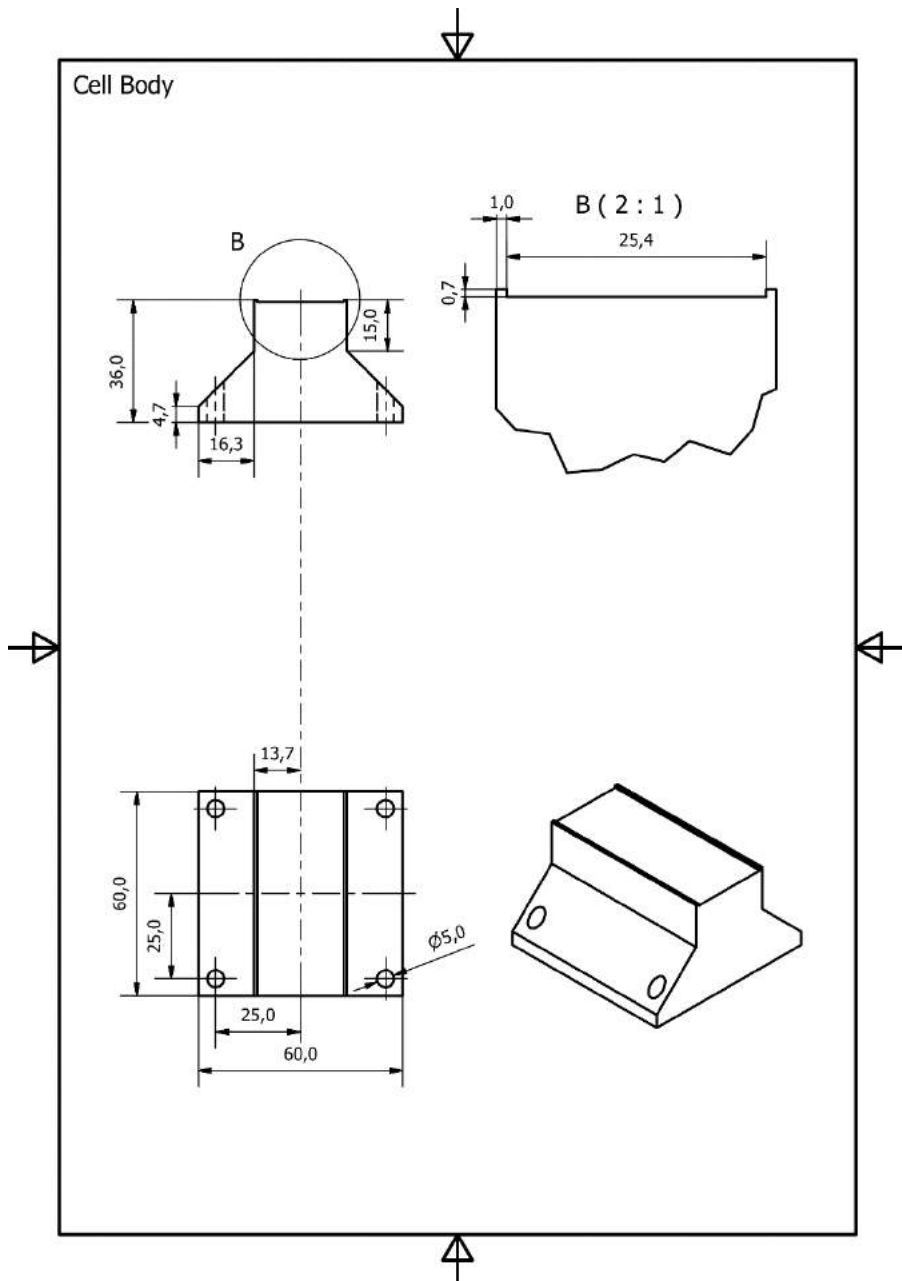


Figure 78 – Cell body

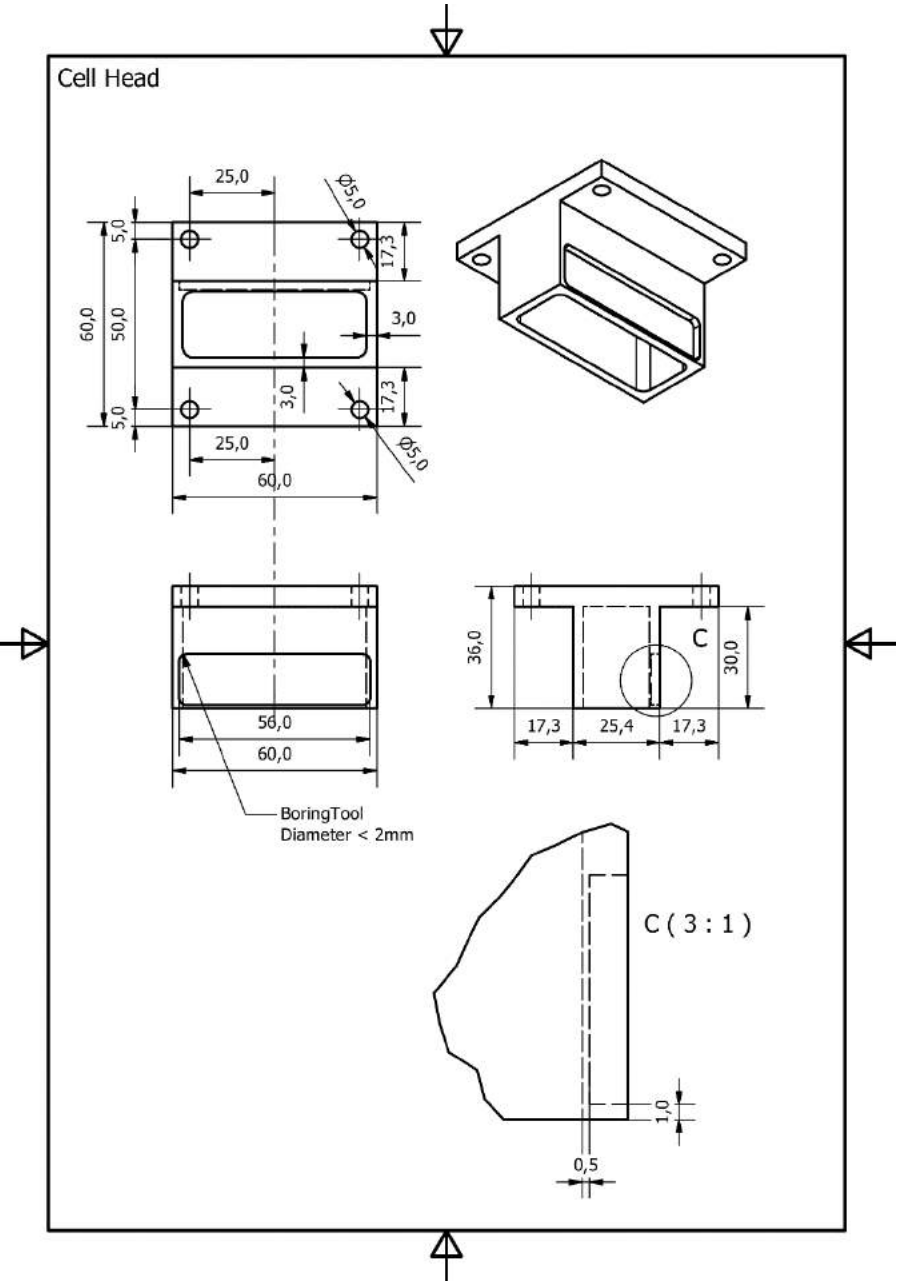


Figure 79 – Cell head

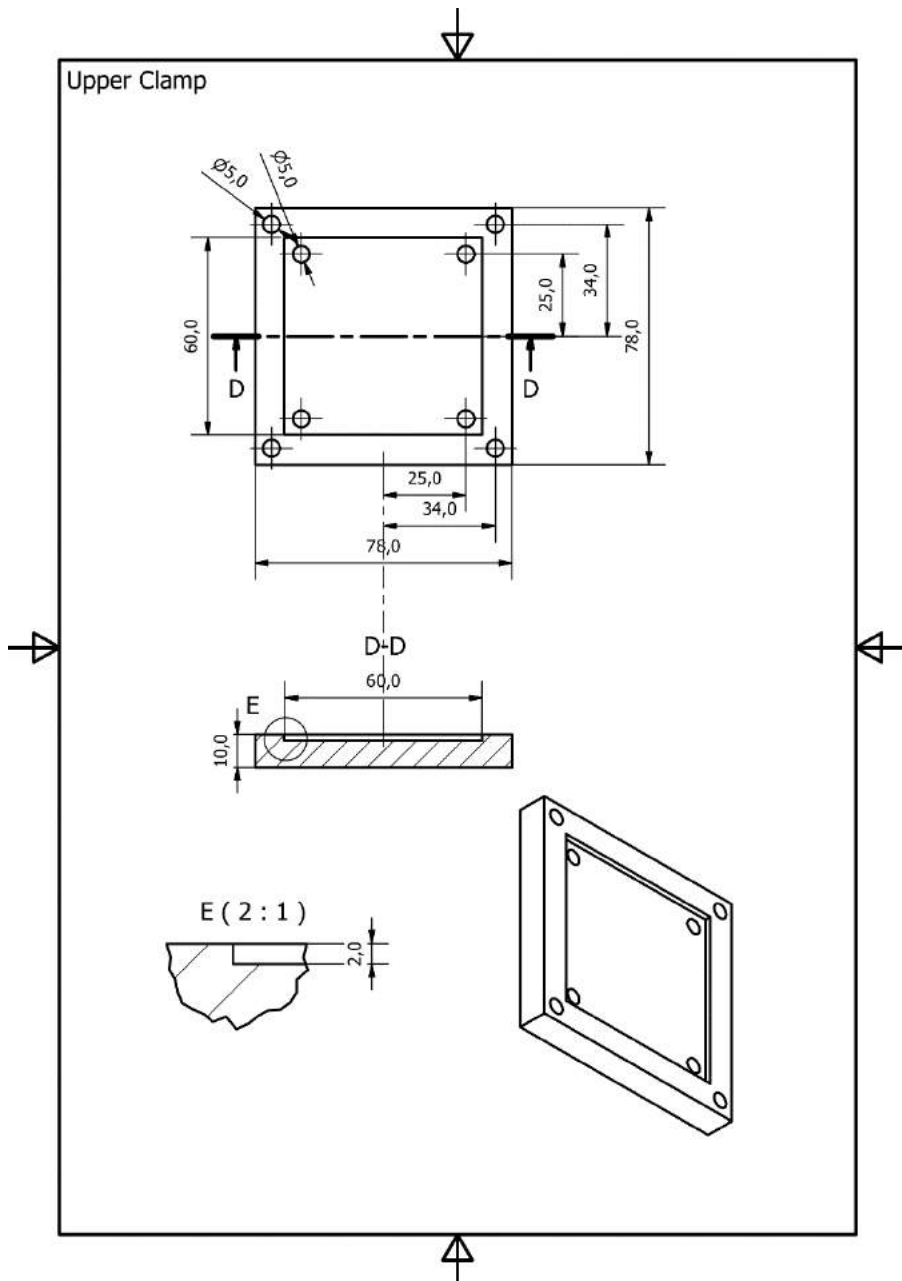


Figure 80 – Upper Clamp

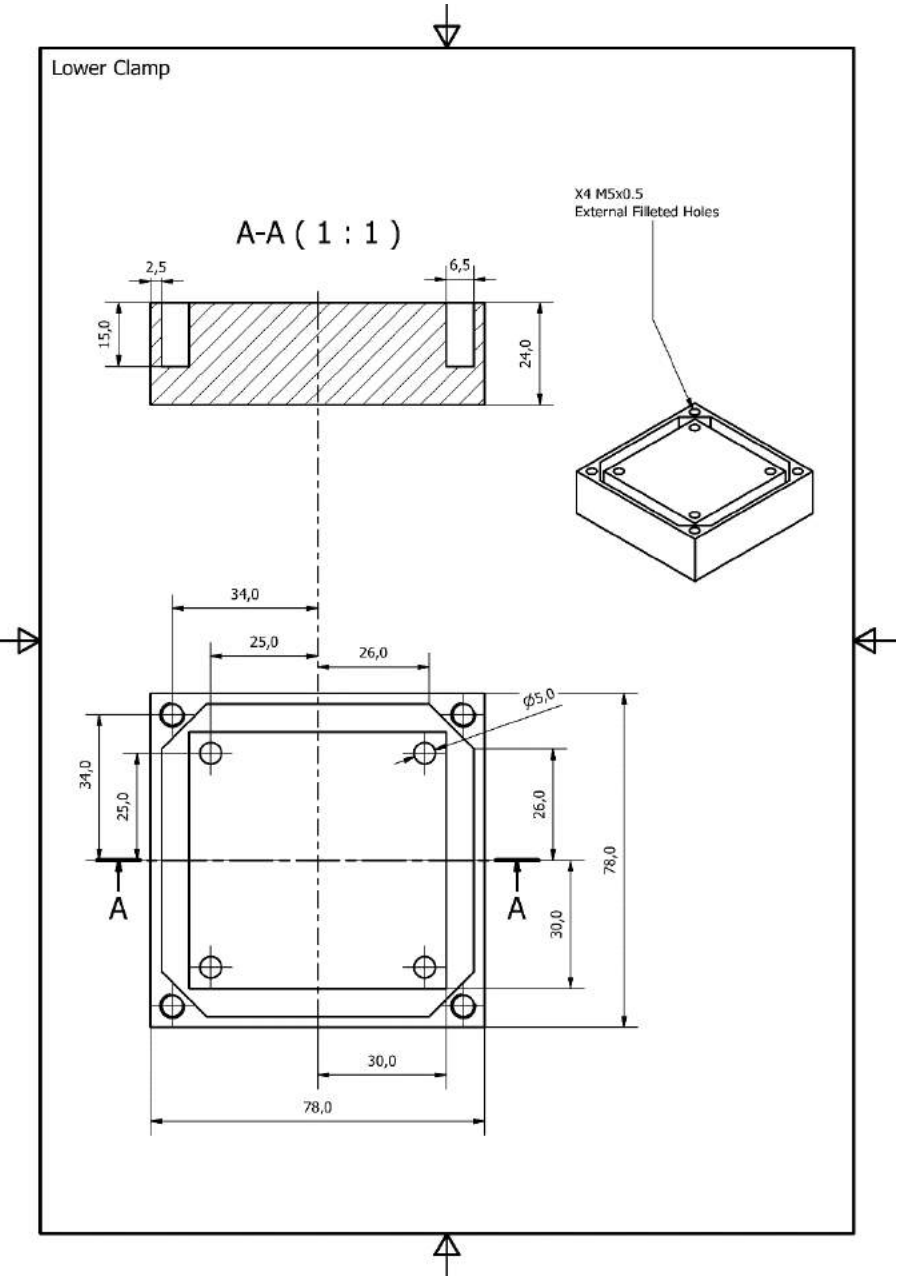


Figure 81 – Lower clamp

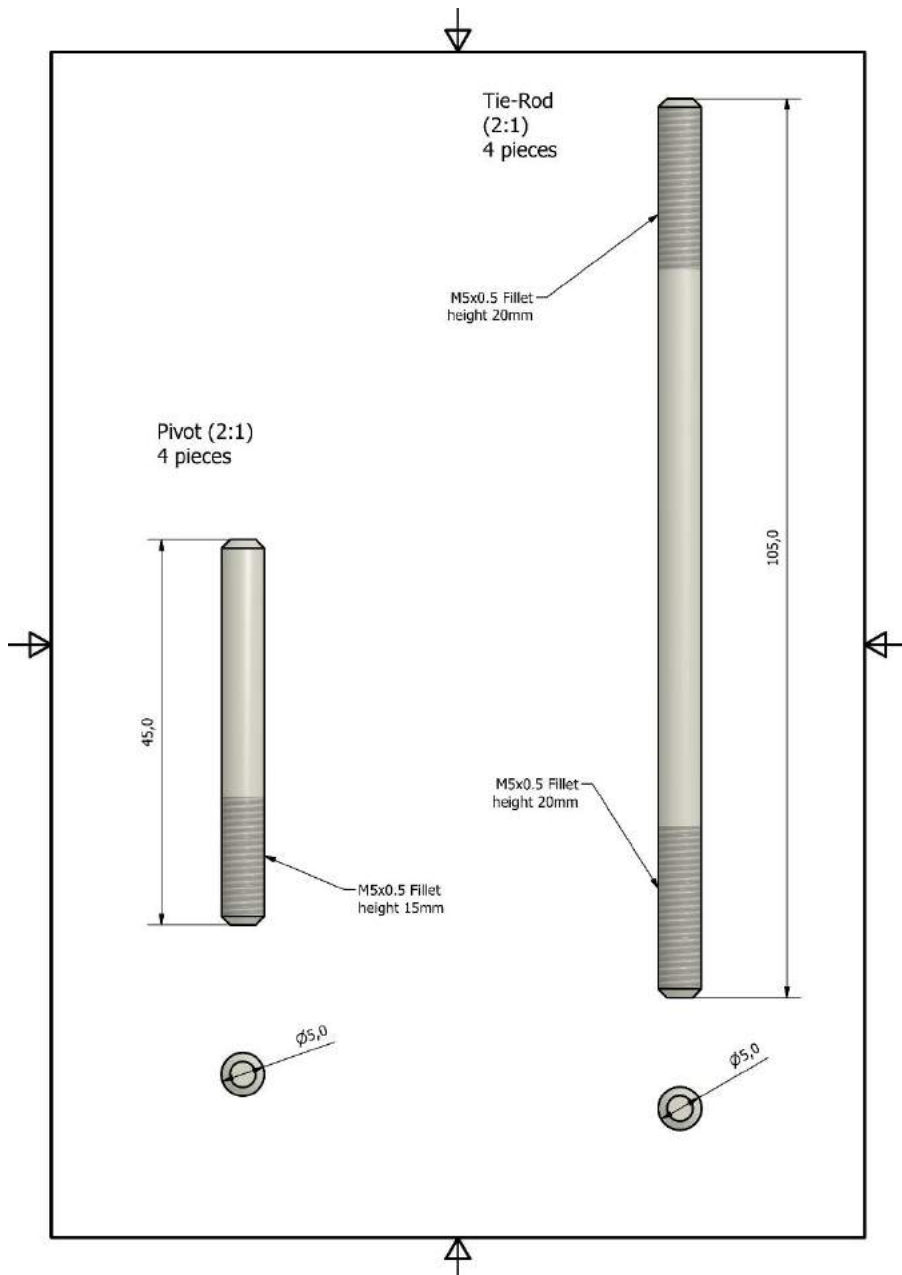


Figure 82 – Tie rods & pivots

6.3 [Appendix C: Article “Aluminium Electrodeposition from
Ionic Liquid: Effect of Deposition Temperature and
Sonication”](#)



Article

Aluminium Electrodeposition from Ionic Liquid: Effect of Deposition Temperature and Sonication [†]

Enrico Berretti ¹, Andrea Giaccherini ¹, Stefano M. Martinuzzi ¹, Massimo Innocenti ¹, Thomas J.S. Schubert ², Frank M. Stiemke ² and Stefano Caporali ^{3,*}

¹ Dipartimento di Chimica, Università di Firenze, Sesto Fiorentino 50019, Italy; enrico.berretti@unifi.it (E.B.); andrea.giaccherini@unifi.it (A.G.); stefano.martinuzzi@unifi.it (S.M.M.); m.innocenti@unifi.it (M.I.)

² IoLiTec Ionic Liquids Technologies GmbH, Heilbronn 74080, Germany; schubert@iolitec.de (T.J.S.S.); stiemke@iolitec.de (F.M.S.)

³ Consorzio Interuniversitario Nazionale Per la Scienza e Tecnologia dei Materiali (INSTM) and Istituto Sistemi Complessi (ISC), Sesto Fiorentino 50019, Italy

* Correspondence: stefano.caporali@unifi.it; Tel.: +39-055-457-3119

[†] This paper is an extended and revised version of the paper published in Sciforum Electronic Conference Series, Proceedings of the 2nd International Electronic Conference Materials, 2–16 May 2016; Volume 2, 2016, C003; doi:10.3390/ecm-2-C003.

Academic Editor: Silvia Gross

Received: 17 June 2016; Accepted: 12 August 2016; Published: 24 August 2016

Abstract: Since their discovery, ionic liquids (ILs) have attracted a wide interest for their potential use as a medium for many chemical processes, in particular electrochemistry. As electrochemical media they allow the electrodeposition of elements that are impossible to reduce in aqueous media. We have investigated the electrodeposition of aluminium from 1-butyl-3-methyl-imidazolium chloride ((Bmim)Cl)/AlCl₃ (40/60 mol %) as concerns the effect of deposition parameters on the quality of the deposits. Thick (20 µm) aluminium coatings were electrodeposited on brass substrates at different temperatures and mixing conditions (mechanical stirring and sonication). These coatings were investigated by means of scanning electron microscope, roughness measurements, and X-ray diffraction to assess the morphology and the phase composition. Finally, electrochemical corrosion tests were carried out with the intent to correlate the deposition parameters to the anti-corrosion properties.

Keywords: ionic liquids; aluminium; electrodeposition; surface morphology; sonication; corrosion resistance; texture

1. Introduction

Since its invention, the Hall-Héroult process [1] has been the conventional process for the production of metallic aluminium. It is based upon the electroreduction of alumina in a cryolite melt by using graphite electrodes. The high temperature required (in the order of 900 °C) and the emission of toxic gaseous by-products, such as fluorine and carbon monoxide, rendered the research for greener and safer alternatives highly attractive [2]. The introduction of Ionic Liquids (ILs) (namely room temperature molten salts) as electrochemical media for the aluminium electrodeposition offered a very promising route to succeed in this goal. Since the first pioneeristic studies in the 1990s [3], a large number of investigations successfully reported the lab-scale electrodeposition of aluminium at room or nearly room temperature. Different types of ionic liquids [4–9] and additives [10,11] were proposed to achieve smooth and thick aluminium coatings. However, with the aim of the industrialization of the Al-plating process, the use of additive-free chloroaluminate ILs, seems to constitute the better compromise between the quality of the deposit and the durability of the electroplating bath. Beside the handling difficulties, mainly due to the vigorous reaction with atmospheric moisture, their high

aluminium content, reduced viscosity, and remarkable electrochemical stability allow for a high deposition rate, in the order of $10 \mu\text{m}\cdot\text{h}^{-1}$, and a long working time without the need to replenish chemicals. The scheme of the Al-electroplating process is depicted in Figure 1.

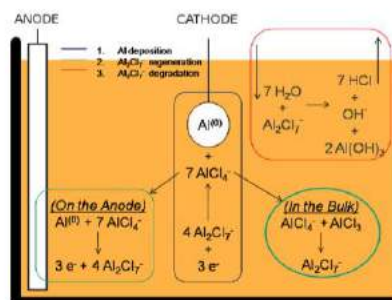


Figure 1. Scheme of the Al-electroplating process from chloroaluminated ionic liquids (ILs). Al is reduced at the cathode while at the anode the electroactive species is regenerated by aluminium dissolution and reaction with AlCl_4^- . The red box depicts the parasite reaction with moisture.

The Al-coatings obtained at lab scale by means of this technology were successfully employed as protective layers for structural materials such as carbon steel [10–12], magnesium alloys [13], and light weight alloys [14], just to name a few. The anticorrosion properties of the Al-coatings are based upon the formation of a dense passivation layer composed by aluminium oxide that prevents further corrosive action towards the metal beneath. Therefore, the anticorrosion ability requires the formation of a homogeneous, crack-free alumina layer.

In order to obtain high quality Al-coatings, the study of the effect of deposition parameters such as temperature and mixing conditions on the deposition rate, the crystalline structure, the surface morphology, and roughness is, therefore, mandatory. Electrodeposition in stirred solution has the advantage of reducing the thickness of the diffusion layer, thereby improving the deposition rate and the homogeneity of the deposit. However, even though some studies investigated the effect of temperature [12,15,16], very little work was reported on the effect of solution stirring [17,18] and, to the best of our knowledge, no one has addressed the effect of sonication so far.

For these reasons, with an aim to determine the better operative conditions for the industrialization of the Al-plating process, we investigated the effects of temperature and mixing conditions, both alone and combined, on the electrodeposition of Al from the ionic liquid (Bmim)Cl/ AlCl_3 (40/60 mol %). Finally, the deposits were characterized by scanning electron microscopy (SEM) investigation, roughness measurement, X-ray diffraction, and electrochemical corrosion tests to assess the conditions more suited to achieving smooth, homogeneous, and thick aluminium coatings.

2. Materials and Methods

2.1. Chemicals

The electroplating bath was constituted by 1-butyl-3-methyl-imidazolium chloride ((Bmim)Cl)/ AlCl_3 (40/60 mol %). It was supplied by IoLiTec Ionic Liquids Technologies GmbH (Heilbronn, Germany) and used as received without further purification.

2.2. Electrode Materials

12 mm diameter brass (Cu 63%, Zn 37%) tokens were employed for the study of temperature and mixing effect. Larger tokens (25 mm diameter) were used to study the combined effects. The tokens were grinded with SiC paper down to 1200 grit and polished with diamond suspension (Metadi 3 micron, Buehler, Uzwil, Switzerland), rinsed with tap water and sonicated in acetone (technical grade, VWR Chemicals, Leuven, Belgium) for 5 min. Before the electrodeposition they were rinsed again in tap water and soaked in HCl 1 M for 3 min, rinsed in distilled water, sonicated in acetone for 5 min and then dried under N_2 . Inside the nitrogen filled glove box, prior to the start of electrodeposition, the working electrodes were electrochemically cleaned in the electroplating bath by applying a positive (oxidative) current ($2.5 \text{ mA}\cdot\text{cm}^{-2}$) for 30 s.

2.3. Deposition Parameters

The plating process was carried out inside a nitrogen filled glove box (Itenco mod 10A, Castelvoglia, Italy), with water content below 20 ppm. The deposits were produced in current controlled (galvanostatic) conditions at $10 \text{ mA}\cdot\text{cm}^{-2}$ using a potentiostat (Model 7050 by Amel s.r.l., Milan, Italy), a circular anode constituted by a pure aluminium foil (Goodfellow, Huntingdon, UK, 99.0%) and brass tokens as cathodes. No reference electrode was used in this study, since the galvanostatic method requires only the control of the charge. The obtained potential vs. time curves refer to the absolute potential difference applied to the electrodes. Two different deposition set-ups were used with the same geometry but different anode/cathode surface ratio (see Figure 2a,b). Depositions were performed in quiet (no motion) or under mixing conditions by means of mechanical stirring (magnetic bar, 320 rpm) or sonication (Qsonica Sonicator Q500, Newtown, CT, USA, 500 W 20 kHz operating at 30% of maximum power). In the sonication experiments, the horn was placed on the cathode side as depicted in Figure 2b.

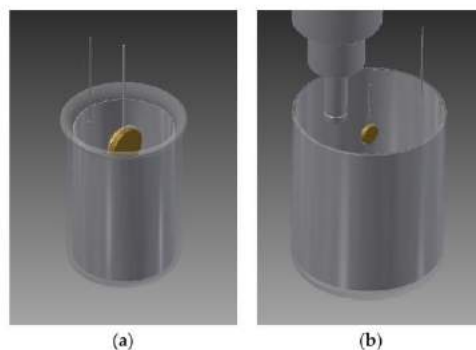


Figure 2. Scheme of experimental set-ups used for temperature (a) and sonication (b) experiments.

2.4. Characterization of the Deposits

The morphology of the coatings was investigated by Scanning Electron Microscopy (S-2300, Hitachi, Tokyo, Japan) operating at 20 kV, while the average roughness was measured using a Hommel Tester W55 (Teplce, Czech Republic). The roughness measurements were obtained carrying out five different and independent tests in randomly chosen areas of the sample scanning 4.8 mm of surface at $0.2 \text{ mm}\cdot\text{s}^{-1}$ of scan rate. The parameters employed were $\lambda_c = 0.8 \text{ mm}$ and $\lambda_c/\lambda_s = 300$ using a filter ISO 11562(MI). Different roughness parameters were calculated (see Appendix A) and the obtained values are summarized in Tables 1 and 2.

Table 1. Roughness parameters for the samples obtained at different temperatures and their relative yield.

| Sample | Rt (μm) | Ra | RzISO (μm) | Rz (μm) | Yield (%) |
|-------------|-------------|-----------|------------|------------|-----------|
| Temp. 50 °C | 32.9 ± 1.2 | 3.7 ± 1.1 | 25.5 ± 4.1 | 23.3 ± 2.8 | 79 |
| Temp. 70 °C | 21.7 ± 10.5 | 2.1 ± 0.2 | 14.9 ± 5.8 | 13.4 ± 4.8 | 86 |
| Temp. 90 °C | 4.2 ± 0.1 | 0.3 ± 0.1 | 3.1 ± 0.1 | 2.90 ± 0.1 | 88 |

Table 2. Roughness parameters for the samples obtained with different agitation modes and their relative yield.

| Sample | Rt (μm) | Ra | RzISO (μm) | Rz (μm) | Yield (%) |
|--------------------|------------|-----------|------------|------------|-----------|
| Quiet deposit | 4.2 ± 0.3 | 0.4 ± 0.1 | 3.6 ± 0.2 | 3.4 ± 0.2 | 60 |
| Sonication 1 to 10 | 11.7 ± 1.3 | 0.7 ± 0.1 | 8.5 ± 0.8 | 7.2 ± 0.6 | 100 |
| Sonication 1 to 1 | 17.0 ± 1.2 | 1.7 ± 0.1 | 13.6 ± 0.6 | 12.7 ± 0.4 | 100 |

2.5. Process Yield

Since the IL viscosity is much larger with respect to the aqueous solutions (thus limiting the mass transport of the electroactive species), the formation of dendritic deposits is favoured, especially when mild operative conditions (low temperature, no mixing) and high current densities are employed. If dendritic coatings are formed, the detachment of parts of the deposit during the rinsing operations cannot be neglected. To take into account this mass loss, process yield was calculated as the percent ratio between the effective mass of the obtained deposit and the theoretical mass calculated from the Faraday law (Equation (1)).

$$Yield = \frac{weightedMass}{theoreticalMass} \times 100 \quad (1)$$

From the potentials reached in our experiments, there is no evidence that parasitic reactions can lower the cathodic efficiency of the deposition below a 100% yield. Therefore, considering the aluminium layer homogeneously distributed, the yield provides information about the thickness of the deposit.

2.6. XRD Analysis

The phase determination of the coatings was carried out through X-ray diffraction (XRD), performed using a XRD Bruker D8 Advance powder diffractometer (Bruker AXS GmbH, Karlsruhe, Germany) employing Cu Kα (1.54187 Å) radiation in the 2θ range 36°–80°, applying a step size of 0.022° 2θ and a step counting time of 0.27 s. XRD spectra deconvolution was performed by means of the single line profile analysis [19], involving the fitting of the peaks with two Voigt functions (one for the K_{α1} and for K_{α2}). We are aware that for the complete assessment of the strain and size of the crystallites the Warren-Averbach method had to be used. However, the accurate assessment of these parameters requires tens of independent peaks and it is beyond the aim of this work. Still, the use of Voigt functions (convolution of Lorentzian and Gaussian functions) allows us to assess the average strain of the crystallites, related to the Gaussian width, and the crystallite size, related to the Lorentzian width, in a simple and reliable way as shown by several authors [19–21]. In such a way, information on the effect of the experimental conditions on the strain and size of the crystals as well as the texture coefficient were determined. The texture coefficient $T(hkl)$ for the (hkl) plane is defined in Equation (2):

$$T(hkl) = \frac{A(hkl) / A_0(hkl)}{\sum_{hkl} A(hkl) / A_0(hkl)} \quad (2)$$

where $A(hkl)$ is the experimental area under the Voigt curve of the (hkl) plane and $A_0(hkl)$ is the respective theoretical area simulated by using the program Mercury and Wyckoff structural parameters [22–24].

2.7. Electrochemical Corrosion Test

The electrochemical corrosion tests were performed using a corrosion cell from Princeton Applied Research (Flat cell KO235, Oak Ridge, TN, USA) in aerated 3.5% NaCl (>99.5% from Merck, Darmstadt, Germany) solution at room temperature (20–23 °C). The potentiostat (Princeton Applied Research model 2273, Oak Ridge, TN, USA) was controlled by PowerSuite 2.58 software (Princeton Applied Research, Oak Ridge, TN, USA). The classical three electrode set-up was employed using a platinum grid as counter electrode and a standard calomel electrode (SCE) reference electrode separated from the solution with an ions conducting glass frit, the working electrode surface was always 1.0 cm². The tests were performed on the aluminized samples without further treatment. Every sample was kept in the saline solution for at least 16 h in order to allow the stabilization of the open circuit potential (OCP); then, potentiodynamic (PD) experiments were recorded starting from −0.250 V with respect to the OCP at the scan rate of 0.4 mV·s^{−1}.

3. Results

3.1. Effect of Temperature

Even though the effect of temperature on the morphology of the Al-coatings has been previously reported for this IL up to 55 °C [14], we extended the investigation at higher temperatures. In this set of experiments, while maintaining quiet the electroplating bath, the Al deposition was performed at three different temperatures: 50 °C, 70 °C and 90 °C. During the deposition the potential-time curves (Figure 3) were recorded in order to extrapolate the induction time (the time needed to reach a stable deposition potential) and the equilibrium potential. The last one provides direct insight about the overpotential needed to obtain the Al-reduction and, therefore, the energy consumed.

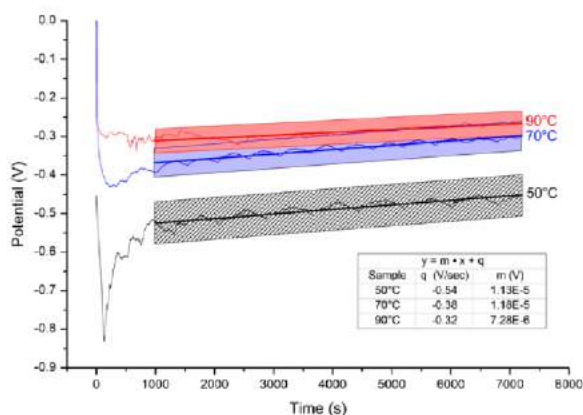


Figure 3. Potential-time curves obtained at different temperatures. Galvanostatic deposition 10 mA cm^{−2}, deposition time 2 h. The inset depicts the results of data linear fitting. The slope of the curves decreases with increasing temperature.

In accordance with previous investigations in similar ionic liquids [14], higher temperature favours the electroreduction process. Increasing temperature reduces the induction time, promotes higher process yield, and requires less negative potentials. It is noteworthy that the curves are characterized by smaller slopes indicating, on the whole, a lower surface increase as a consequence of the formation of smoother deposits. This qualitative observation was supported by more quantitative roughness measurements. The data summarized in Table 1 show that the surface roughness decreased and more homogeneous deposits (lower relative error in the roughness measurement) were obtained as a function of temperature increase.

SEM investigation (Figure 4) strengthen this trend evidencing the change of morphology from pinnacle type deposits at 50 °C to homogeneous crystalline structure at 90 °C.

Unfortunately, repeated experiments demonstrate that for temperatures higher than 70 °C the ILs undergo very rapid degradation. This impairs the use of higher temperatures for industrial and applicative purposes. The recommended maximum temperature can be considered 60 °C. All the following experiments were carried out at temperatures not exceeding 60 °C.

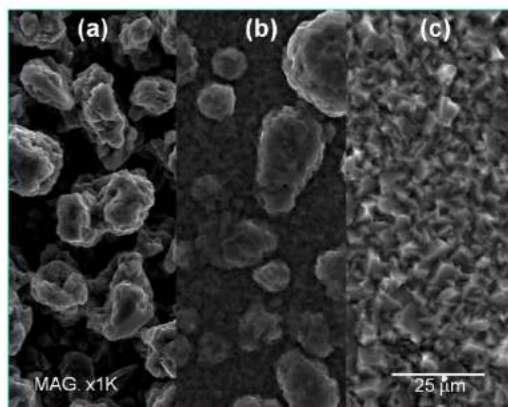


Figure 4. Scanning electron microscopy (SEM) images of the samples obtained at different temperatures: (a) 50 °C; (b) 70 °C; and (c) 90 °C. Deposition time was 2 h.

3.2. Effect of Sonication

By using the larger set-up (Figure 2b) necessary to immerse the sonication horn in the electroplating bath, two series of samples were produced at 20 °C employing different sonication duty cycles. The first one, namely mild sonication, consisted of 1 s on (30% power) for every 10 s off; the second, stronger sonication, consisted in a 1 s on (30% power) for every 1 s off. We refer to these conditions as “Sonication 1 to 10” and “Sonication 1 to 1” respectively. Quiet depositions were also carried out for comparison.

The potential-time curves depicted in Figure 5 show long induction time and the serious effect of sonication on the equilibrium potential; stronger sonication leads to less negative deposition potentials and, in turn, an easier deposition process. On the other side, the roughness measurements summarized in Table 2 depict an opposite trend with respect to the temperature series indicating, on the whole, the increase of surface roughness as a function of sonication. This counter intuitive behaviour is explained by SEM investigation (Figure 6). Even if the nucleation and growth mechanism remain unchanged, increasing the sonication power leads to the formation of larger crystals that account for the increased surface roughness. It is also worth noting that by using sonication a 100% yield is achieved.

On the other hand, the deposit obtained at 20 °C without sonication presents a massive deposit loss (yield about 60%, Table 2). That is reasonably due to the formation of dendrites that were removed during sample rinsing. As a consequence of the reduced thickness, the surface roughness decreases.

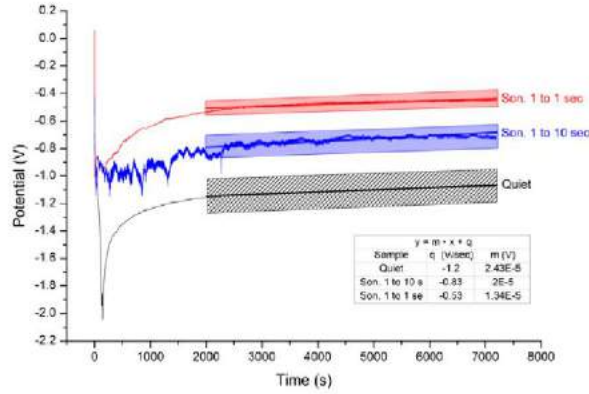


Figure 5. Potential-time curves obtained at different sonication levels. Galvanostatic deposition $10 \text{ mA}\cdot\text{cm}^{-2}$, deposition time 2 h. The inset depicts the results of data linear fitting; shadow areas represent the confidence interval.

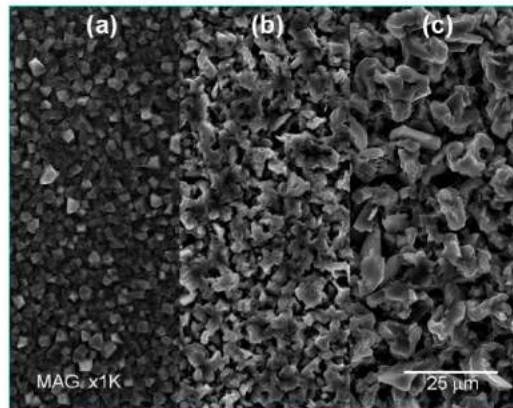


Figure 6. SEM images of the samples obtained using different sonication: (a) Quiet solution; (b) Sonication 1 to 10; and (c) Sonication 1 to 1.

Corrosion Tests

The Al-coatings obtained at different temperatures and mixing conditions were investigated to assess their anticorrosion properties in 3.5% NaCl aerated aqueous solution. Figure 7 shows the potentiodynamic curves relative to the samples obtained at different temperatures (a) and mixing conditions (b). There were no substantial variations among the free corrosion potentials. Only a modest

decrease in the corrosion current (i_c) is detectable in the temperature series. That is reasonably due to the decrease in sample roughness and, therefore, the reduction of the active surface. On the whole, all the curves but one present very similar anodic branches thereby confirming a similar corrosion mechanism. The different curve shape displayed by the sample obtained at room temperature in quiet conditions is reasonably due to the lower thickness, about 12 μm accordingly to a 60% yield, with respect to the 20 μm of a 100% yield (Table 2).

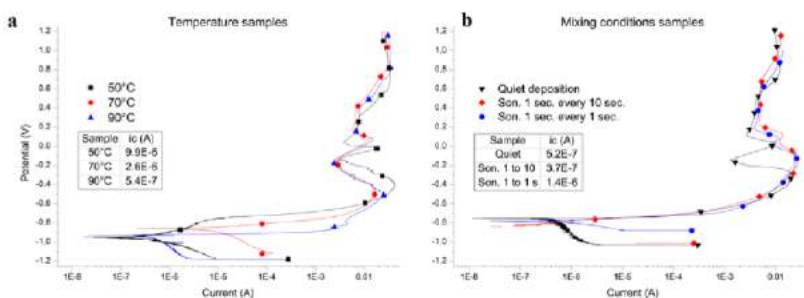


Figure 7. Potentiodynamic curves in 3.5% NaCl aerated aqueous solution on samples obtained at different temperatures (a) and mixing conditions (b). Scan rate 0.4 mV·s⁻¹. The inset depicts the corrosion current values.

3.3. Combined Effects

In order to study the influence of both temperature and sonication, a new set of Al-deposits were obtained. Three temperatures (20 °C, 40 °C, and 60 °C) and three mixing parameters (quiet bath, stirring at 320 RPM, and sonication 1 to 10) were chosen to deposit aluminium on 25 mm diameter disks. Table 3 summarizes the tested combinations, while the electrochemical set-up used is depicted in Figure 2b. The sample at 20 °C in quiet was not studied since it required a very negative potential (close to −4 V), well below the IL cathodic limit.

Table 3. Summary of the samples obtained by means of combined experimental conditions and, within brackets, their relative process yield.

| Yield % | 20 °C | 40 °C | 60 °C |
|--------------------|----------|----------|----------|
| Quiet Deposits | — | A (45%) | B (69%) |
| Stirring 320 RPM | C (82%) | D (100%) | E (100%) |
| Sonication 1 to 10 | F (100%) | G (100%) | H (100%) |

Deposition at high temperature combined with strong sonication duty cycle (30%, 1 to 1) is not of practical interest since the heating effects of sonication cause local temperatures to rise, which leads to quick degradation of the IL. As expected, the yield increases as a function of temperature (samples A and B) and mixing (Table 3).

Roughness and morphological investigation on the Al-deposits are depicted in Figures 8 and 9. A substantial increase of the crystal size of the deposits obtained at higher temperatures accounts for the observed increased roughness.

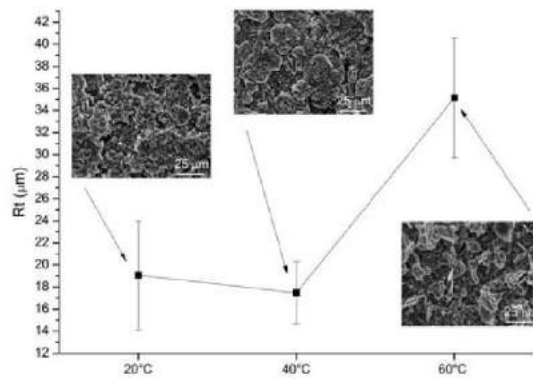


Figure 8. Roughness and SEM micrograph (scale bar is 25 μm) of the samples obtained by mechanical stirring (320 RPM) at different temperatures.

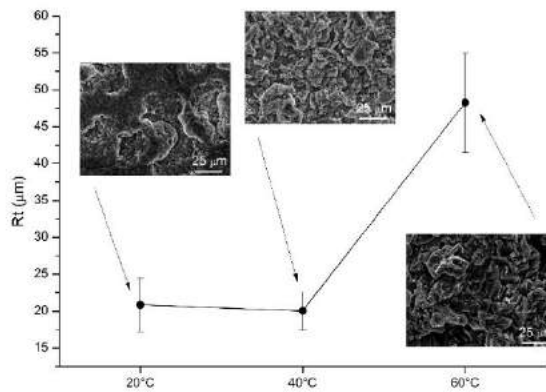


Figure 9. Roughness and SEM micrograph (scale bar is 25 μm) of the samples obtained via sonication (1 to 10 cycle) at different temperatures.

Structural Investigation

The XRD patterns of the Al-coated samples (from A to H) compared with the simulated Al metal pattern are depicted in Figure 10 (PDF 85-1327). The substrate (63% Cu, Zn 37% brass alloy) is an α - β biphasic alloy (Alloy Phase Diagrams, ASM international, page 48), the α -brass pattern is labelled as “Brass” according to the PDF 50-1333 card, while the β -phase pattern (PDF 02-1231) is hindered by the pattern of the Al coating.

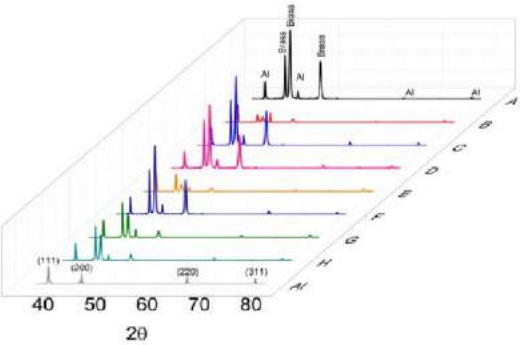


Figure 10. X-ray diffraction (XRD) patterns of the samples (A–H) in Table 3 compared with the simulated powder aluminium pattern (Al).

The diffraction peaks have been fitted with a R^2 always higher than 0.987. Figure 11 depicts the resulting fits of the $K_{\alpha 1}$ and $K_{\alpha 2}$ diffraction peaks for the sample B.

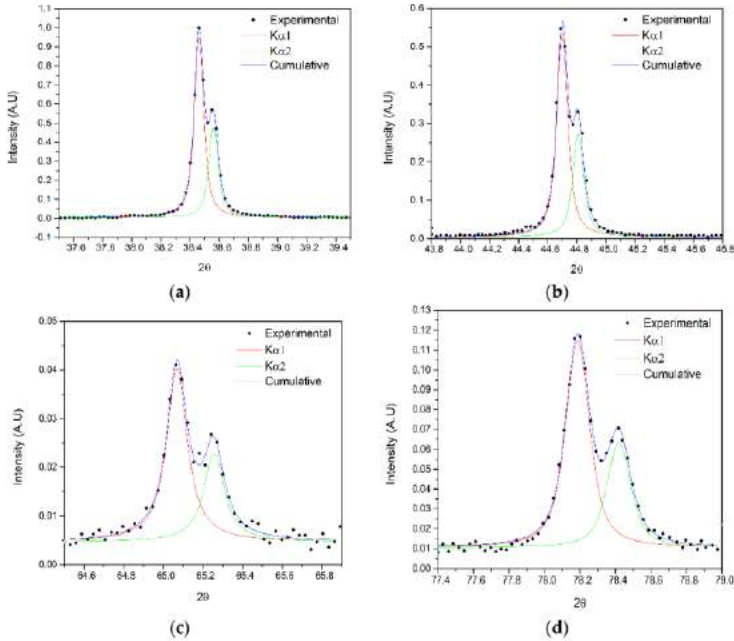


Figure 11. An example of the fitted double Voigt for the sample B: plane (111) (a); (200) (b); (220) (c); and (311) (d).

The texture coefficients obtained from these spectra (Figure 12a) clearly show the effect of deposition parameters on the growth of the deposits. In the samples obtained by using mechanical stirring (samples C to E), the texture along (111) and (311) planes increases as a function of the temperature. On the contrary, texturing of planes (200) and (220) decrease with rising temperatures. Samples obtained by means of sonication (samples F to H) show a similar but less enhanced texturing as a function of the temperature. Moreover, the (220) plane is characterized by a significant increase of texturing for the sample obtained at 60 °C.

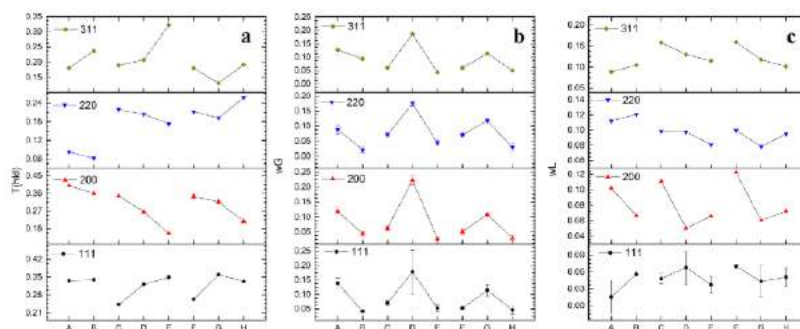


Figure 12. Trends of the fits for the assigned peaks over the three different sets of results: (a) the texture coefficient (no error bars); (b) the Gaussian width (proportional to the average strain); and (c) the Lorentzian width (proportional to the average size of the crystallites). The missing error bars in panels b and c are related to errors smaller than 0.5%.

Figure 12b reports the Gaussian widths of the XRD peaks. These values are considered to be related to the average strain of the crystallites. It is worth noting that for each plane the maximum Gaussian width, hence the maximum lattice strain, was achieved in the deposits obtained at 40 °C. Regarding the Lorentzian width of the peaks, which is inversely related to the average crystal size, the obtained values are depicted in Figure 12c. The average crystallite size presents trends that are more complex with respect to the texture. Generally speaking, improving the mixing conditions does not dramatically affect crystallite size along (111), (200), and (220) planes. In particular, the temperature does not consistently change the size along the zonal axis of the (111) plane. Along the zonal axis corresponding to the (200) and (220) planes, the crystallites size reaches its maximum at 40 °C under sonication. On the other hand, along the zonal axis of the (311) plane, the average crystallite size increases consistently with the temperature.

4. Conclusions

We have successfully prepared thick coatings of metallic aluminium on brass substrates by electrodeposition from (Bmim)Cl/AlCl₃ 40:60 ionic liquid. The investigation of the surface morphology, the crystal orientation, as well as the process yield evidenced the effects of temperature and mixing conditions.

Particularly, the process yield proved useful to assess the optimal deposition conditions to achieve compact and dense deposits. Yield lower than 100% can be related to the formation of dendritic coatings due by mass transfer limitations. Regarding the effect of operative conditions, temperature increase plays a positive role enhancing the deposition yield and smoothing the roughness of the deposits. On the other hand, sonication greatly improves the mobility of the species inside the IL allowing 100% yield, but also forcing a slight increase in roughness [25].

The combined effects of the experiments demonstrated that for temperatures above 60 °C, mixing has a larger effect with respect to temperature in reducing the roughness of the deposits. Below 40 °C, temperature affects the morphology of the coatings more effectively. It is reasonable to suppose that the two effects have a competitive role in growing the layer, with a threshold assessed between 40 °C and 60 °C. Compared to the sonication, stirring shows a lower yield at nearly room temperatures, but at higher temperatures the morphological and roughness studies show similar trends between these two mixing systems.

Regarding XRD analysis, the texturing of the Al coating is related to the temperature of the deposition process, favouring the orientation along the (111) and (311) axis. That is confirmed by the crystallite size analysis which demonstrated the preferential growth along different zonal axis according to different mass transport conditions [26]. In general, the mixing conditions do not affect the crystallites' size, while increasing the temperature does. Moreover, the maximum of the crystallite strain at 40 °C, in each set of mixing conditions, can be explained as a higher concentration of defects in the crystallites. This phenomenon cannot be confirmed in this study and the reason for its occurrence has to be understood. We suggest that it can be considered a trade-off between the nucleation-growth mechanism and the improvement of the mass transport of the active species.

In conclusion, higher temperatures and stronger mixing conditions promote the deposition of smoother and thicker aluminium deposits. However, in order to move towards the industrialization of the process and to increase the durability of the IL, temperatures above 60 °C should be avoided. In order to speed up the electrodeposition process, mechanical stirring or mild sonication can be successfully adopted.

Acknowledgments: The research leading to these results has received funding from the European Union Seventh Framework Programme (FP7/2007-2013) under grant agreement no. 608698.

Author Contributions: Stefano Caporali and Massimo Innocenti conceived and designed the experiments. Enrico Berretti and Stefano M. Martinuzzi obtained and characterized the deposits; Andrea Giaccherini performed the XRD characterization and analysed the data. Thomas J.S. Schubert and Frank M. Stiemke supplied the ILs used in this study. Stefano Caporali also wrote the paper.

Conflicts of Interest: The authors declare no conflict of interest.

Abbreviations

The following abbreviations are used in this manuscript:

| | |
|------|------------------------------|
| IL | Ionic liquid |
| Bmim | 1-Butyl-3-methyl-imidazolium |
| SCE | Standard calomel electrode |
| WG | Gaussian width |
| WL | Lorentzian width |
| OCP | Open circuit potential |
| PD | potentiodynamic |

Appendix A. Roughness

Four different roughness parameters are considered in this article: Rt, Ra, Rz ISO, and Rz [27,28]. Rt is the so called total roughness, the height between the deepest valley and the highest peak extrapolated from the entire evaluation length.

Ra is the average roughness, the arithmetic mean of the profile from a mean line.

Rz ISO and Rz are similar to the Rt value; in fact, they are expressed as the mean of the sum of the maximum value of profile peak height and the maximum profile valley depth taken in various sampling lengths within the evaluation length (ten for the Rz ISO and five for the Rz).

While Ra and Rt alone may be of very limited value in assessing the overall surface roughness of a sample (particularly Rt which can be seriously affected by a single spurious scratch or particle of dirt on the surface), their conjunction with the two Rz values could greatly boost our comprehension of the homogeneity of the obtained deposits. In addition, the variance related to the roughness

measurements helped us to visualize the surface homogeneity of the obtained deposits. In fact, roughness parameters were collected considering five measurements within three samples for each experiment. Larger errors are related to higher inhomogeneity of the surfaces, while smaller ones represent more homogeneous surfaces.

References

1. Grjotheim, K.; Halvor, K. *Introduction to Aluminium Electrolysis: Understanding the Hall-Héroult Process*, 2nd ed.; Aluminium-Verlag: Düsseldorf, Germany, 1993.
2. Markiewicz, M.; Hupka, J.; Joskowska, M.; Jungnickel, C.H. Potential application of ionic liquids in aluminium production—Economic and ecological assessment. *Physicochem. Probl. Miner. Process.* **2009**, *43*, 73–84.
3. Takahashi, S.; Koura, N.; Kohara, S.; Sabouni, M.L.; Curtiss, L. Technological and scientific issues of room-temperature molten salts. *Plasma ions* **1999**, *2*, 91–105. [[CrossRef](#)]
4. Abbott, A.P.; Harris, R.C.; Hsieh, Y.T.; Ryder, K.S.; Sun, I.W. Aluminium electrodeposition under ambient conditions. *Phys. Chem. Chem. Phys.* **2014**, *16*, 14675–14681. [[CrossRef](#)] [[PubMed](#)]
5. Fang, Y.; Yoshii, K.; Jiang, X.; Sun, X.G.; Tsuda, T.; Mehio, N.; Dai, S. An AlCl_3 based ionic liquid with a neutral substituted pyridine ligand for electrochemical deposition of aluminum. *Electrochim. Acta* **2015**, *160*, 82–88. [[CrossRef](#)]
6. Pulletikurthi, G.; Bödecker, B.; Borodin, A.; Weidenfeller, B.; Endres, F. Electrodeposition of Al from a 1-butylpyrrolidine- AlCl_3 ionic liquid. *Prog. Nat. Sci. Mater. Int.* **2015**, *25*, 603–611. [[CrossRef](#)]
7. Su, C.J.; Hsieh, Y.T.; Chen, C.C.; Sun, I.W. Electrodeposition of aluminium wires from the Lewis acidic AlCl_3 /trimethylamine hydrochloride ionic liquid without using a template. *Electrochem. Commun.* **2013**, *34*, 170–173. [[CrossRef](#)]
8. Endo, A.; Miyake, M.; Hirato, T. Electrodeposition of aluminium from 1,3-dimethyl-2-imidazolidinone/ AlCl_3 baths. *Electrochim. Acta* **2014**, *137*, 470–475. [[CrossRef](#)]
9. Hadi, M.A.; Abood, N.L.D. Morphology of electrodeposited aluminium metal from aluminium chloride-urea room temperature ionic liquid (RTIL) at variable parameter. *Int. J. Sci. Res.* **2015**, *4*, 753–760.
10. Wang, Q.; Chen, B.; Zhang, Q.; Lu, X.; Zhang, S. Aluminium deposition from Lewis acidic 1-butyl-3-methylimidazolium chloroaluminate ionic liquid ((Bmim)Cl/ AlCl_3) modified with methyl nicotinate. *ChemElectroChem* **2015**, *2*, 1794–1798. [[CrossRef](#)]
11. Wang, Q.; Zhang, Q.; Chen, B.; Lu, X.; Zhang, S. Electrodeposition of bright Al coatings from 1-butyl-3-methylimidazolium chloroaluminate ionic liquids with specific additives. *J. Electrochem. Soc.* **2015**, *162*, D320–D324. [[CrossRef](#)]
12. Yue, G.; Lu, X.; Zhu, Y.; Zhang, X.; Zhang, S. Surface morphology, crystal structure and orientation of aluminium coatings electrodeposited on mild steel in ionic liquid. *Chem. Eng. J.* **2009**, *147*, 79–86. [[CrossRef](#)]
13. Chang, J.K.; Chen, S.Y.; Tsai, W.T.; Deng, M.J.; Sun, I.W. Electrodeposition of aluminium on magnesium alloy in aluminium chloride (AlCl_3)–1-ethyl-3-methylimidazolium chloride (EMIC) ionic liquid and its corrosion behavior. *Electrochem. Commun.* **2007**, *9*, 1602–1606. [[CrossRef](#)]
14. Bardi, U.; Caporali, S.; Craig, M.; Giorgetti, A.; Perissi, I.; Nicholls, J.R. Electrodeposition of aluminium film on P90 Li–Al alloy as protective coating against corrosion. *Surf. Coat. Technol.* **2009**, *203*, 1373–1378. [[CrossRef](#)]
15. Zheng, Y.; Zhang, S.; Lu, X.; Wang, Q.; Zuo, Y.; Liu, L. Low-temperature electrodeposition of aluminium from Lewis acidic 1-allyl-3-methylimidazolium chloroaluminate ionic liquids. *Chin. J. Chem. Eng.* **2012**, *20*, 130–139. [[CrossRef](#)]
16. Guikuan, Y.; Suojang, Z.; Yanli, Z.; Xingmei, L.; Shuai, L.; Zengxi, L. A promising method for electrodeposition of aluminium on stainless steel in ionic liquid. *AIChE J.* **2009**, *55*, 783–796.
17. Pradhan, D.; Reddy, R.G. Dendrite-free aluminium electrodeposition from AlCl_3 –1-ethyl-3-methylimidazolium chloride ionic liquid electrolytes. *Metall. Mater. Trans. B* **2012**, *43*, 519–531. [[CrossRef](#)]
18. Choudhary, R.K.; Kain, V.; Hubli, R.C. Stirring effects on aluminium coatings electrodeposited in ionic liquids. *Surf. Eng.* **2014**, *30*, 562–567. [[CrossRef](#)]
19. De Keijser, T.H.; Langford, J.I.; Mittemeijer, E.J.; Vogels, A.B.P. Use of the Voigt function 406 in a single-line method for the analysis of X-ray diffraction line broadening. *J. Appl. Crystallogr.* **1982**, *15*, 308–314. [[CrossRef](#)]

20. Scardi, P.; Leoni, M.; Delhez, R. Line broadening analysis using integral breadth methods: A critical review. *J. Appl. Crystallogr.* **2004**, *37*, 381–390. [[CrossRef](#)]
21. Balzar, D. Voigt-function model in diffraction line-broadening analysis, in defect and microstructure analysis from diffraction. *Int. Union Crystallogr. Monogr. Crystallogr.* **1999**, *10*, 94–126.
22. Macrae, C.F.; Bruno, I.J.; Chisholm, J.A.; Edgington, P.R.; McCabe, P.; Pidcock, E.; Rodriguez-Monge, L.; Taylor, R.; van de Streek, J.; Wood, P.A. Mercury CSD 2.0—New features for the visualization and investigation of crystal structures. *J. Appl. Crystallogr.* **2008**, *41*, 466–470. [[CrossRef](#)]
23. Wyckoff, R.W.G. *Crystal Structures*; Wiley: New York, NY, USA, 1963; pp. 7–83.
24. Downs, R.T.; Hall-Wallace, M. The American mineralogist crystal structure database. *Am. Mineral.* **2003**, *88*, 247–250.
25. Costa, C.; Doche, M.; Hihn, J.; Bisel, I.; Moisy, P.; Léveque, J. Hydrodynamic sono-voltammetry of ferrocene in (Tf₂N)[−] based ionic liquid media. *Ultrasonics* **2010**, *50*, 323–328. [[CrossRef](#)] [[PubMed](#)]
26. Zheng, Y.; Dong, K.; Wang, Q.; Zhang, J.; Lu, X. Density, viscosity, and conductivity of lewis acidic 1-butyl- and 1-hydrogen-3-methylimidazolium chloroaluminate ionic liquids. *J. Chem. Eng. Data* **2013**, *58*, 32–42. [[CrossRef](#)]
27. Stout, K.J. Surface roughness—Measurement, interpretation and significance of data. *Mater. Eng.* **1981**, *2*, 260–265. [[CrossRef](#)]
28. Gadelmawla, E.S.; Koura, M.M.; Maksoud, T.M.A.; Elewa, I.M.; Soliman, H.H. Roughness parameters. *J. Mater. Process. Technol.* **2002**, *123*, 133–145. [[CrossRef](#)]



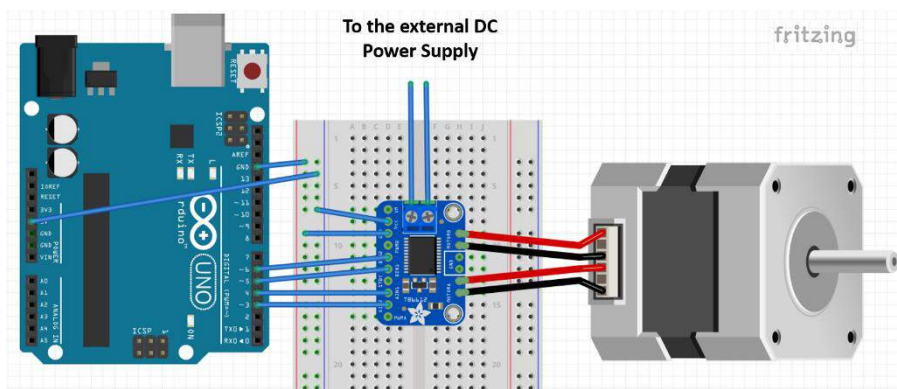
© 2016 by the authors; licensee MDPI, Basel, Switzerland. This article is an open access article distributed under the terms and conditions of the Creative Commons Attribution (CC-BY) license (<http://creativecommons.org/licenses/by/4.0/>).

6.4 Appendix D: RHC Schematics

In order to control the rotation speed of the cathode, the following elements were used:

- An ARDUINO UNO board;
- An Adafruit TB6612 Motor Driver;
- An SY42STH47-1206a Bipolar Stepper Motor;
- An external 2V 2A DC power supply.

The circuit was mounted as depicted in the following figure:



In order to regulate the rotation speed, the following Arduino programming code was used:

```
Stepper$
#include <Stepper.h>

// change this to the number of steps on your motor
#define STEPS 200

// create an instance of the stepper class, specifying
// the number of steps of the motor and the pins it's
// attached to
Stepper stepper(STEPS, 4, 5, 6, 7);

void setup() {
  Serial.begin(9600);
  Serial.println("Stepper test!");
  // set the speed of the motor to X RPMs
  stepper.setSpeed(300);
}

void loop()
{
  Serial.println("Forward");
  stepper.step(STEPS);
}

```

This value indicates the rotation speed (in RPM)

Index of the design sheets:

| | |
|----------|---------------------|
| Pag. 135 | Assembly Views |
| Pag. 136 | Front Exploded View |
| Pag. 137 | Back Exploded View |
| Pag. 138 | Section A |
| Pag. 139 | Section B |
| Pag. 140 | Cell Body |
| Pag. 141 | Cell Support |
| Pag. 142 | Cell Chamber |
| Pag. 143 | Others |

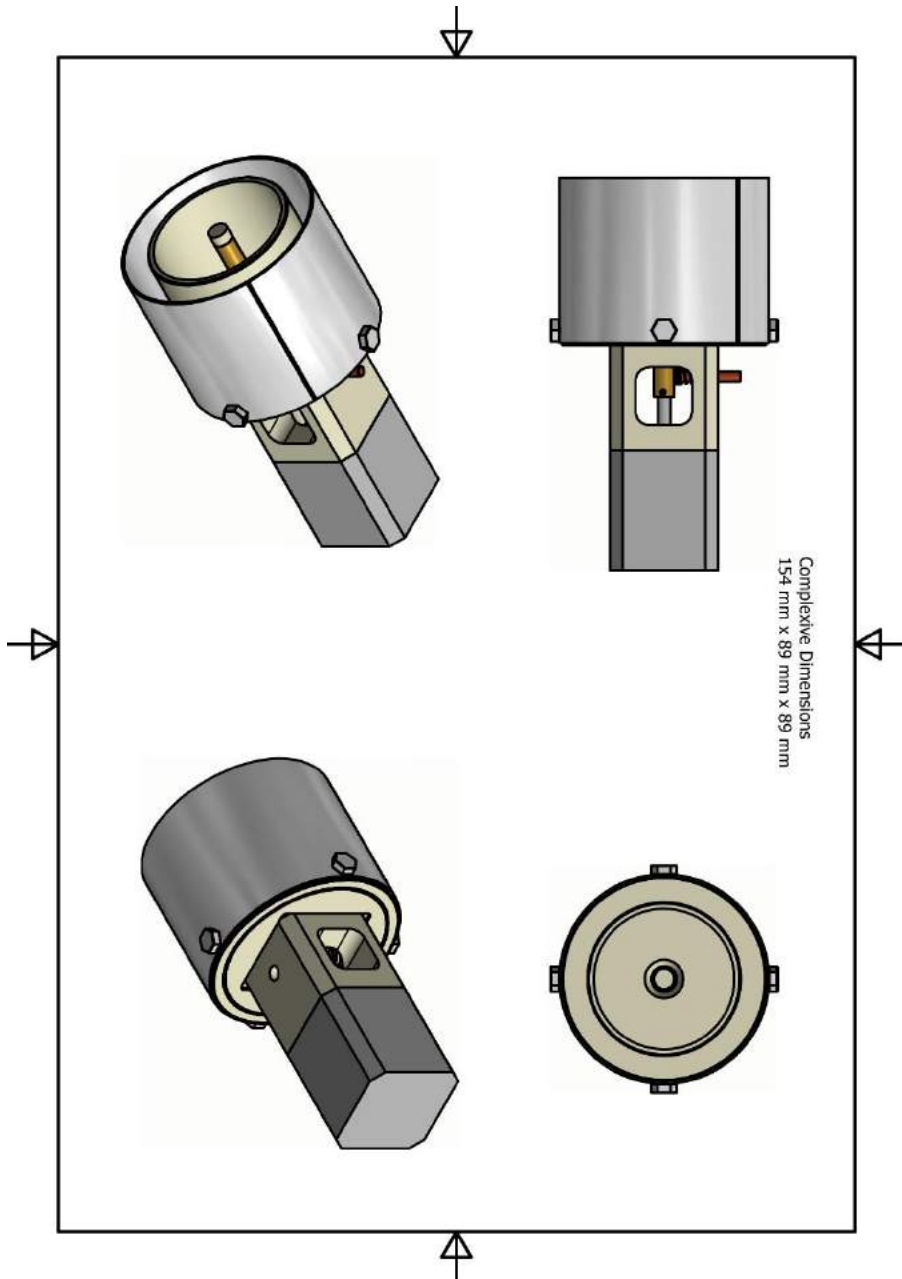


Figure 83 – Assembly views

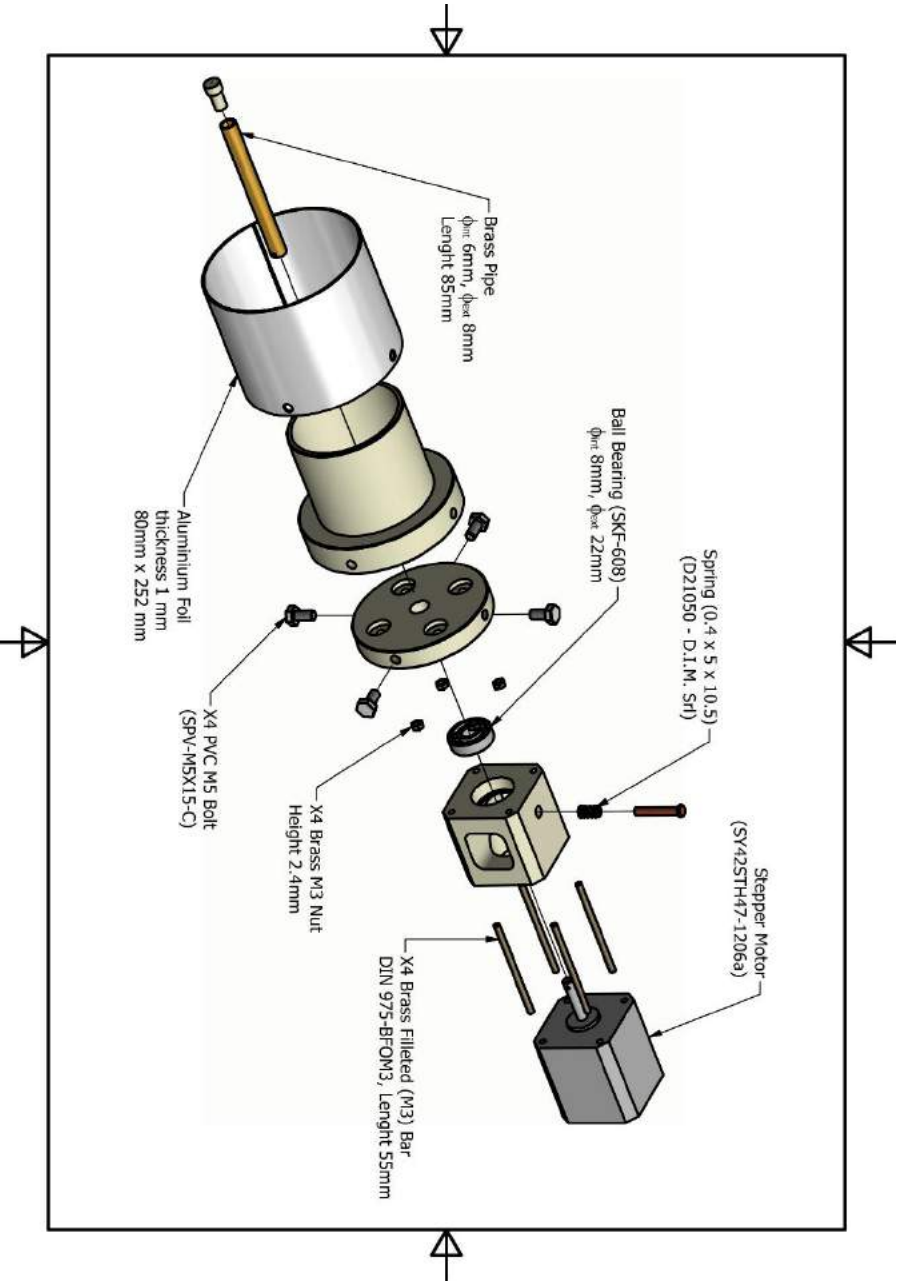


Figure 84 – Front exploded view

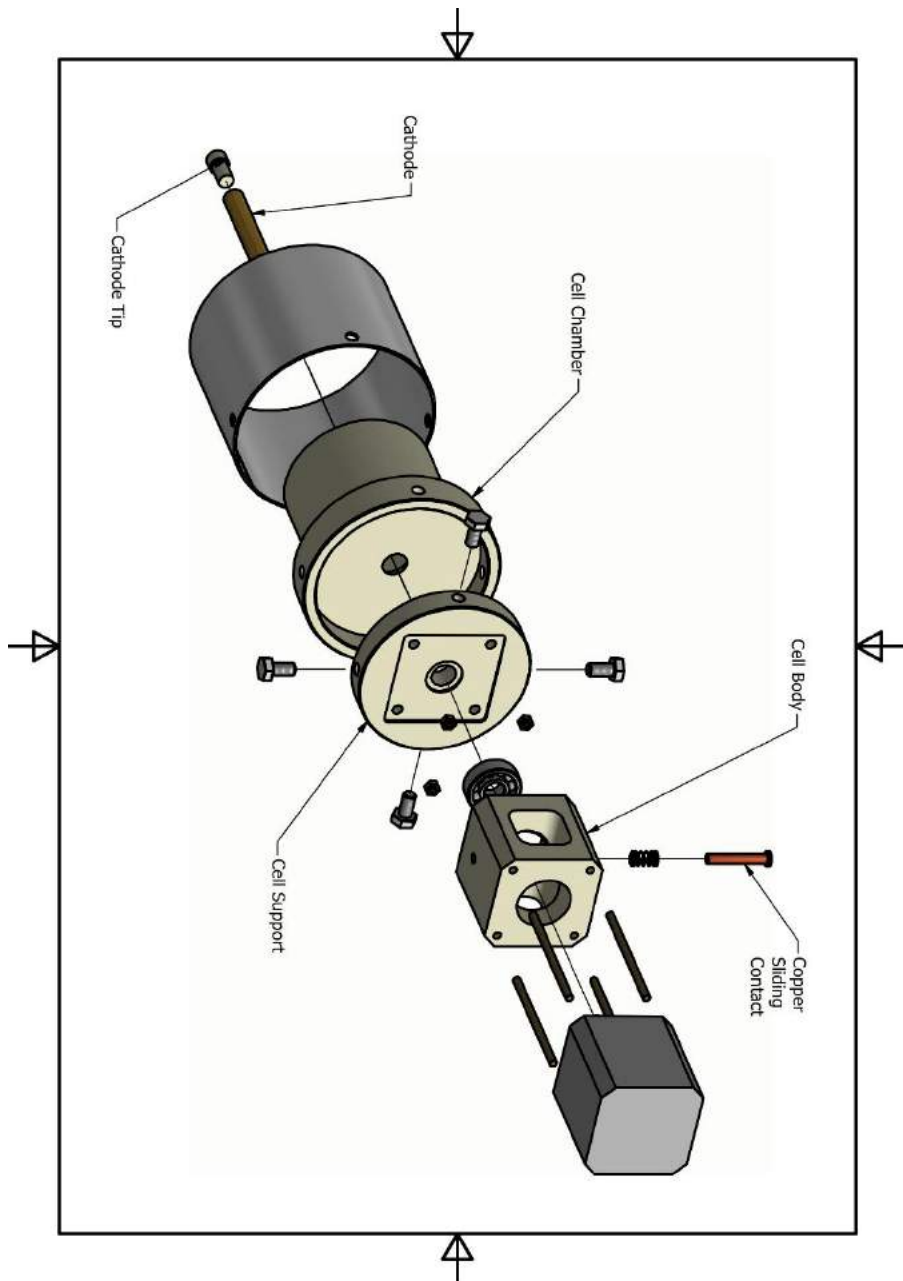


Figure 85 – Back exploded view

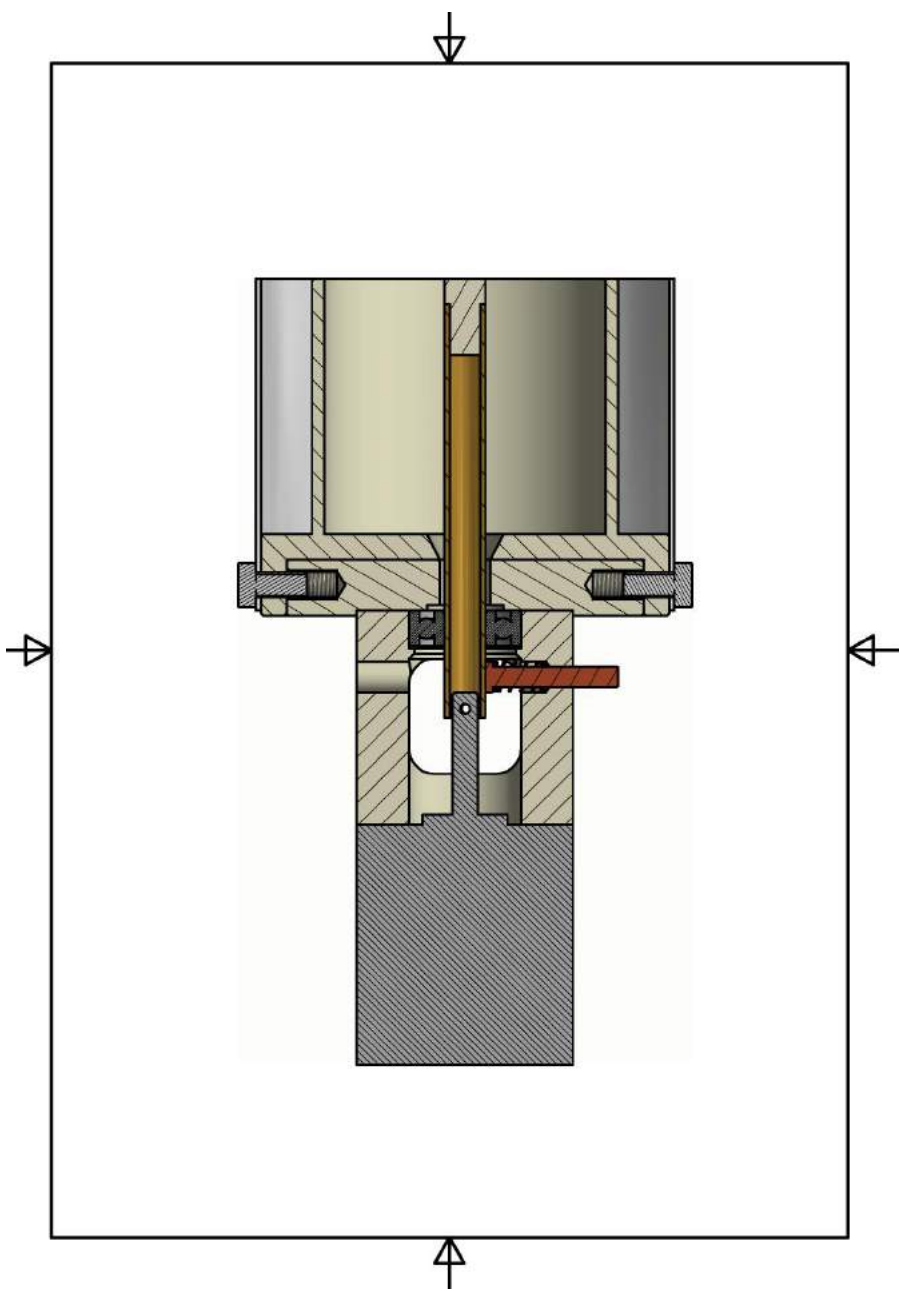


Figure 86 – Section A

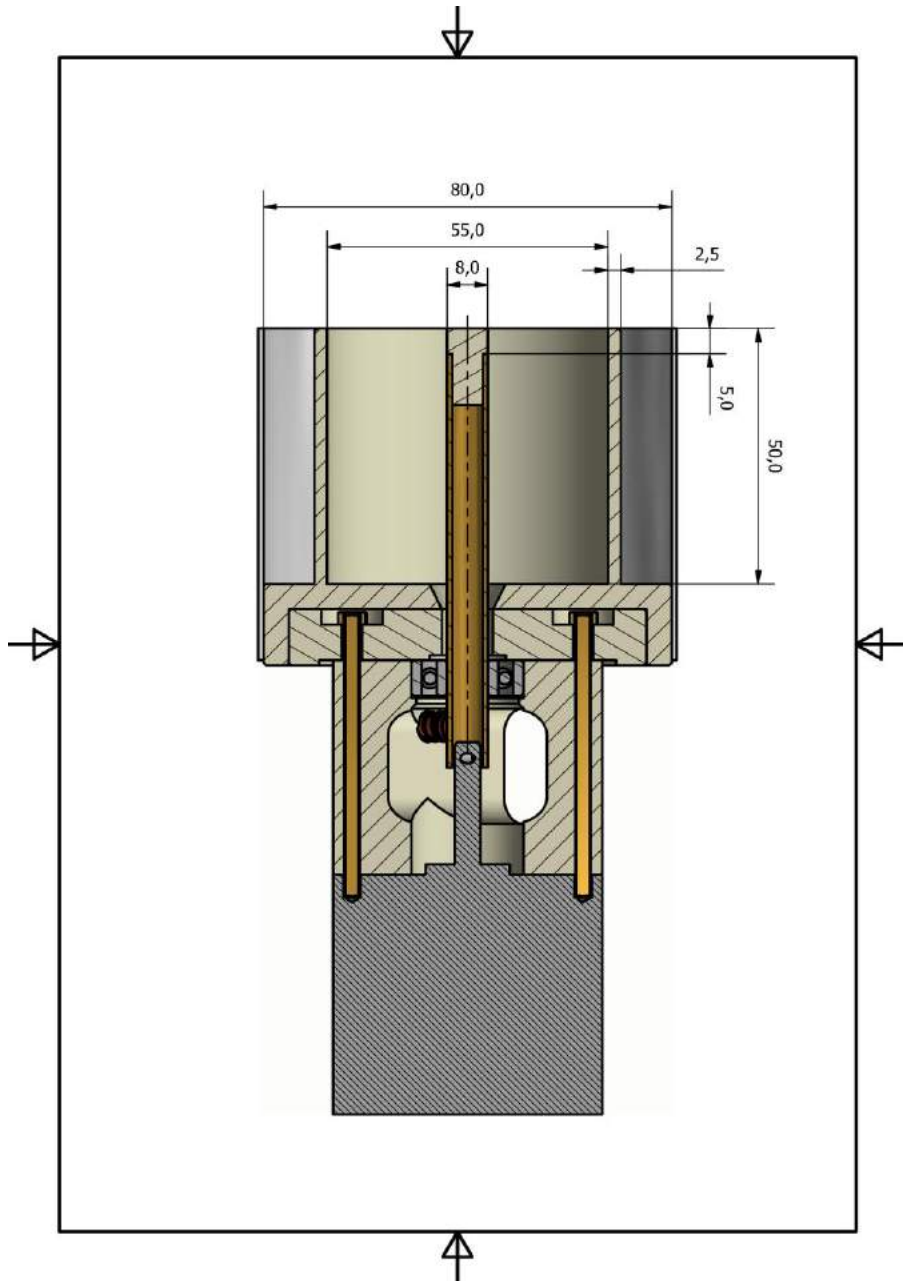


Figure 87 – Section B

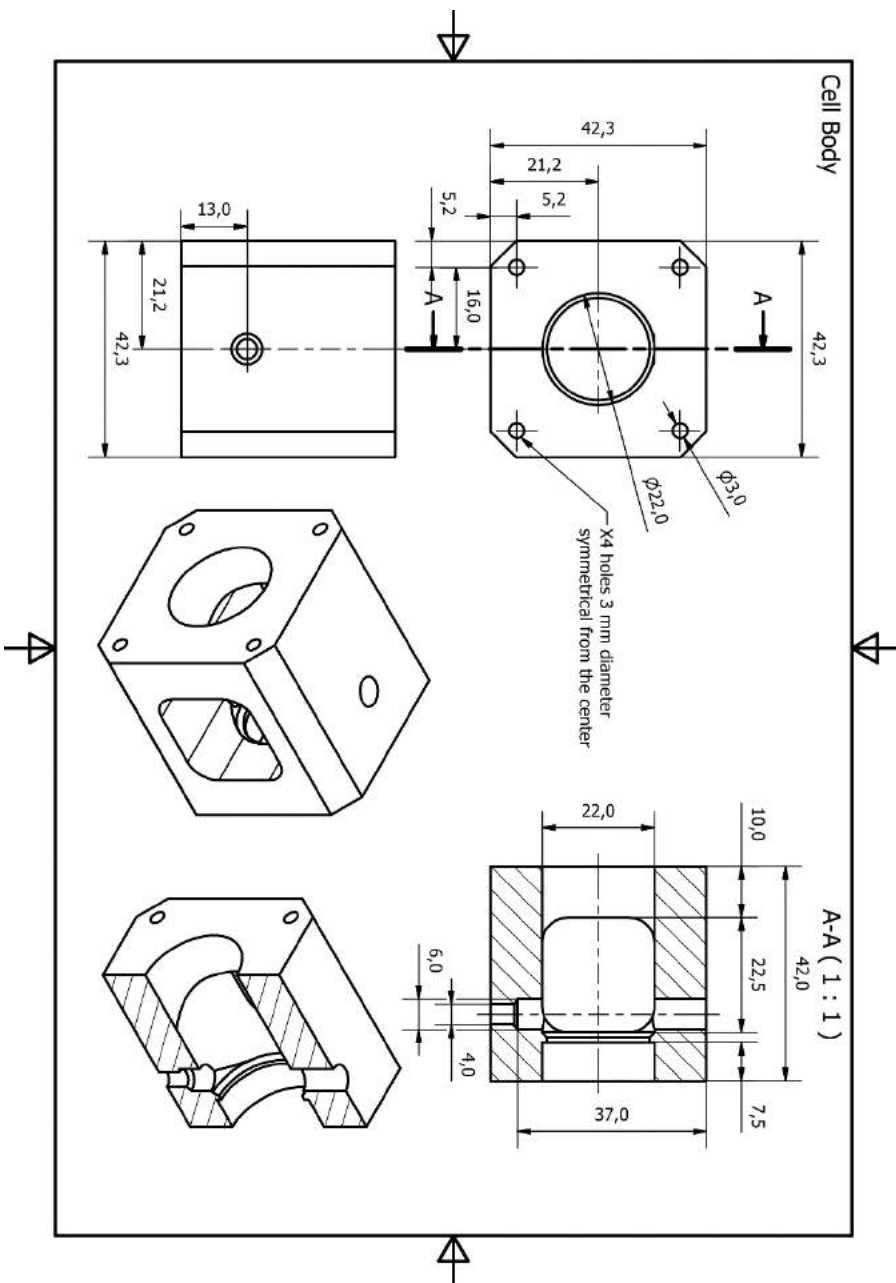


Figure 88 – Cell body

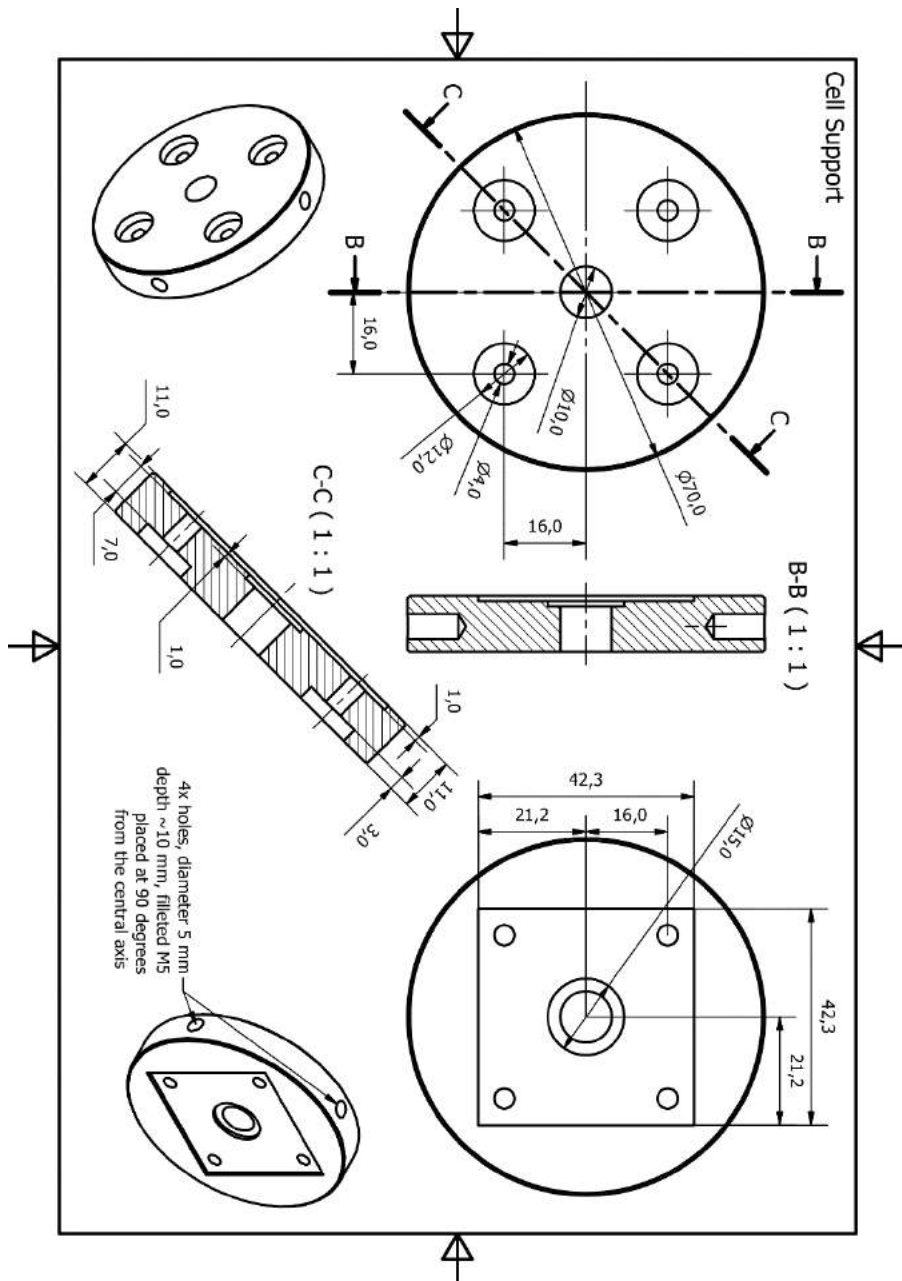


Figure 89 – Cell support

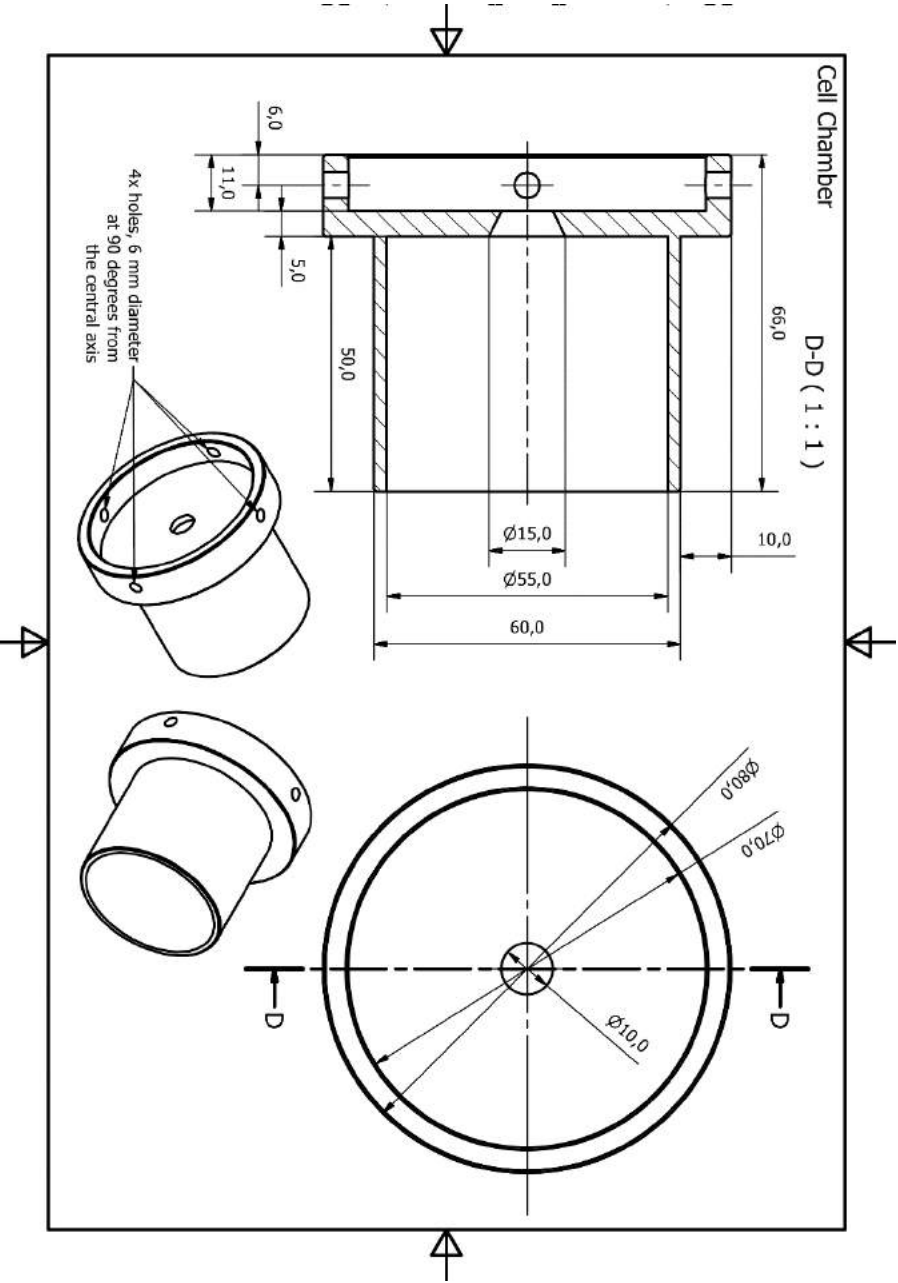


Figure 90 – Cell chamber

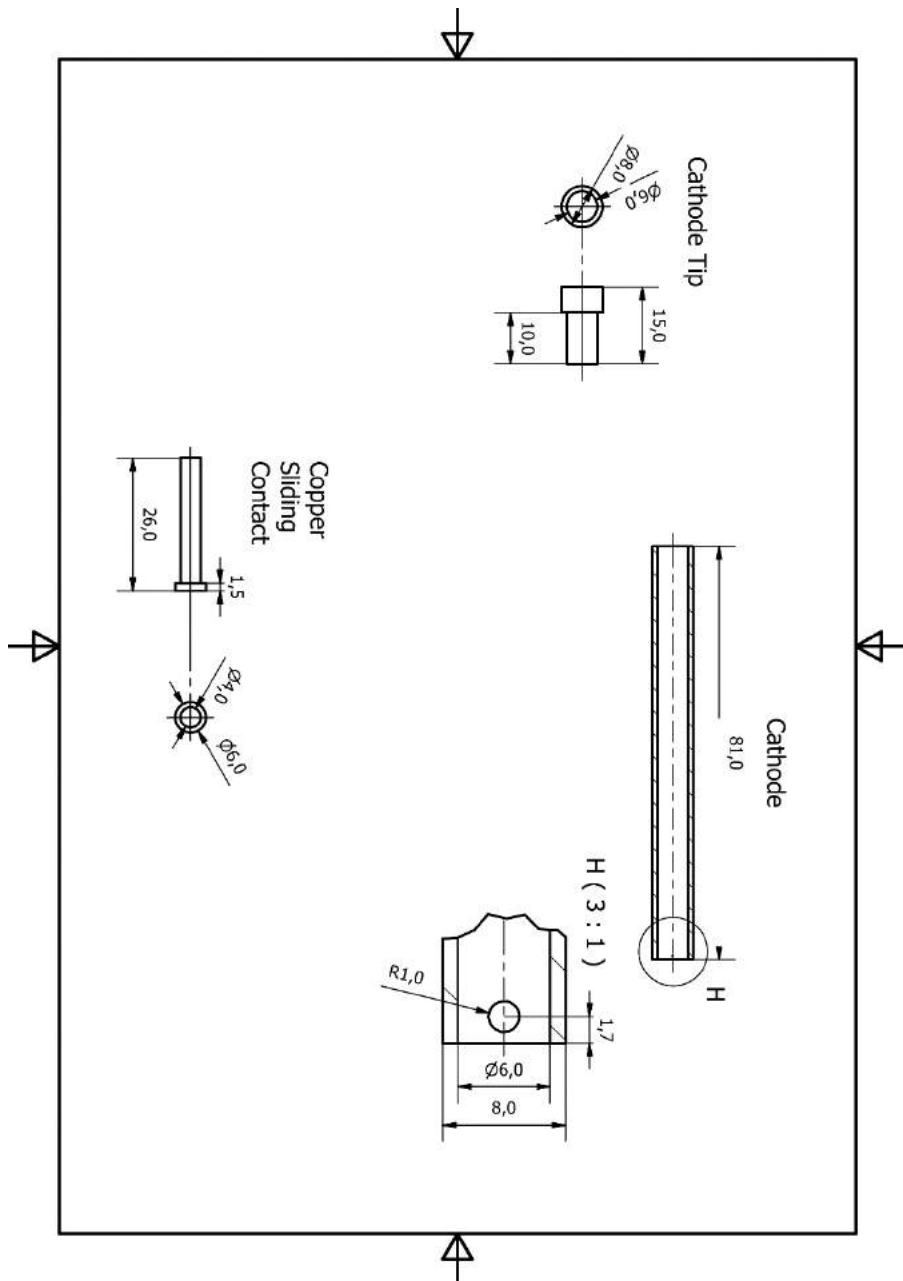


Figure 91 - Others

6.5 Appendix E: Article “Aluminizing via Ionic Liquid
Electrodeposition and Pack Cementation: A Comparative
Study with Inconel 738 and a CoNiCrAlY”



Article

Aluminizing via Ionic Liquid Electrodeposition and Pack Cementation: A Comparative Study with Inconel 738 and a CoNiCrAlY

Luca Tagliaferri ¹, Enrico Berretti ², Andrea Giaccherini ², Stefano M. Martinuzzi ²,
 Francesco Bozza ¹, Martin Thoma ³, Ugo Bardi ² and Stefano Caporali ^{4,5,6,*}

¹ Turbocoating s.p.a., Via Mistrali 7, 43040 Rubbiano di Solignano, Italy; LucaTagliaferri@turbocoating.it (L.T.); FrancescoBozza@turbocoating.it (F.B.)

² Dipartimento di Chimica, Università di Firenze, via della Lastruccia 3, 50019 Sesto Fiorentino, Italy; eberretti@gmail.com (E.B.); andrea.giaccherini@unifi.it (A.G.); ste.martinuzzi@gmail.com (S.M.M.); ugo.bardi@unifi.it (U.B.)

³ MT Consulting, Mainzerstrasse 15, 80804 Munich, Germany; martin.thoma@forumt.com

⁴ Dipartimento di Ingegneria Industriale, Università di Firenze, via di S. Marta 3, 50139 Firenze, Italy

⁵ Consorzio Interuniversitario Nazionale per la Scienza e Tecnologia dei Materiali, via Giusti 9, 50123 Firenze, Italy

⁶ Istituto Sistemi Complessi (ISC-CNR), via Madonna del Piano 10, 50019 Sesto Fiorentino, Italy

* Correspondence: stefano.caporali@unifi.it; Tel.: +39-055-457-3119

Received: 1 May 2017; Accepted: 15 June 2017; Published: 19 June 2017

Abstract: A novel aluminizing process based upon room temperature Al-electrodeposition from Ionic Liquids followed by diffusion heat treatment was applied on bare- and CoNiCrAlY-coated Inconel 738 (IN738). The aluminized samples were tested by isothermal oxidation at 1000 °C in air. The microstructural and chemical evolution of the samples were determined as function of oxidation time and compared with the currently applied coatings obtained via pack cementation. The newly proposed method is suitable for the CoNiCrAlY coating, but not for the bare IN738. In the latter, the formed Al-enriched layer is much thinner and the anticorrosion properties resulted in being reduced. This is probably due to the presence of precipitates, which slow down the aluminum inward diffusion impairing the formation of a well-developed interdiffusion zone (IDZ). Traces of the electrolyte, embedded during the Al-electrodeposition process, can be seen as the origin of these precipitates.

Keywords: ionic liquids; electrodeposition; aluminum; isothermal test; NiAl; Ni superalloys; gas turbine; SEM-EDX; coatings

1. Introduction

Inconel 738 (IN738) is a nickel-based superalloy widely used as a high temperature material for gas turbine and aerospace applications. Its industrial success is based on the superior creep resistance with respect to other alloys at the high operating temperatures employed in gas turbine engines (up to 1300 °C). However, this alloy is not without drawbacks. In particular, it presents low resistance to hot corrosion and high temperature oxidation. For this reason, surface modifications are mandatory in order to improve the durability of IN738 parts in the hot sections of gas turbines.

The oxidation and corrosion resistance of high-temperature alloys and coatings is dependent on the formation and retention of a thin, dense, continuous external oxide scale, which serves as a diffusion barrier preventing oxygen diffusion and therefore the rapid oxidation of the metal beneath. Alumina is typically the preferred protective scale for applications above 900 °C. Thus, two types of alumina-forming coatings are currently used as oxidation-resistant systems on gas turbine superalloy; nickel aluminide diffusion coatings (NiAl) [1–6] and MCrAlX alloys (where M = Ni, Co and/or Fe

and $X = Y$, Hf, Zr and/or Si). The diffusion aluminide coatings are based on β -NiAl phase; the MCrAlY ($M = \text{Ni, Co, or NiCo}$) overlay coatings are based on a mixture of β -NiAl and γ' -Ni₃Al or γ phases. One important advantage of the overlay coatings is the extra freedom in the choice of coating composition. A further over-aluminizing step on MCrAlX coatings is generally performed in order to enhance their oxidation protection at high temperatures [7–11].

Due to many merits such as low cost, convenient operation and mature techniques, diffusion aluminide coatings have been extensively applied on the surface of gas turbine blades and vanes [12]. Pack cementation is the principal industrial methodology to produce diffusion aluminide coatings. It is based on the deposition of aluminum from Al-halides (typically AlCl₃) created from a powder mix containing an Al-source (CrAl or CoAl), an halide activator (typically NH₄Cl) and an inert filler to avoid particles sintering [2,12,13]. At high temperatures (from 650 to 1100 °C), a reaction takes place with the creation of volatile, Al-rich halides that finally lead to the diffusion of metallic Al into the Ni/Co base [12] forming the Ni–Al intermetallic compounds and secondary phases.

Nickel-aluminide diffusion coatings can also be achieved by diffusing pure aluminum—layered on the surface—into the nickel-based alloy. The process is well known and models for Al and Ni-diffusion have been proposed [14,15]. This method requires the deposition of a pure aluminum layer and, recently, a new method to create Al-enriched coatings has been proposed on the basis of the electrodeposition of metallic aluminium from Ionic Liquids (ILs) [16]. ILs, and in particular chloroaluminated-based ILs, are a well known family of non-protic compounds from which layers of aluminum can be obtained by electrodeposition at room temperature. Even though the process must be carried out in moisture-free environments, it has several advantages over vacuum-based techniques such as: high deposition rate (10–20 $\mu\text{m/h}$), simple and cheap instrumentation, and low energy consumption [17–22]. For these reasons, the industrialization of the Al-plating process for automotive and aerospace applications is of great technological interest and it is currently under industrial development [23,24].

The present work deals with a two-step aluminizing process based on (a) the electrodeposition of aluminum and (b) the formation of Ni–Al intermetallics by means of thermal treatment. The results of this new process in terms of microstructural investigation and isothermal oxidation test were compared with the currently employed pack cementation process over bare IN738 (aluminizing) and CoNiCrAlY-coated IN738 (over-aluminizing). The results show comparable oxidation resistance for the over-aluminizing process while on bare IN738 (aluminizing) the sample produced with the two-step process resulted less performing respect to the ones produced by pack cementation.

2. Materials and Methods

Flat samples of IN738 (16 wt % Cr, 8.5 wt % Co, 3.4 wt % Ti, 2.6 wt % W, 2.65 wt % Ta, 1.75 wt % Mo, 0.11 wt % C, Ni balance) were prepared by casting and machining $7 \times 7 \text{ cm}^2$ tokens. Al-rich coatings were prepared on bare and CoNiCrAlY-coated IN738 via IL double step and pack cementation and will be called from now on, respectively, as: IL or Pack “aluminizing” and IL or Pack “over-aluminizing”.

Five types of sample were prepared as listed below:

- “IL aluminizing”: IN738 + Al by Ionic Liquids + Heat treatment (1100 °C in vacuum).
- “IL over-aluminizing”: IN738 + CoNiCrAlY + Al by Ionic Liquids + Heat treatment (1100 °C in vacuum).
- “Pack aluminizing”: IN738 + pack cementation process (1000 °C) + Heat treatment (1100 °C in vacuum).
- “Pack over-aluminizing”: IN738 + CoNiCrAlY + pack cementation process (1000 °C) + Heat treatment (1100 °C in vacuum).
- “Reference coating”: IN738 + CoNiCrAlY + Heat treatment (1100 °C in vacuum).

Furthermore, $200 \pm 50 \mu\text{m}$ thick CoNiCrAlY coatings (38.1 wt % Co, 32 wt % Ni, 21 wt % Cr, 8 wt % Al, 0.5 wt % Y) were deposited, prior to the aluminizing processes on IN738, by HVOF (High

Velocity Oxygen Fuel) thermal spray using a JP5000 HVOF gun, manufactured by Artec s.r.l (Parma, Italy) working in an oxygen/kerosene configuration.

Aluminum coatings were electrodeposited from 1-butyl-3-methylimidazolium chloride/Aluminum chloride ([Bmim]Cl/ AlCl_3) 40/60 mol % supplied by IoLiTec Ionic Liquids Technologies GmbH (Heilbronn, Germany) and used without further purification. The process was carried out inside a N_2 filled glove box (Iteco mod 10A, Castelbolognese, Italy), with a moisture content below 30 ppm using a PAR model 2273 potentiostat (Oak Ridge, TN, USA) controlled by PowerSuite 2.58 software (v. 2.58, Princeton Applied Research, Oak Ridge, TN, USA). A pure aluminum foil (Goodfellow, Huntingdon, UK, 99.0) was used as counter electrode.

The Al-deposits were produced by direct deposition in current controlled (galvanostatic) conditions at $10 \text{ mA} \cdot \text{cm}^{-2}$ for 2 h at room temperature, and then rinsed with acetone and distilled water to remove traces of the adsorbed electroplating bath. Figure 1 depicts the cross sections of the Al layer deposited on bare IN738 and CoNiCrAlY-coated IN738.

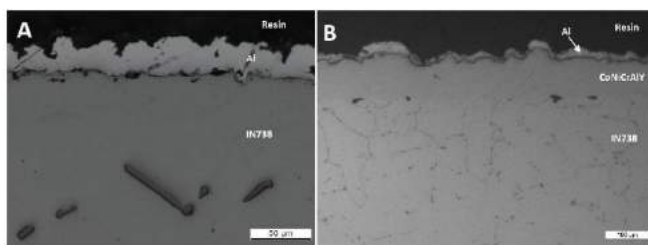


Figure 1. SEM images (SE signal) of the aluminum coating on bare IN738 (A) and CoNiCrAlY coated IN738 (B) before the heat treatment. In both cases, a pure Al layer about $20 \mu\text{m}$ thick is detectable on the top of the sample.

The heat treatment was finally performed at 1100°C for 2–5 h in vacuum (range 10^{-1} – 10^{-3} mbar) allowing the Al diffusion inwards the substrates but avoiding its high temperature oxidation (for process details, see Ref. [14] and citations therein).

Samples of bare IN738 and CoNiCrAlY-coated underwent the same treatment, while replacing the two-step process with the pack aluminizing process (for process details, see Ref. [8] and citations therein). The process was carried out by covering the surface to be Al-enriched with a powder mix containing an Al source (CoAl or CrAl alloy), an activator (NH_4Cl) and an inert filler (Al_2O_3 powder). The process was carried out in Ar atmosphere at 1000°C for 2–5 h. At this temperature, a reaction took place within the powder mix, creating the Al chloride vapour phase, able to let the inward diffusion of Al into both IN738 and CoNiCrAlY.

For each of the 5 systems, three samples were prepared applying a post treatment at 1100°C in vacuum (range 10^{-1} – 10^{-3} mbar) for 2–5 h as final step. The obtained samples were tested under isothermal conditions (air atmosphere, 1000°C) and characterized before oxidation test (0 h) and after 500 and 1000 h (end of the test) by means of Scanning electron microscope (SEM), X-ray diffraction (XRD) and micro-hardness analyses. Since Ni–Al intermetallic phases are materials harder than the Ni superalloy, a micro-hardness profile evaluation can be profitably used as indirect indication of the formation of these compounds.

Metallographic cross sections of the samples were prepared and investigated by using a Hitachi 2300 SEM microscope (Tokyo, Japan). Compositional profiles were determined by means of an Energy Dispersive Microanalysis (EDS) system (NORAN NSS 300, Thermo Fisher Scientific, Waltham, MA, USA) using 20 kV acceleration and 34.7° take off angle. The peaks were fitted by Gaussian curves applying the ZAF (atomic number absorption fluorescence) correction.

The crystalline phases present in the coatings were determined through XRD, using a XRD Bruker D8 Advance powder diffractometer (Bruker, Billerica, MA, USA) employing Cu K α (1.54187 Å) radiation covering a 2θ range between 36° and 80°, applying a step size of 0.022° and a step counting time of 0.27 s.

Hardness measurements were carried out by using a HX1000 micro-hardness tester (Remet, Bologna, Italy) equipped with a Vickers indenter. The measurements were performed using a load of 25 g and repeated at least 4 times for every sample on randomly chosen profiles of the cross section.

3. Results

3.1. Comparison between Pack Aluminizing and IL Aluminizing over IN738

The evolution of the base material (IN738) aluminized, via both pack cementation and ILs electrodeposition, was evaluated and compared as a function of the isothermal test duration.

Figure 2 depicts the SEM-BSE (backscattered electron mode) micrographs of the cross sections obtained on both the type of samples as function of test duration.

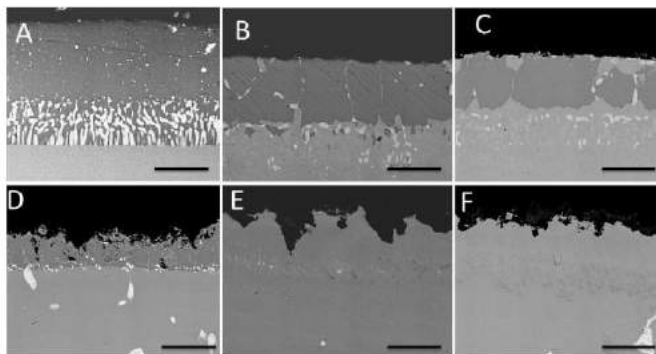


Figure 2. SEM images (BSE signal) of the aluminized IN738 as function of the isothermal test duration (A,D = 0 h; B,E = 500 h; C,F = 1000 h) for IN738 + pack aluminizing + heat treatment (A–C) and IN738 + IL Aluminizing + heat treatment (D–F). Scale bar 25 μ m.

The coatings substantially differ in terms of thickness and microstructure even before the thermal tests. The one obtained via pack aluminizing (Figure 1A) is thicker (up to 40 μ m) and presents a well-developed interdiffusion zone (IDZ) compared to the sample obtained via IL aluminizing process (Figure 1D). Clues about the reduced thickness of the diffusion layer were investigated analyzing the interphase between the IL aluminide coating and the IN738 substrate. Figure 3 displays the backscattered electron (BSE) magnification of this zone. It shows the presence of a large number of bright particles which imply a high electron scattering power generated by high atomic number elements. The EDS analysis performed on these particles shows the presence of W, Nb, Mo, Ti and Ta, probably as carbides or nitrides (Table 1). It seems reasonable that these precipitates, absent in the sample prepared via pack cementation, slow down the Al inward diffusion. As a consequence of the reduced inward diffusion rate, at the severe condition of the heat treatment (vacuum, 1100 °C), aluminum sublimation could become a relevant process leading to the loss of part of the deposit. The most likely explanation for the presence of these compounds is the presence of traces of the electrolyte embedded in the growing Al-layer. Carbon and/or nitrogen present in the cation of the

IL may have reacted with the metals present in the base material (W, Ta, Nb, Ti, Mo) during the heat treatment (1100 °C) in vacuum, leading to the formation of carbides and/or nitrides.

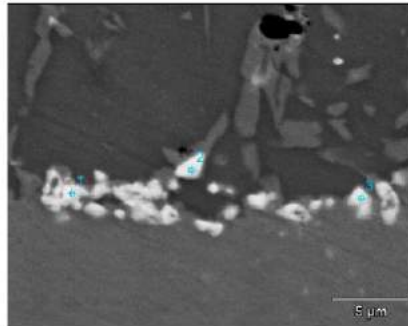


Figure 3. SEM image (BSE signal) of the interphase between IL aluminide coating and IN738 substrate. Numbers indicate the spots on which EDS analysis was performed. Scale bar 25 μ m.

Table 1. EDS spot analysis over the points depicted in Figure 2.

| Element | Point 1 | Point 2 | Point 3 |
|---------|---------|---------|---------|
| Al | 0.2 | 0.4 | 0.3 |
| Ti | 3.7 | 1.7 | 15.5 |
| Cr | 50.4 | 45.9 | 3.3 |
| Co | 2.1 | 3.8 | 2.5 |
| Ni | 13.2 | 25.3 | 20.7 |
| Mo | 12.0 | 9.3 | — |
| W | 18.4 | 13.6 | — |
| Nb | — | — | 4.7 |
| Ta | — | — | 53.0 |

EDS compositional analysis, micro-hardness profiles and XRD patterns have been realized to better characterize the samples. Figures 4–6 show the elemental profile concentration, the hardness profiles and the XRD pattern of these coatings, respectively.

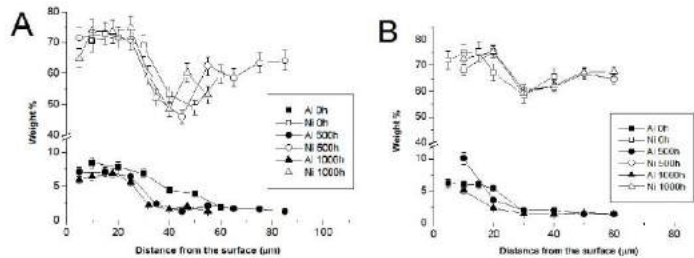


Figure 4. Compositional profiles of Al (full symbols) and Ni (empty symbols) for the cross sections depicted in Figure 1 as determined by EDS measurement. (A) and (B) panels depict data for IN738 + pack aluminizing + heat treatment and IN738 + IL aluminizing + heat treatment, respectively.

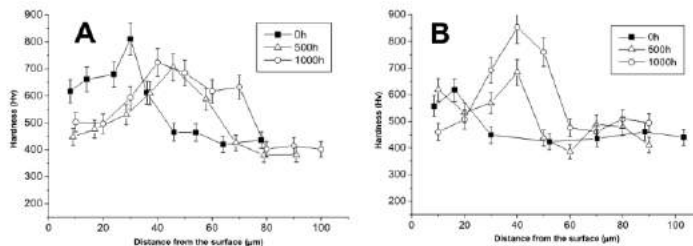


Figure 5. Hardness profile measurement for IN738 + Pack aluminizing + Post treatment (A) and IN738 + IL aluminizing + post treatment (B), respectively, at 0, 500 and 1000 h of isothermal test (1000 °C).

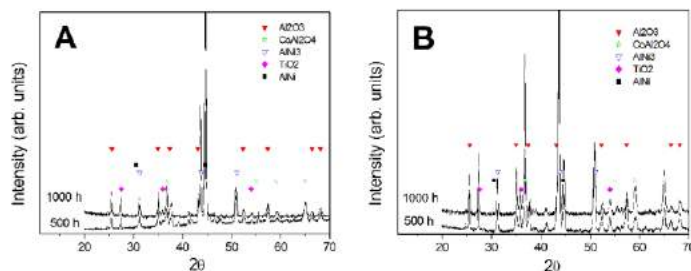


Figure 6. Surface XRD pattern of IN738 + Pack aluminizing + Post treatment (A) and IN738 + IL aluminizing + post treatment (B), respectively, after 500 and 1000 h of isothermal test (1000 °C).

Compositional and hardness profiles depicted in Figures 4 and 5 present a clear trend: pack aluminizing generates a higher concentration of aluminum and, consequently, we observe the formation of Ni–Al intermetallic compounds within the coating cross section. On the other hand, the IL aluminizing performed over IN738 resulted in a lower and more shallow Al inward diffusion leading to the formation of a different microstructure depleted in Ni–Al as proved by the lower hardness (compare the curves at 0 h of Figure 5A,B). The consequence was a lower oxidation resistance (also detectable from results at 500 and 1000 h of isothermal test). The surface of the sample obtained via ILs aluminizing also results much rougher (Figure 2E,F) and richer in oxidation byproducts such as rutile (TiO₂) (see Figure 6), providing direct evidence of severe oxidation of the base material (IN738).

On the contrary, the surface of samples obtained via pack cementation, is dominated by α -Al₂O₃, which is the oxidation product of the aluminide coating that plays a protective role toward the Ni-base superalloy (see Figure 6).

3.2. Tests on the Reference Coating: HVOF Sprayed CoNiCrAlY on IN738 with No Aluminizing Process + Heat Treatment (1100 °C in Vacuum).

To determine the oxidation resistance of the CoNiCrAlY alone, the IN738 samples coated with CoNiCrAlY, but without any over-aluminizing process, underwent oxidation tests in isothermal conditions. Figure 7 shows SEM-BSE micrographs of the cross section as a function of the test duration while Figure 8 displays the Ni and Al concentration profiles as determined by EDS.

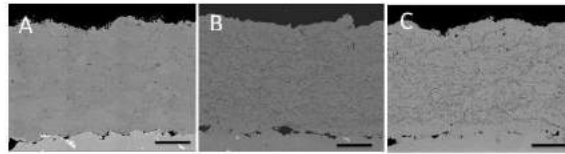


Figure 7. SEM micrographs for the HVOF sprayed CoNiCrAlY + heat treatment at 0 h (A), 500 h (B) and 1000 h (C) of isothermal test. Scale bar 50 μm .

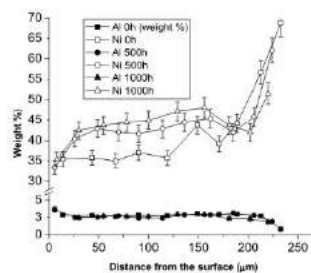


Figure 8. Ni and Al concentration profile for HVOF sprayed CoNiCrAlY on IN738 at 0, 500 and 1000 h of isothermal test.

During the high temperature test, aluminum diffuses toward the surface and oxidizes: creating the protective Al_2O_3 scale. At the same time, nickel migrates outward from the base material. Figure 8 shows the increase of Ni amount from 0 h in which Co concentration is higher than Ni, to 500 and 1000 h, where Ni becomes the dominant element in the coating. The migration of Ni at high temperature also brings changes within the microstructural composition of the CoNiCrAlY coating. Higher amounts of Ni are observed in the coatings at 500 and 1000 h. This leads to the decrease of β NiAl and the parallel increase of γ' Ni_3Al . This process has detrimental effects on the anticorrosion properties of the treatment. The microstructural evolution is clearly detectable from the micrographs depicted in Figure 7 as well as the compositional profiles depicted in Figure 8. Ni diffusion from substrate towards the bond coat leads the transformation from β to γ phase reducing the overall coating hardness (Figure 9).

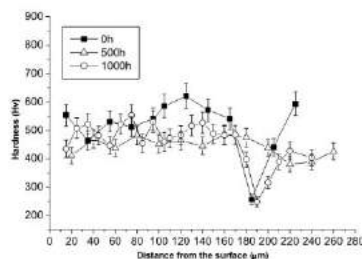


Figure 9. Micro-hardness profiles of HVOF sprayed CoNiCrAlY on IN738 + heat treatment at 0, 500 and 1000 h of isothermal test.

The evolutionary trend of CoNiCrAlY during oxidation test was finally confirmed by XRD analysis (Figure 10) on which Al_2O_3 and the mixed oxide CoAl_2O_4 result as the main oxidation byproducts [7,8].

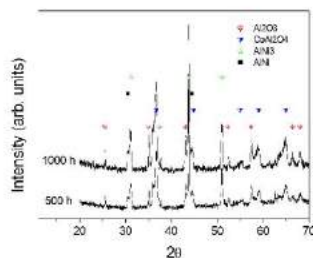


Figure 10. XRD analysis performed on HVOF sprayed CoNiCrAlY on IN738 + heat treatment at 500 and 1000 h of isothermal test.

3.3. Comparison between Pack- and IL Over-Aluminizing

As a final evaluation, the results of isothermal tests for the two over-aluminizing processes (pack aluminizing and IL aluminizing) were compared.

Microstructural investigation of the cross sections (Figure 11) provides evidence of the different behavior and trends of the double-step coated and heat treated samples with respect to the standard aluminizing process over IN738 (see Section 3.1). In this case, no formation of carbides is detected and aluminum diffuses much deeper into the metallic coating with respect to the pack aluminizing.

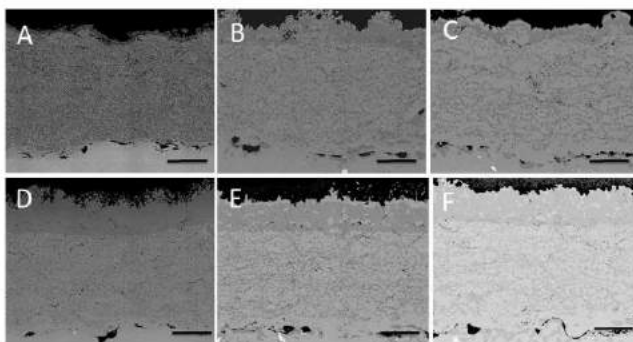


Figure 11. SEM images (BSE signal) of the over-aluminized IN738 + CoNiCrAlY as function of the isothermal test duration (A,D = 0 h; B,E = 500 h; C,F = 1000 h) for IN738 + CoNiCrAlY + pack aluminizing + heat treatment (A–C) and IN738 + CoNiCrAlY + IL Aluminizing + heat treatment (D–F). Scale bar 50 μm .

These trends are also confirmed by the compositional profiles (Figure 12): Al in the IL over-aluminized CoNiCrAlY diffuses deeper than in the case of the pack aluminizing process increasing the β NiAl phase within a thicker CoNiCrAlY section. Figure 13 depicts the hardness variation across the coating of both the over-aluminized samples: little but detectable differences in the micro-hardness values

indicate that it generally increases in the outermost portion of the coating due to the higher amount of Al diffused from the over-aluminized process. However, among the two over-aluminizing processes, the sample obtained via IL electrodeposition is characterized by larger hardness increase (from an average of 450 HV up to 700 HV in the more external portion of the coating, Figure 13B) due to the higher thickness of the over-aluminide coating itself with respect to the pack over-aluminide coatings.

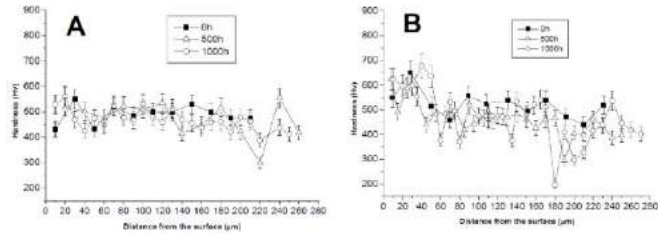


Figure 12. Compositional profiles of Al (full symbols) and Ni (empty symbols) for the cross sections depicted in Figure 10 as determined by EDS measurement. (A) and (B) panels depict data for IN738 + CoNiCrAlY + IL aluminizing + heat treatment and IN738 CoNiCrAlY + Pack aluminizing + heat treatment, respectively.

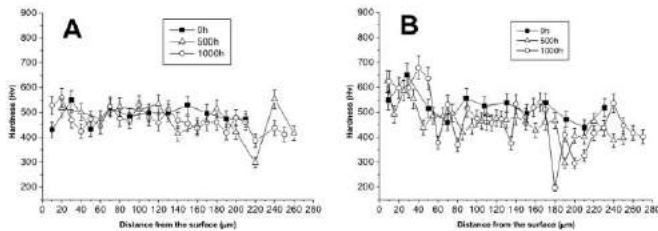


Figure 13. Hardness profile measurement for IN738 + CoNiCrAlY + Pack aluminizing + Post treatment (A) and IN738 + CoNiCrAlY + IL aluminizing + post treatment (B), respectively, after 500 and 1000 h of isothermal test (1000 °C).

XRD data (Figure 14) confirm the good resistance for both types of over-aluminized samples.

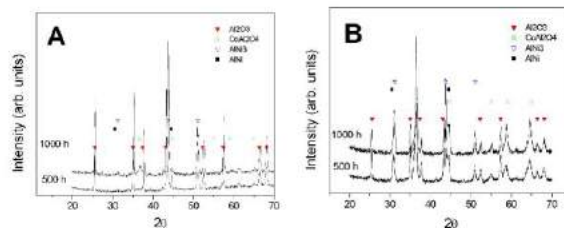


Figure 14. Surface XRD pattern of IN738 + CoNiCrAlY + Pack aluminizing + Post treatment (A) and IN738 + CoNiCrAlY + IL aluminizing + post treatment (B), respectively, after 500 and 1000 h of isothermal test (1000 °C).

4. Conclusions

The results obtained in the present study can be summarized as follows:

- Apparently, the two-step aluminizing process by Al-electrodeposition and consequent diffusion heat treatment (IL aluminizing) is not suitable for the direct application over IN738. Al inward diffusion seems to be inhibited by the possible formation of carbides or nitrides. These precipitates were observed after the diffusion post treatment, and they could result from the reaction of traces of ionic liquid entrapped in the growing Al layer with the base material. A further cleaning process could be attempted after the electroplating step in order to avoid the presence of IL residuals.
- Over-aluminizing of CoNiCrAlY is beneficial in order to create a viable anti-corrosion coating. This is due to the high Ni interdiffusion from the base material to the coating. This behavior causes the transformation of the β NiAl into γ Ni₃Al, which is less protective under oxidative and corrosive environment. For this reason, a further aluminizing step (over-aluminizing) is required for these types of metallic coatings in order to enhance the oxidation resistance at high temperatures.
- Being virtually free of W, Ta, Ti, there is no formation of carbides in the CoNiCrAlY coat; therefore, IL over-aluminizing on CoNiCrAlY allows a better and deeper diffusion of the Al toward the coating with respect to the pack over-aluminizing process.

Overall, the IL aluminizing process results in being feasible and suitable as an over-aluminizing step onto CoNiCrAlY metallic coatings for high temperature oxidation protection but not for direct aluminizing of IN738.

Acknowledgments: The research leading to these results has received funding from the European Union Seventh Framework Programme (FP7/2007-2013) under Grant No. 608698. We wish to thank the IoLiTec Ionic Liquids Technologies GmbH (Heilbronn, Germany) for supplying the Ionic Liquid used in this study.

Author Contributions: Luca Tagliaferri and Stefano Caporali conceived and designed the experiments, analyzed the data, and wrote the paper; Stefano M. Martinuzzi realized the Al-electrodeposition from ionic liquid and Francesco Bozza via pack cementation. Enrico Berretti performed and analyzed the hardness profiles, and Andrea Giaccherini analyzed the XRD data. Martin Thoma and Ugo Bardi analyzed the data and contributed to the paper writing.

Conflicts of Interest: The authors declare no conflict of interest.

References

1. Bozza, F.; Bolelli, G.; Giolli, C.; Giorgetti, A.; Lusvarghi, L.; Sassatelli, P.; Scrivani, A.; Candelì, A.; Thoma, M. Diffusion mechanisms and microstructure development in pack aluminizing of Ni-based alloys. *Surf. Coat. Tech.* **2014**, *239*, 147–159. [[CrossRef](#)]
2. Xiang, Z.D.; Burnell-Gray, J.S.; Datta, P.K. Aluminide coating formation on nickel-base superalloys by pack cementation process. *J. Mater. Sci.* **2001**, *36*, 5673–5682. [[CrossRef](#)]
3. Kim, D.; Sah, I.; Lee, H.J.; Hong, S.; Jang, C. Development of an aluminide coating layer on Alloy 617 by Al sputtering and inter-diffusion heat treatments. *Surf. Coat. Technol.* **2014**, *244*, 15–22. [[CrossRef](#)]
4. Wang, Y.; Chen, W.; Wang, L. Micro-indentation and erosion properties of thermal sprayed NiAl intermetallic-based alloy coatings. *Wear* **2003**, *254*, 350–355. [[CrossRef](#)]
5. Wang, Y.; Chen, W. Effect of ceria on the erosion resistance of HVOF thermal sprayed NiAl intermetallic coatings. *J. Mater. Sci. Lett.* **2003**, *22*, 845–851. [[CrossRef](#)]
6. Deevi, S.C.; Sikka, V.K.; Liu, C.T. Processing, properties, and applications of nickel and iron aluminides. *Prog. Mater. Sci.* **1997**, *42*, 177–192. [[CrossRef](#)]
7. Lih, W.; Chang, E.; Wu, B.C.; Chao, C.H. The effect of pack-aluminisation on the microstructure of MCrAlY and the performance of thermal barrier coatings. *Surf. Coat. Technol.* **1992**, *50*, 277–288. [[CrossRef](#)]
8. Chang, S.F.; Chao, C.H.; Wu, B.C.; Leu, R.Q.; Chang, E. Zirconia/pack-aluminized Co-29Cr-6Al-1Y thermal barrier coatings. *J. Vac. Sci. Technol. A* **1991**, *9*, 2099–2106. [[CrossRef](#)]
9. Tong, L.; Dengzun, Y.; Chungen, Z. Low-temperature formation of aluminide coatings on Ni-base superalloys by pack cementation process. *Chin. J. Aeronaut.* **2010**, *23*, 381–385. [[CrossRef](#)]

10. Svensson, H.; Angenete, J.; Stiller, K. Microstructure of oxide scales on aluminide diffusion coatings after short time oxidation at 1050 °C. *Surf. Coat. Technol.* **2004**, *177*–178, 152–157. [CrossRef]
11. Fossati, A.; Ferdinando, M.; Lavacchi, A.; Scrivani, A.; Giolli, C.; Bardi, U. Improvement of the oxidation resistance of CoNiCrAlY bond coats sprayed by high velocity oxygen-fuel onto nickel superalloy substrate. *Coatings* **2011**, *1*, 3–16. [CrossRef]
12. Choy, K.L. Chemical vapour deposition of coatings. *Prog. Mater. Sci.* **2003**, *48*, 57–170. [CrossRef]
13. Thoma, M.; Scrivani, A.; Giolli, C.; Giorgetti, A. Aluminizing turbine parts—Processes and coatings. In Proceedings of the ASME Turbo Expo 2011, Vancouver, BC, Canada, 6–10 June 2011.
14. Mishin, Y. Atomistic modeling of the γ and γ' -phases of the Ni–Al system. *Acta Mater.* **2004**, *52*, 1451–1467. [CrossRef]
15. Wu, K.; Chang, Y.A.; Wang, Y. Simulating interdiffusion microstructures in Ni–Al–Cr diffusion couples: A phase field approach coupled with CALPHAD database. *Scripta Mater.* **2004**, *50*, 1145–1150. [CrossRef]
16. Bardi, U.; Caporali, S.; Craig, M.; Lavacchi, A.; Nicholls, J. A Method for Making a Protective Coating on a Metal Substrate. European Patent No 2330233 A1, 1 December 2009.
17. Abbott, A.P.; Harris, R.C.; Hsieh, Y.T.; Ryder, K.S.; Wen-Sun, I. Aluminium electrodeposition under ambient conditions. *Phys. Chem. Chem. Phys.* **2014**, *16*, 14675–14681. [CrossRef] [PubMed]
18. Fang, Y.; Yoshii, K.; Jiang, X.; Sun, X.G.; Tsuda, T.; Mehio, N.; Dai, S. An AlCl_3 based ionic liquid with a neutral substituted pyridine ligand for electrochemical deposition of aluminum. *Electrochim. Acta* **2015**, *160*, 82–88. [CrossRef]
19. Wang, Q.; Chen, B.; Zhang, Q.; Lu, X.; Zhang, S. Aluminium deposition from lewis acidic 1-butyl-3-methylimidazolium chloroaluminate ionic liquid ([Bmim]Cl/ AlCl_3) modified with methyl nicotinate. *ChemElectroChem* **2015**, *2*, 1794–1798. [CrossRef]
20. Wang, Q.; Zhang, Q.; Chen, B.; Lu, X.; Zhang, S. Electrodeposition of bright Al coatings from 1-butyl-3-methylimidazolium chloroaluminate ionic liquids with specific additives. *J. Electrochem. Soc.* **2015**, *162*, D320–D324. [CrossRef]
21. Zheng, Y.; Zhang, S.; Lu, X.; Wang, Q.; Zuo, Y.; Liu, L. Low-temperature electrodeposition of aluminium from lewis acidic 1-allyl-3-methylimidazolium chloroaluminate ionic liquids. *Chin. J. Chem. Eng.* **2012**, *20*, 130–139. [CrossRef]
22. Berretti, E.; Giaccherini, A.; Martinuzzi, S.M.; Innocenti, M.; Schubert, T.J.S.; Stiemke, F.M.; Caporali, S. Aluminium Electrodeposition from Ionic Liquid: Effect of Deposition Temperature and Sonication. *Materials* **2016**, *9*, 719. [CrossRef]
23. Project Scail-Up. Scaling-Up of the Aluminium Plating Process from Ionic Liquid. Available online: <http://scailup.eu> (accessed on 25 February 2017).
24. Caporali, S.; Martinuzzi, S.M.; von Czarnecki, P.; Schubert, T.J.S.; Bardi, U. Effects of metal ions on the aluminum electrodeposition from ionic liquids. *J. Mater. Eng. Perform.* **2017**, *26*, 685–691. [CrossRef]



© 2017 by the authors. Licensee MDPI, Basel, Switzerland. This article is an open access article distributed under the terms and conditions of the Creative Commons Attribution (CC BY) license (<http://creativecommons.org/licenses/by/4.0/>).

7 Bibliography

1. Hunt, L. B. The early history of gold plating. *Gold Bull.* **6**, 16–27 (1973).
2. Foresti, M. L. *Elettrochimica dei materiali e dei nanosistemi*. (2012).
3. Hogendoorn, B. *Heinemann Chemistry Enhanced 2*. (Pearson Education Australia, 2010).
4. Paunovic, M. & Schlesinger, M. *Fundamentals of Electrochemical Deposition*. (John Wiley & Sons, Inc., 2006). doi:10.1002/0470009403
5. Bertorelle, E. *Trattato di Galvanotecnica*. (Hoepli).
6. Innocenti, M., Pezzatini, G., Forni, F. & Foresti, M. L. CdS and ZnS Deposition on Ag(111) by Electrochemical Atomic Layer Epitaxy. *J. Electrochem. Soc.* **148**, C357 (2001).
7. Foresti, M. *et al.* Electrochemical atomic layer epitaxy deposition of CdS on Ag (111): An electrochemical and STM investigation. *J. Phys. Chem. B* **102**, 7413–7420 (1998).
8. Berretti, E. *et al.* Electrodeposition and Characterization of p and n Sulfide Semiconductors Composite Thin Film. *J. Electrochem. Soc.* **163**, D3034–D3039 (2016).
9. Oviedo, O. A., Reinaudi, L., Garcia, S. & Leiva, E. P. M. *Underpotential Deposition*. (Springer International Publishing, 2016). doi:10.1007/978-3-319-24394-8
10. Innocenti, M., Cattarin, S., Cavallini, M., Loglio, F. & Foresti, M. L. Characterisation of thin films of CdS deposited on Ag(111) by ECALE. A morphological and photoelectrochemical investigation. *J. Electroanal. Chem.* **532**, 219–225 (2002).
11. Stickney, J. L. Electrochemical ALD. *ECS Interface* 28–30 (2011).
12. Cleere, Henry; Tylecote, R. F. A History of Metallurgy. *Archaeol. J.* **134**, 446–446 (1977).
13. Lechtman, H. Pre-Columbian surface metallurgy. *Sci. Am.* **250**, 56–63 (1984).
14. Cesareo, R. *et al.* Multilayered artifacts in the pre-Columbian metallurgy from the North of Peru. *Appl. Phys. A* **113**, 889–903 (2013).
15. Al Amri, Z., Mercer, M. P. & Vasiljevic, N. Surface Limited Redox Replacement Deposition of Platinum Ultrathin Films on Gold: Thickness and Structure Dependent Activity towards the Carbon Monoxide and Formic Acid Oxidation reactions. *Electrochim. Acta* **210**, 520–529 (2016).

16. Viyannalage, L. T., Vasilic, R. & Dimitrov, N. Epitaxial Growth of Cu on Au(111) and Ag(111) by Surface Limited Redox Replacement An Electrochemical and STM Study. *J. Phys. Chem. C* **111**, 4036–4041 (2007).
17. Ambrozik, S., Rawlings, B., Vasiljevic, N. & Dimitrov, N. Metal deposition via electroless surface limited redox replacement. *Electrochem. commun.* **44**, 19–22 (2014).
18. Minguzzi, A. *et al.* Fixed Energy X-ray Absorption Voltammetry. *Anal. Chem.* **85**, 7009–7013 (2013).
19. Rondinini, S. *et al.* Fixed Energy X-ray Absorption Voltammetry and Extended X-ray Absorption fine Structure of Ag nanoparticle electrodes. *J. Electroanal. Chem.* **766**, 71–77 (2016).
20. Keil, P., Lützenkirchen-Hecht, D. & Frahm, R. Grazing incidence XAFS under non-specular conditions. *Phys. B Condens. Matter* **357**, 1–5 (2005).
21. EG&G Technical Services, I. Fuel Cell Handbook. *Fuel Cell* **7 Edition**, 1–352 (2004).
22. Abuadmah, H. Fuel Cells Versus Heat Engines: A Perspective of Thermodynamic and Production Efficiencies. (2012).
23. Lavacchi, A., Miller, H. & Vizza, F. *Nanotechnology in Electrocatalysis for Energy*. **170**, (Springer New York, 2013).
24. Akhairi, M. A. F. & Kamarudin, S. K. Catalysts in direct ethanol fuel cell (DEFC): An overview. *Int. J. Hydrogen Energy* **41**, 4214–4228 (2016).
25. Fang, X., Wang, L., Shen, P. K., Cui, G. & Bianchini, C. An in situ Fourier transform infrared spectroelectrochemical study on ethanol electrooxidation on Pd in alkaline solution. *J. Power Sources* **195**, 1375–1378 (2010).
26. Wang, L. *et al.* Deactivation of Palladium Electrocatalysts for Alcohols Oxidation in Basic Electrolytes. *Electrochim. Acta* **177**, 100–106 (2015).
27. Friedl, J. & Stimming, U. Model catalyst studies on hydrogen and ethanol oxidation for fuel cells. *Electrochim. Acta* **101**, 41–58 (2013).
28. Hachkar, M., Napporn, T., Léger, J.-M., Beden, B. & Lamy, C. An electrochemical quartz crystal microbalance investigation of the adsorption and oxidation of CO on a platinum electrode. *Electrochim. Acta* **41**, 2721–2730 (1996).
29. Lucas, C. A., Markovic, N. M., Grgur, B. N. & Ross, P. N. Structural effects during CO adsorption on Pt–bimetallic surfaces. *Surf. Sci.* **448**, 65–76 (2000).
30. Lucas, C. A., Marković, N. M. & Ross, P. N. Structural effects during CO

- adsorption on Pt-bimetallic surfaces. II. The Pt(111) electrode. *Surf. Sci.* **448**, 77–86 (2000).
31. Lamy, C. *et al.* Recent advances in the development of direct alcohol fuel cells (DAFC). *J. Power Sources* **105**, 283–296 (2002).
 32. Kutz, R. B. *et al.* Reaction pathways of ethanol electrooxidation on polycrystalline platinum catalysts in acidic electrolytes. *J. Catal.* **278**, 181–188 (2011).
 33. Miller, H. A. *et al.* A Pd/C-CeO₂ Anode Catalyst for High-Performance Platinum-Free Anion Exchange Membrane Fuel Cells. *Angew. Chem. Int. Ed. Engl.* **55**, 6004–7 (2016).
 34. Bambagioni, V. *et al.* Energy Efficiency Enhancement of Ethanol Electrooxidation on Pd-CeO₂/C in Passive and Active Polymer Electrolyte-Membrane Fuel Cells. *ChemSusChem* **5**, 1266–1273 (2012).
 35. Antolini, E. & Gonzalez, E. R. Alkaline direct alcohol fuel cells. *J. Power Sources* **195**, 3431–3450 (2010).
 36. Guo, J., Chen, R., Zhu, F.-C., Sun, S.-G. & Villullas, H. M. New Understandings of Ethanol Oxidation Reaction Mechanism on Pd/C and Pd 2 Ru/C Catalysts in Alkaline Direct Ethanol Fuel Cells. *Appl. Catal. B Environ.* (2017). doi:10.1016/j.apcatb.2017.10.037
 37. Wang, J. *et al.* Comparative study to understand the intrinsic properties of Pt and Pd catalysts for methanol and ethanol oxidation in alkaline media. *Electrochim. Acta* **185**, 267–275 (2015).
 38. Antolini, E. & Perez, J. Anode Catalysts for Alkaline Direct Alcohol Fuel Cells and Characteristics of the Catalyst Layer. in 89–127 (2013). doi:10.1007/978-1-4471-4911-8_5
 39. Liang, Z. X., Zhao, T. S., Xu, J. B. & Zhu, L. D. Mechanism study of the ethanol oxidation reaction on palladium in alkaline media. *Electrochim. Acta* **54**, 2203–2208 (2009).
 40. Xu, C., Shen, P. kang & Liu, Y. Ethanol electrooxidation on Pt/C and Pd/C catalysts promoted with oxide. *J. Power Sources* **164**, 527–531 (2007).
 41. Shen, P. K. & Xu, C. Alcohol oxidation on nanocrystalline oxide Pd/C promoted electrocatalysts. *Electrochem. commun.* **8**, 184–188 (2006).
 42. Bambagioni, V. *et al.* Single-site and nanosized Fe–Co electrocatalysts for oxygen reduction: Synthesis, characterization and catalytic performance. *J. Power Sources* **196**, 2519–2529 (2011).
 43. Walter Giurlani. In situ X-ray Absorption Spectroscopy for electrocatalytic processes. (University of Florence, 2015).

44. Stickney, J. L. Electrochemical Atomic Layer Epitaxy (EC-ALE): Nanoscale Control in the Electrodeposition of Compound Semiconductors. in *Advances in Electrochemical Science and Engineering, Volume 7* 1–105 (Wiley-VCH Verlag GmbH). doi:10.1002/3527600264.ch1
45. Brett, A. M. O., Matysik, F.-M. & Vieira, M. T. Thin-film gold electrodes produced by magnetron sputtering. Voltammetric characteristics and application in batch injection analysis with amperometric detection. *Electroanalysis* **9**, 209–212 (1997).
46. Delgado, J. M., Orts, J. M., Pérez, J. M. & Rodes, A. Sputtered thin-film gold electrodes for in situ ATR-SEIRAS and SERS studies. *J. Electroanal. Chem.* **617**, 130–140 (2008).
47. Mie, Y., Ikegami, M. & Komatsu, Y. Gold sputtered electrode surfaces enhance direct electron transfer reactions of human cytochrome P450s. *Electrochem. commun.* **12**, 680–683 (2010).
48. Snyder, J. *et al.* Thin film approach to single crystalline electrochemistry. *J. Phys. Chem. C* **117**, 23790–23796 (2013).
49. Maljusch, A., Henry, J. B., Schuhmann, W. & Bondarenko, A. S. A quick method for the preparation of Pt(111)-like thin films. *Electrochem. commun.* **16**, 88–91 (2012).
50. Dimitrov, N. Recent Advances in the Growth of Metals, Alloys, and Multilayers by Surface Limited Redox Replacement (SLRR) Based Approaches. *Electrochim. Acta* **209**, 599–622 (2016).
51. Chen, H. *et al.* Palladium modified gold nanoparticles as electrocatalysts for ethanol electrooxidation. *J. Power Sources* **321**, 264–269 (2016).
52. Sheridan, L. B., Yates, V. M., Benson, D. M., Stickney, J. L. & Robinson, D. B. Hydrogen sorption properties of bare and Rh-modified Pd nanofilms grown via surface limited redox replacement reactions. *Electrochim. Acta* **128**, 400–405 (2014).
53. Soldo-Olivier, Y., De Santis, M., Liang, W. & Sibert, E. Growth mechanisms of Pd nanofilms electrodeposited onto Au(111): an in situ grazing incidence X-ray diffraction study. *Phys. Chem. Chem. Phys.* **18**, 2830–2839 (2016).
54. Herrero, E., Buller, L. J. & Abruña, H. D. Underpotential deposition at single crystal surfaces of Au, Pt, Ag and other materials. *Chem. Rev.* **101**, 1897–1930 (2001).
55. Nakamura, M., Endo, O., Ohta, T., Ito, M. & Yoda, Y. Surface X-ray diffraction study of Cu UPD on Au(1) electrode in 0.5 M H₂SO₄ solution: the coadsorption structure of UPD copper, hydration water molecule and bisulfate anion on Au(1). *Surf. Sci.* **514**, 227–233 (2002).

56. Avci, E. AN ELECTROCHEMICAL STUDY OF THE DEPOSITION OF COPPER AND SILVER ON THYMINE MODIFIED AU(111). **0**, (Freie Universität Berlin, 2007).
57. Bulk copper deposition on gold studied in an EC-AFM application using the FlexAFM. *nanoSurf* 1–4
58. Dell'Aquila, V. Oxidation of alcohols with surfaces modified by electrodeposition. (University of Florence, 2016).
59. Kiani, A. & Fard, E. N. Fabrication of palladium coated nanoporous gold film electrode via underpotential deposition and spontaneous metal replacement: A low palladium loading electrode with electrocatalytic activity. *Electrochim. Acta* **54**, 7254–7259 (2009).
60. Shirley, D. A. High-Resolution X-Ray Photoemission Spectrum of the Valence Bands of Gold. *Phys. Rev. B* **5**, 4709–4714 (1972).
61. Smith, G. C. & Seah, M. P. Standard reference spectra for XPS and AES: Their derivation, validation and use. *Surf. Interface Anal.* **16**, 144–148 (1990).
62. Cheng, F. *et al.* Synergistic effect of Pd–Au bimetallic surfaces in Au-covered Pd nanowires studied for ethanol oxidation. *Electrochim. Acta* **55**, 2295–2298 (2010).
63. Wilkes, J. S. A short history of ionic liquids—from molten salts to neoteric solvents. *Green Chem.* **4**, 73–80 (2002).
64. *Physicochemical Properties of Ionic Liquid Mixtures*. (Springer Netherlands, 2016). doi:10.1007/978-94-017-7573-1
65. ACS. Production of aluminum metal by electrochemistry. 8 (1997).
66. Seacharran, K. *Bayer Process Chemistry*. (1893).
67. The Sigal process for electrodeposition of aluminium. *Anti-Corrosion Methods Mater.* **32**, 13–13 (1985).
68. *Electrodeposition from Ionic Liquids*. (Wiley-VCH Verlag GmbH & Co. KGaA, 2008). doi:10.1002/9783527622917
69. Yadav, J. S., Reddy, B. V. S., Reddy, M. S., Niranjan, N. & Prasad, A. R. Lewis Acidic Chloroaluminate Ionic Liquids: Novel Reaction Media for the Synthesis of 4-Chloropyrans. *European J. Org. Chem.* **2003**, 1779–1783 (2003).
70. Landolt, C. M. and D. The Rotating Cylinder Hull Cell: Design and Application. *Plat. Surf. Finish.* **80**, 73–78 (1993).
71. Madore, C., Landolt, D., Hassenpflug, C. & Hermann, J. A. Application of

- the Rotating Cylinder Hull Cell to the Measurement of Throwing Power and the Monitoring of Copper Plating Baths. *Plat. Surf. Finish.* **82**, 36–41 (1995).
72. Yang, K. & Liu, C.-G. HETEROGENEOUS CATALYST IN IONIC LIQUIDS: ZIRCONIA SUPPORTED GOLD NANOPARTICLES. in *Material Engineering and Mechanical Engineering* 1336–1342 (WORLD SCIENTIFIC, 2016). doi:10.1142/9789814759687_0149
73. Fletcher, C. A. J. *Computational Techniques for Fluid Dynamics 1*. (Springer Berlin Heidelberg, 1988). doi:10.1007/978-3-642-97035-1
74. *Comprehensive Treatise of Electrochemistry*. (Springer US, 1984). doi:10.1007/978-1-4613-2679-3
75. Giaccherini, A. *et al.* Finite Elements Analysis of an Electrochemical Coating Process of an Irregularly Shaped Cathode with COMSOL Multiphysics(R). *ECS Trans.* **64**, 1–8 (2015).
76. Kosieniak, E., Biesiada, K., Kaczorowski, J. & Innocenti, M. Corrosion failures in gas turbine hot components. *J. Fail. Anal. Prev.* **12**, 330–337 (2012).
77. Nicholls, J. R., Simms, N. J. & Encinas-Oropesa, A. Modelling hot corrosion in industrial gas turbines. *Mater. High Temp.* **24**, 149–162 (2007).
78. Eliaz, N., Shemesh, G. & Latanision, R. M. Hot corrosion in gas turbine components. *Eng. Fail. Anal.* **9**, 31–43 (2002).
79. Zucchi, K. Electrochemical identical location techniques in electron microscopy. (University of Florence, 2017).
80. Schlögl, K., Mayrhofer, K. J. J., Hanzlik, M. & Arenz, M. Identical-location TEM investigations of Pt/C electrocatalyst degradation at elevated temperatures. *J. Electroanal. Chem.* **662**, 355–360 (2011).